University of South Carolina
Scholar Commons

Theses and Dissertations

1-1-2013

Toward Sophisticated Controls of Two-Phase Transport at Micro/ Nano-Scale

Fanghao Yang
University of South Carolina

Follow this and additional works at: https://scholarcommons.sc.edu/etd

 Part of the Mechanical Engineering Commons

Recommended Citation

Yang, F.(2013). *Toward Sophisticated Controls of Two-Phase Transport at Micro/Nano-Scale.* (Doctoral dissertation). Retrieved from https://scholarcommons.sc.edu/etd/2336

This Open Access Dissertation is brought to you by Scholar Commons. It has been accepted for inclusion in Theses and Dissertations by an authorized administrator of Scholar Commons. For more information, please contact digres@mailbox.sc.edu.

TOWARD SOPHISTICATED CONTROLS OF TWO-PHASE TRANSPORT AT MICRO/NANO-SCALE

by

Fanghao Yang

Bachelor of Engineering
Beijing University of Aeronautics & Astronautics, 2008

Submitted in Partial Fulfillment of the Requirements

For the Degree of Doctor of Philosophy in

Mechanical Engineering

College of Engineering and Computing

University of South Carolina

2013

Accepted by:

Dr. Chen Li, Major Professor

Dr. Jamil Khan, Committee Member

Dr. Guiren Wang, Committee Member

Dr. Roger Dougal, Committee Member

Lacy Ford, Vice Provost and Dean of Graduate Studies

© Copyright by Fanghao Yang, 2013
All Rights Reserved.

DEDICATION

I would like to thank my parents, who encourage me all these years. Also, it is dedicated to my wife, Lijin, for her love and supporting.

ACKNOWLEDGEMENTS

As a bachelor of engineering majored in Instrumentation engineering, I had no fundamental knowledge on heat transfer and fluid mechanics but only solid mechanics when I was joining Dr. Chen Li's research group, which focus on two-phase transport in micro/nano-scale. In the past four years in University of South Carolina, I was very fortunate to work with Dr. Chen Li, my research advisor. Completing my study toward my doctor of philosophy has been a truly challenging and rewarding experience. Dr. Chen Li offers me countless support and encourage for my academic study and living. It is almost impossible to image that I could finish all these work without his generous help and insightful guidance. First of all, I would say thanks to him, sincerely.

Secondly, I would like to thank my committee members, Dr. Jamil Khan, Dr. Guiren Wang and Dr. Roger Dougal. I appreciate the opportunities to work with Dr. Jamil Khan and his students for flow boiling on copper nanowired interfaces and publish my first journal papers as a co-author. This is a great fundamental experience for my further study on two-phase transport in microchannels. I also learnt a lot from Dr. Guiren Wang and his student, Fang Yang, who are researchers on microfluidic systems. For Dr. Roger Dougal, although he is a professor of electrical engineering and doesn’t focus on phase-change heat transfer, I was amazed by his in-depth understanding on applied physics and extensive view of engineering.

Moreover, I would like to thank my co-workers and friends, Xianming Dai, Zach Wachter and Mehdi Famouri. It was very pleasant to work with these excellent and hard-working people in past four years. Recently, Mohammad Alwazzan and Dr. Xiaochuan Li joined our group and helped me a lot on running experiments. I would like to extend my thanks to them.

I would like to thank Dr. Yoav Peles in Rensselaer Polytechnic Institute and Dr. C.J. Kuo now in Intel Corp. for their help in microfabrication and building testing system. I also would like to thank my father, Er-wei Yang. He is a mechanical engineer with 30 years experience and his suggestions help me successfully design testing package.

Finally, I want to say thanks to all my friends, my parents and my wife. They shared encouragement and optimism with me when I was struggling through my research. Their love supports me to conquer every difficulty in my study and life.

This work was supported by the startup funding of the University of South Carolina (USC) and the U.S. Department of Defense, Office of Naval Research under the Grant N000140810080 (Program Officer Mrs. Sharon Beermann-Curtin) and the Grant N000141210724 (Program Officer Dr. Mark Spector). SEM figures in this study were taken in the Electron Microscopy Center at University of South Carolina. Part of the microfabrication was performed at the Cornell Nanoscale Facility (CNF), a member of the National Nanotechnology Infrastructure Network of United States, which is supported by the National Science Foundation under the Grant ECS-0335765.

ABSTRACT

Through the use of latent heat evaporating, flow boiling in microchannels offers new opportunities to enable high efficient heat and mass transport for a wide range of emerging applications such as high power electric/electronic/optical cooling, compact heat exchangers and reactors. However, flow boiling in microchannels is hampered by several severe constraints such as bubble confinement (e.g., slug flow), viscosity and surface tension force-dominated flows, which result in unpredictable flow pattern transitions and tend to induce severe flow boiling instabilities (i.e. low-frequency and large magnitude flows) and suppress evaporation and convection.

In this dissertation, three novel micro/nanoscale thermo-fluidic control methodologies were developed to address these aforementioned constraints faced in flow boiling in microchannels. These include a) "unifying two-phase flow patterns" to radically avoid pattern transitions, b) "nano-tips induced boundary layers" to promote evaporation and advections by reconstructing boundary layers, and c) "high frequency self-sustained two-phase oscillations" to generate strong mixing in the laminar flow. Using superhydrophilic silicon nanowires, the first methodology successfully formulated a new, single and periodic annular flow during the entire flow boiling process, i.e., from the onset of nucleate boiling to the critical heat flux (CHF) conditions by reducing the characteristic bubble size and transforming the direction of the dominant capillary forces from the cross-sectional plane to inner-wall plane. In the second methodology, boundary layers were induced along vertical walls by hydrophilic nanotips using surface tension

forces, which is the first time to achieve the design of boundary layers that ultimately govern heat and mass transfer. In the last approach, novel microfluidic transistors were devised to passively introduce and sustain high frequency bubble growth/collapse processes and hence to create strong mixing in microchannels. Compared with the state-of-the- art techniques, by directly targeting on manipulating bubble dynamics and governing forces, consequently, the fluid structures, these three novel principles can enable substantially higher flow boiling performance in terms of heat transfer coefficient, CHF, and flow boiling stabilities. Equally important, pressure drop was also well managed or even greatly reduced. Theoretical study was also conducted to understand the mechanisms and provide insight to new flow boiling phenomena.

PREFACE

Since 1980, micro/nanofabrication technologies were developed to realize miniature system. In the same time, two-phase transport at micro/nano-scale were well promoted and developed to efficiently transfer heat and mass by utilizing phase change phenomena in microsystems. It was widely applied in various engineering fields, including micro heat-exchangers (Jiang, Wong et al. 2001;Mudawar 2001;Kandlikar 2002;Wang and Cheng 2009), micro chemical reactors (Andersson, van der Wijngaart et al. 2001;Kobayashi, Mori et al. 2004), micro propulsion for aerospace engineering (Hitt, Zakrzwski et al. 2001), bio-MEMS(Tadashi Okamoto 2000;Shui, Pennathur et al. 2008), micro-pump/valve (Ory, Yuan et al. 2000;Andersson, van der Wijngaart et al. 2001;Tsai and Lin 2002;R. B. Maxwell 2003;Cheng and Liu 2006) and micro-mixers (Losey, Jackman et al. 2002;Robin H. Liu 2002;Tsai and Lin 2002).

An ideal two-phase transport system, no matter conventional scale or micro/nano-scale, could be evaluated at three aspects. First, it should have highest efficiency to transfer heat and mass while requiring lowest driving power. Secondly, an ideal system should also have controllable instabilities and reliability. It should work stably at various working conditions without significantly losing performance. Finally, it shall be light-weight, small, compact and low-cost to manufacture.

Due to the enlarged surface area to volume ratio, heat and mass are converted and transferred in microsystem more efficiently than conventional system. Microscale two-phase systems commonly take more advantages on cost, weight and space-saving than conventional systems. However, rapid vaporization of a liquid usually leads to a large volume of gas confined inside such small domains so that instabilities exist when bulk boiling happens. Generally, comparing to conventional system, the major challenges for microscale two-phase system is how to effectively manipulate two-phase flow in geometrically confined small domains and suppress instabilities without sacrificing performance. To conquer these challenges, solutions may be considered at different scales from nanoscale to system scale. In this dissertation, three methods are introduced toward sophisticated control of two-phase transport in micro/nano-scale.

TABLE OF CONTENTS

LIST OF TABLES

LIST OF FIGURES

LIST OF SYMBOLS

A	Area, m^2
C_p	Heat capacity at constant pressure, J/kg ŀK
D	Diameter, m
F	Force, N
G	Mass flux, kg/m^2 s
$\bar{h}$	Average heat transfer coefficient, W/m^2 ŀK
h_{fg}	Latent heat of vaporization, kJ/kg
H	Channel height, m
I	Electrical current, A
k	Thermal conductivity, W/m ŀK
K	Slope of linear function, Ω/K
L	Length, m
m	Parameter for pin efficiency
$\dot{m}$	Mass flow rate, kg/s
N	Number of microchannels
Δp	Pressure drop, N/m^2
p	Pressure, N/m^2
P	Power, W
$\dot{Q}$	Heat loss, W

q''	Heat flux, W/cm^2
R	Electrical resistance, Ω
t	Thickness, m
T	Temperature, ℃
$\bar{T}$	Average temperature, ℃
ΔT	Superheat, K
ΔT_{sub}	Subcooling temperature, K
u	Velocity, m/s
$\bar{u}$	Average flow velocity, m/s
V	Electrical voltage, V
W	Microchannel width, m
α	Void fraction
γ	Surface tension, N/m
θ	Contact angle
μ	Viscosity, kg/(s·m)
η	Fin efficiency
ρ	Density, kg/m^3
χ	Vapor quality
σ_i	Interfacial stress, N/m^2
ρ	Density, kg/m^3
δ_τ	Boundary layer thickness, m

LIST OF ABBREVIATIONS

2ϕ ..... Two-phase

acc ..... Accelerational

c ..... Cross-sectional

CHF ..... Critical heat flux

e ..... Exit

eff ..... Effective

exp ..... Experimental

f ..... Frictional

h ..... Hydraulic

HTC ..... Heat Transfer Coefficient

i ..... Inlet

l ..... Liquid

m ..... Mixture

NW ..... Nanowire

NP ..... Nanoparticles

o ..... Outlet

sat ..... Saturated

Si ..... Silicon

v ..... Vapor

CHAPTER 1

INTRODUCTION OF MICROSCALE TWO PHASE TRANSPORT

Microscale two-phase transport denotes heat and mass transfer in microscale two phase flows, which are liquid and gas flow. Gas flow could be entrained in the inlet flow or generated during phase-change inside microchannels. Generally, microscale flow boiling and evaporation is one of the most efficient mass and energy transport phenomena, where energy is absorbed as latent heat during vaporization. Due to the existing of capillary forces in microchannels, the microscale two-phase flow characteristics is significantly different from the characteristics in conventional channels. With increasing of vapor qualities, various flow patterns are characterized in microchannels. As shown in Figure 1.1, bubbly flow, vapor slug flow, annular flow and churn flow are primary flow patterns of two-phase flow in microchannels (Mudawar 2001;Kandlikar 2002;Serizawa, Feng et al. 2002;Hetsroni, Mosyak et al. 2003). The bubbly flow is a two-phase flow where small bubbles are dispersed or suspended in a liquid flow. The liquid subcooling could affect on the bubble growth and bubble sizes (Wang and Cheng 2009). On the contrary, once bubble nucleation initiates in saturated flow, these small bubbles, whose diameters are smaller than hydraulic diameter, would gradually grow until reach the solid boundaries. Consequently, these bubbles would be confined and elongated in microchannels.

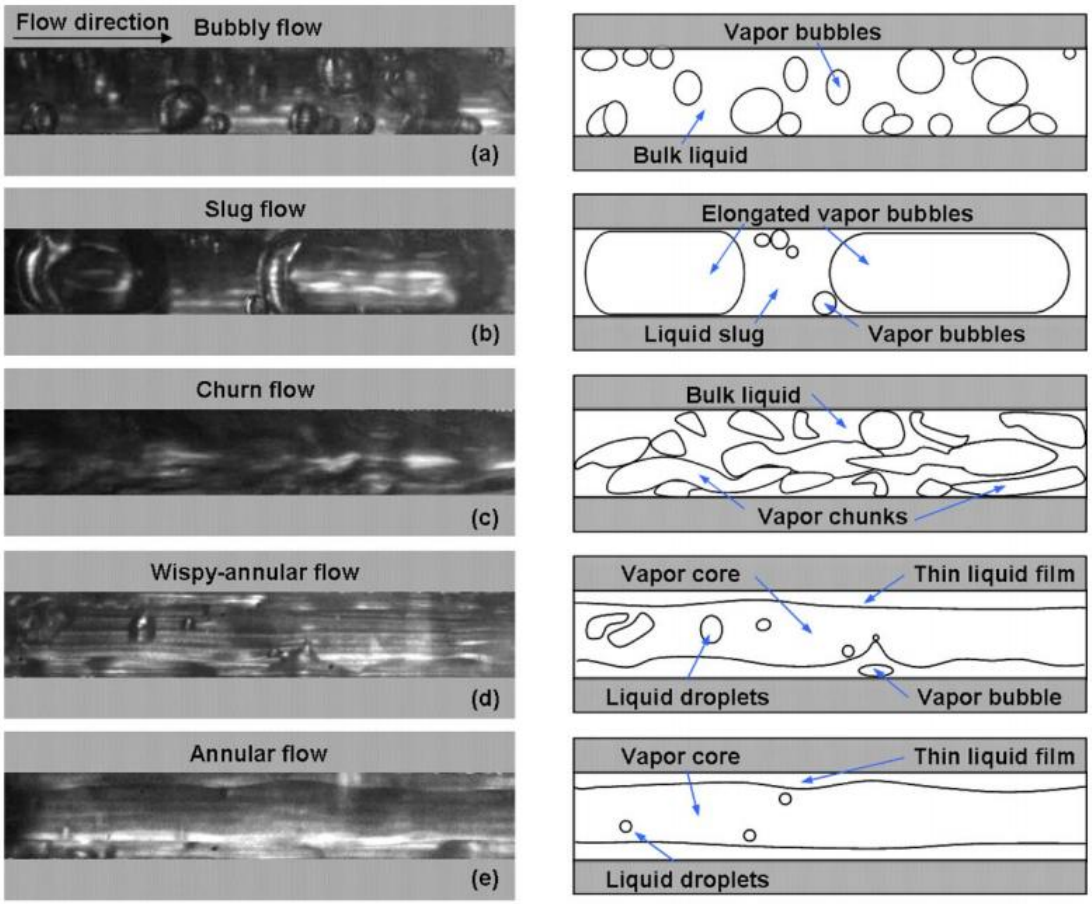

Figure 1.1. From a to e, different two-phase flow patterns are listed. (Harirchian and Garimella 2011)

These elongated vapor bubble grow rapidly after bubble ebullition so that vapor slug flows were generated inside microchannels as shown in Figure 1.1. The slug flow would increase the pressure drop (Serizawa, Feng et al. 2002) as a result of high capillary pressure between two ends of vapor slugs. The extra pressure drop would reduce the sliding between gas bubble and solid channel wall and therefore induce a local dry-out between the vapor slug and the wall. Furthermore, fast growth vapor slug may induce reverse flow into the inlet; therefore, the rewetting process is hindered. At high vapor qualities, either vapor slugs would grow and combine with others into a vapor core,

which forms annular flow, or, the interfacial shear stress could collapse these vapor slugs and form churn flow as a result of high-velocity vapor flow.

It seems that the existing of transitional flow patterns are intrinsic characteristics of two-phase flow in microchannels. And these transitions between different flow patterns are unpredictable. Critical flow transition modes, including the liquid/two-phase alternating flow (LTAF) and the liquid/two-phase/vapor alternating flow (LTVAF), were revealed in previous studies (Wu and Cheng 2003;Wu and Cheng 2004;Wu, Cheng et al. 2006). These phenomena lead to difficulties in controlling and stabilizing heat and mass transfer in microchannel. As a result, severe instability of heat and mass flux were observed in previous works (Wu and Cheng 2003;Wu and Cheng 2004;Bergles and Kandlikar 2005;Kuo and Peles 2008). And three primary modes of instabilities were demonstrated in microchannels: a) rapid bubble growth instability, b) upstream compressible volume/pressure drop instabilities and c) excursive instabilities.

The rapid bubble growth instability refers to an elongated bubble that grows rapidly in the longitudinal direction of a microchannel. This instability is caused by superheated temperature required to initiate bubble growth in microfabricated microchannels, which is typically made by deep reactive ion etching (DRIE) process. This process would generate deep trenches with a characteristic wall peak-to-peak roughness of 10 nm to 300 nm. This kind of smooth surface is lacking of active nucleation sites and not favored by nucleation boiling thus the liquid adjacent to the wall will attain high superheated temperatures before nucleation initiates. Once boiling start on an active nucleation sites, the superheated liquid will suddenly change to vapor and

cause an explosive boiling. Consequently, the vapor slug would grow to both ends of a microchannel due to rapidly increasing inner pressure. It leads to reverse flow.

The instability of upstream compressible volume is a result of reserve flow. The vapor bubble reversely flows into the subcooled inlet flow then condensation may occur. And high inlet pressure may also compress the compressible vapor volume. It shall lead to the oscillation of pressure drops and mass fluxes in inlet manifold of microchannels. Therefore, constant liquid supply could not be sustained in microchannels. Previous study (Qu and Mudawar 2004) suggests that premature CHF could be approached by flow instabilities induced vapor backflow into the heat sink's upstream plenum.

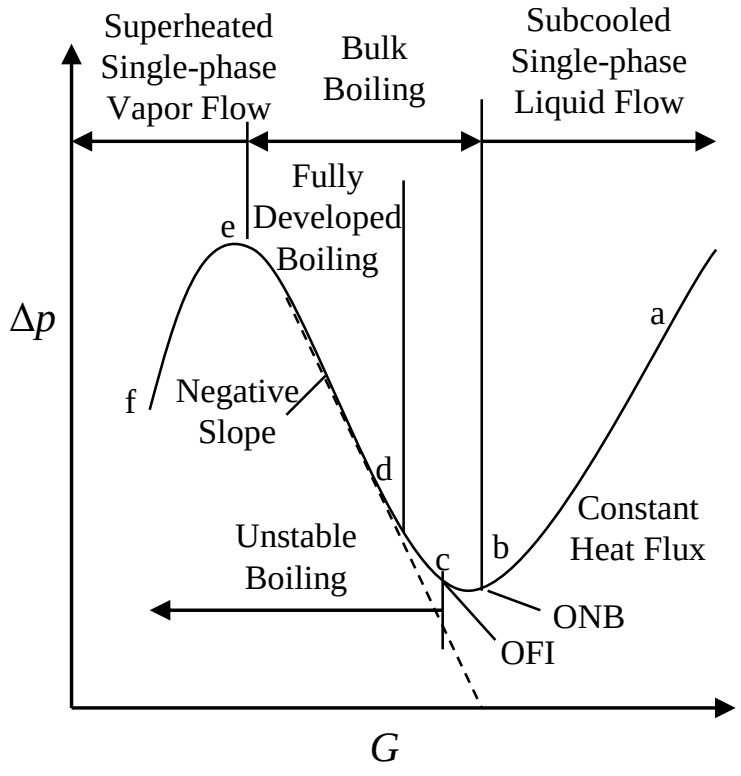

Figure 1.2. Classic Δ*p*-*G* curve of flow boiling in plain wall microchannels (Kosar, Kuo et al. 2005).

The Δ*p*-*G* curves in Figure 1.2 are plotted to analyze the excursive or Ledinegg instability in microchannels (Kosar, Kuo et al. 2005). At high mass fluxes and for fixed

heat flux, the pressure drop initially decreases with decreasing mass flux (segment *a* to *b* in Figure 1.2) before reaching a minimum termed onset of flow instability (*OFI*). In microchannels, it has been argued that *OFI* corresponds to a mass flux only slightly less than *ONB*. As the mass flux continue to decrease past *OFI*, the pressure drop-mass flux slope changes course and becomes negative (Segment *c* to *e* in Figure 1.2a). As discussed in Boure et al. (Boure, Bergles et al. 1973), when this happens, i.e., when

$$\frac{\partial(\Delta p)}{\partial G} \leq 0 \tag{1}$$

The system is susceptible to the excursive instability. During the transitions between different flow patterns, an M-shaped heat transfer coefficient curve reveals rapid drop of heat transfer coefficient during vapor slug flow before transition to annular flow(Bar-Cohen and Rahim 2009).

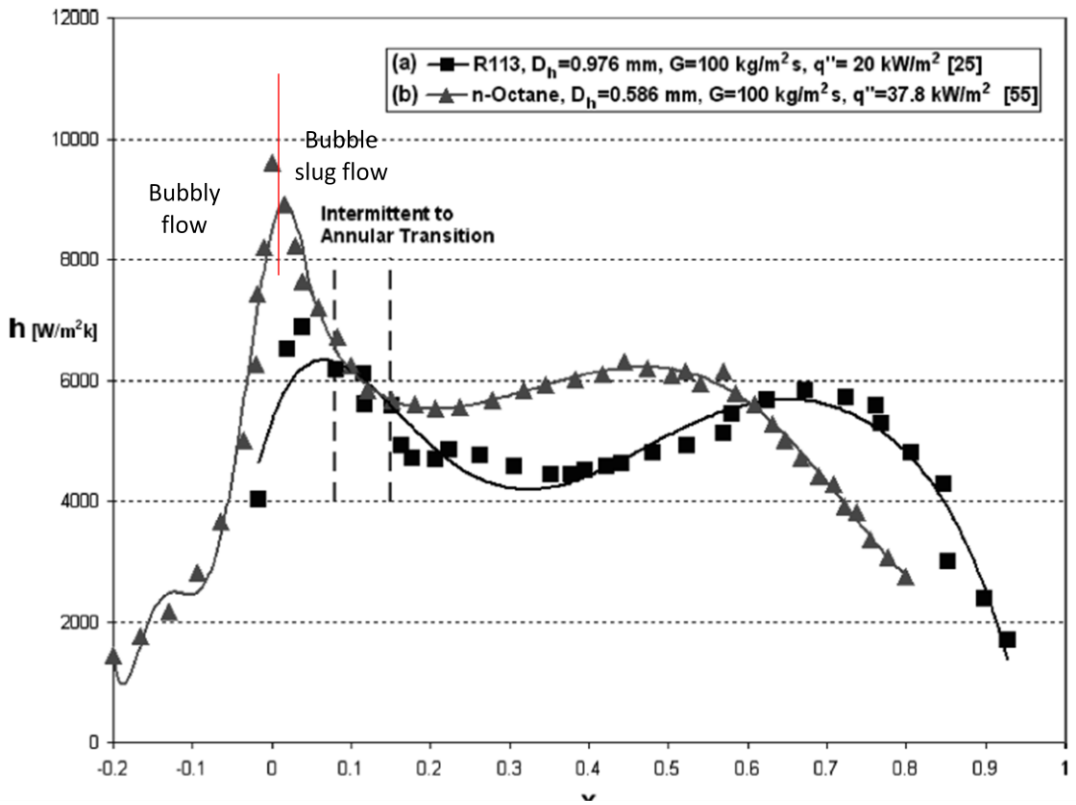

Figure 1.3. Characteristic heat transfer coefficient curve in microchannels (Bar-Cohen and Rahim 2009).

As shown in Figure 1.3, before annular flow, dry-out area between vapor slugs and solid walls would lead to rapidly increase of wall temperature and decrease of heat transfer coefficient. It implied that different flow pattern has different heat transfer mode. Nucleate boiling dominates the bubbly flow and thin-film evaporation dominates vapor slug flow and annular flow. Such two-phase flow instabilities are characterized by low frequencies and large amplitudes of flow rate, pressure drops, and heat transfer coefficients (Boure, Bergles et al. 1973;Bergles and Kandlikar 2005). These oscillations of heat transfer usually result in unstable wall temperatures and premature CHF.

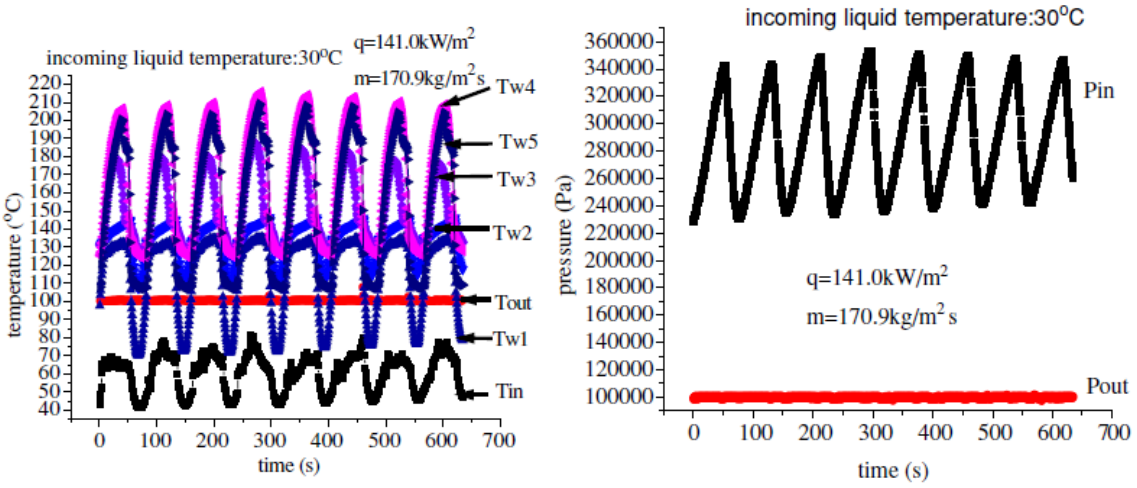

Figure 1.4. The oscillation of temperature and pressure during flow boiling in microchannels (Wu, Cheng et al. 2006).

These instabilities during flow boiling are negative for both mass and heat transfer. For constant pump power or pressure drop, the mass flux during two-phase flow would oscillate so that a stable mass transfer process could not be sustained and temperature/heat transfer coefficient would be also unstable at certain constant heat flux, as show in Figure 1.4. And large-amplitude low-frequency oscillation occurs during flow boiling in microchannels. Consequently, premature CHFs were observed in many previous studies (Bergles and Kandlikar 2005;Kuo and Peles 2008). Thus, the applications of microscale two-phase transport are restricted. The transitional flow patterns shall be regulated and managed so that these instabilities during flow boiling in microchannels could be suppressed and overall performance could be enhanced.

CHAPTER 2

CONTROLLING MICROSCALE TWO PHASE TRANSPORT

Toward sophisticated control of microscale two phase transports, the flow instabilities shall be suppressed by controlling bubble dynamics inside microchannels. The transport phenomena in flow instabilities are extremely complex, so that predictions of bubble dynamics usually rely on empirical correlations according to experimental data. There is lack of management of bubble dynamics to revolutionarily improve the performance of microscale two phase transport. From nanoscale to microscale, novel concepts should be developed and demonstrated for achieving higher performance. In this dissertation, three methods are demonstrated to effectively control microscale two-phase transport thru managing bubble dynamics at micro/nanoscale.

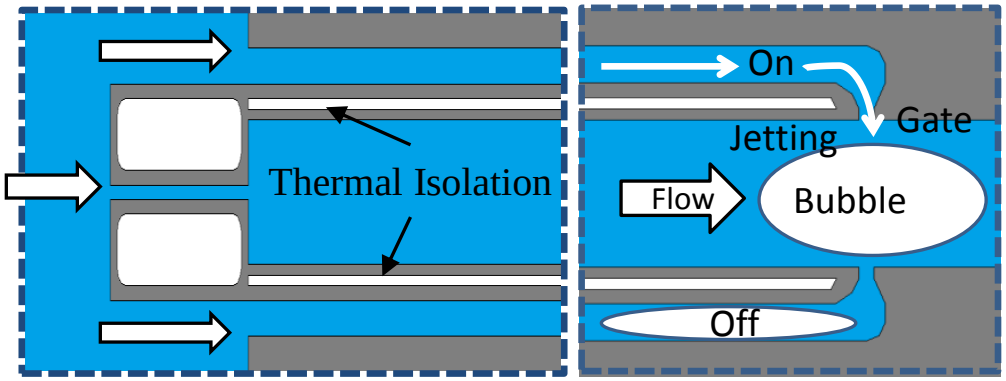

Figure 2.1. High frequency microbubble excited and modulated oscillations in microchannels.

Creating such high frequency two-phase oscillations (HF-TPOs) remains an important goal in advancing microscale fluidic logic devices, micro-mixers, micro-actuators, and flow controls. However, thermally driven TPO frequency has been hindered by confinement of compressible vapor bubbles and low thermal diffusivity in microfluidic systems. The first control method is to convert the intrinsic high-amplitude low-frequency oscillations into low-amplitude high-frequency oscillations. In Figure 2.1, a mechanism creating high frequency microbubbles growth/collapse cycle has been developed to achieve HF-TPOs. A "microfluidic transistor" was conceptualized and fabricated to passively sustain and modulate HF-TPOs. Three orders of magnitude higher TPO frequency has been achieved compared to TPOs reported in literatures under similar working conditions . It can also create and sustain strong mixing in microchannels. This mechanisum occurs in a microchannel architecture consisting of a main channel connected to two secondary channels. And it was shown to significantly enhance flow boiling heat transfer in microchannels. Experimental studies are carried out at mass fluxes ranged from 150 kg/m^2 s to 480 kg/m^2 s by using water as working fluids. Compared with microchannels with inlet restrictors and reentrant cavities, the average two-phase heat transfer coefficient has been improved by up to 88 % with 71 % to 90 % reduction in pressure drop under similar working conditions. Critical heat flux of 552 W/cm^2 at a mass flux of 480 kg/m^2 s was demonstrated. Flow and heat transfer mechanisms were studied and discussed.

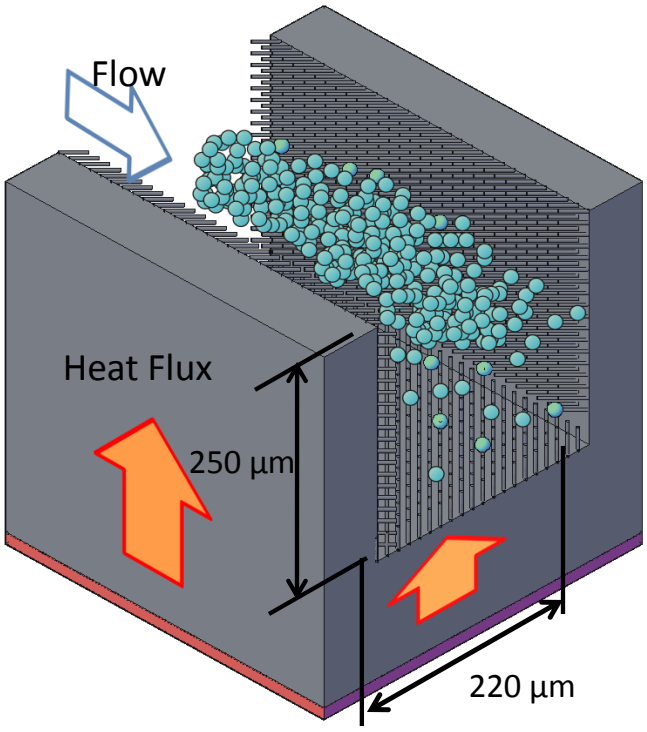

Figure 2.2. The single and periodic annular flow by generation nanobubbles in microchannels.

Figure 2.2 describes the second control method to directly manage bubble nucleation, growth and departure by applying silicon nanowired interfaces on all inner walls of microchannels. Furthermore, transitional flow boiling regimes in microchannels can be reduced to a single and periodic annular flow from the onset of nucleate boiling to the critical heat flux condition. Hydrophilic silicon nanowires directly grown on inner walls of microchannels were tailored to create boiling surfaces with optimal submicron pores surrounded by nanogaps through controlling the height and density of silicon nanowires using the nanocarpet effect. The single two-phase regime was realized by controlling the flow structures in two aspects: reducing bubble size and transforming the dominant surface tension force from the cross-sectional plane to the inner-wall plane.

Then, flow boiling in silicon (Si) microchannels was dramatically enhanced on deionized water in a single and periodic annular flow boiling regime enabled by Si nanowired inner walls. The mechanism of enhanced flow boiling heat transfer, reduced pressured drop and enhanced critical heat flux (CHF), respectively, are demonstrated and characterized in this dissertation. Compared to the flow boiling in plain-wall microchannels without applying inlet restrictors (IRs), the average heat transfer coefficient (HTC) and CHF under the single annular flow were enhanced up to 326% and 317% at a moderate mass flux of 389 kg/m ^{2}s. Additionally, compared with the flow boiling in microchannels with IRs, the HTC of flow boiling in the single and annular flow was enhanced up to 248%; while CHF in the new flow boiling regime was 6.4-25.8% lower. The maximum HTC reached 125.4 kW/m^2 K at a mass flux of 404 kg/m ^{2}s near the exits of microchannels. The significantly promoted nucleate boiling, induced advections, and enhanced thin-film evaporation in the self-stabilized and single flow boiling regime should be the primary reasons behind the dramatically enhanced flow boiling.

Moreover, comparing microchannels with smooth walls under similar working conditions, we report that pressure drops were reduced approximately 50% and critical heat flux (CHF) was enhanced approximately 300% in the single and periodic flow boiling regime enabled by superhydrophilic Silicon nanowires (SiNWs). The hydraulic characteristics of the single and periodic annular flow were systematically investigated to understand mechanisms of reduced pressure drop and enhanced CHF. In the new flow boiling pattern, the liquid and vapor flows were separated during the entire flow boiling process, i.e., from the onset of nucleate boiling to the CHF conditions.

The capillary flows induced by SiNWs also work as liquid lubrication layers. These two characteristics (flow separation and capillary flows) lead to the dramatic reduction of frictional pressure drop at the vapor-liquid interface and hence a reduction of the pressure drops at system level. The global and local liquid supply resulting from the rapid rewetting flows and capillary flows was greatly improved and consequently, resulted in a dramatic CHF enhancement without applying inlet restrictors. In this dissertation, the range of Reynolds number based the vapor flow at exit was from 0.1 to 2200.

The schematic map of the third method is shown in Figure 2.3, Si nanotips fences along the vertical walls of monolithic silicon microchannel arrays are fabricated by modified DRIE process and used to generate an artificial boundary layer and transform the direction of surface tension force from the cross-section plane to in-wall planes. In the same time, capillary flows are generated by surface tension force along these Si nanotips. Thus, the vapor slugs, which usually induce compressible volume, flow instabilities and local dry-out, are observed to collapse within microschannels. The dramatically enhanced CHF of flow boiling in microchannels was experimentally demonstrated and systematically characterized. CHF was enhanced up to ~448 W/cm^2 at a moderate mass flux of 303 kg/m ²s on deionized (DI) water. Comparing to flow boiling in microchannels with smooth walls, CHF was enhanced between 234 % and 275 % with mass flux varying from 160 to 303 kg/m ²s.

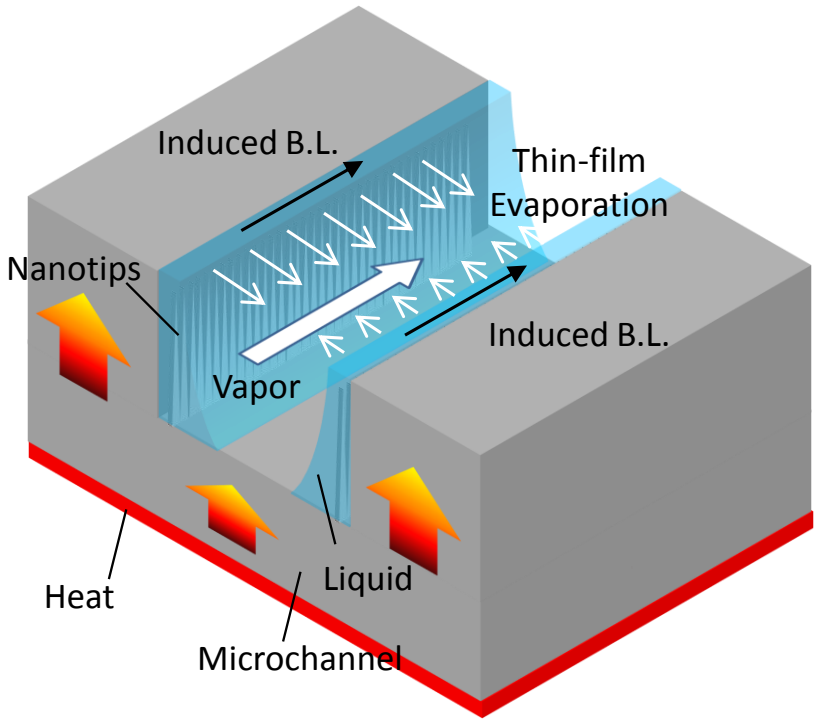

Figure 2.3. The functional boundary layers inside microchannels.

Generally, heat transfer and CHFs are enhanced and pressure drops are reduced at the same time by managing bubble dynamics and controlling two-phase transport inside microchannels. The experimental and theoretical studies of above three methods are discussed in the following chapters.

CHAPTER 3

HIGH FREQUENCY MICROBUBBLE EXCITED AND MODULATED OSCILLATIONS

Two-phase flow instabilities are challenging issues hindering the practical implementation of flow boiling in micro domains. Practically, flow instability in microchannels leads to premature CHF condition at low exit vapor quality (Boure, Bergles et al. 1973;Wu and Cheng 2004;Bergles and Kandlikar 2005;Chang and Pan 2007;Peles 2012). Generally, there exist static and dynamic flow instabilities in microscale flow boiling. The dynamic flow instabilities are characterized as pressure drop oscillation, density-wave oscillation and thermal oscillations (Bergles and Kandlikar 2005). And most flow instabilities are associated with two-phase oscillation (TPO) frequencies that range from 0.06 Hz to 2 Hz in the laminar flow regime (Boure, Bergles et al. 1973;Wu and Cheng 2004;Bergles and Kandlikar 2005;Chang and Pan 2007;Peles 2012). And these intrinsic oscillations are low-frequency and large-amplitude fluctuations (Wu and Cheng 2004;Balasubramanian and Kandlikar 2005;Xu, Zhou et al. 2005;Wang, Cheng et al. 2007;Wang, Cheng et al. 2008). Thus, these low-frequency flow fluctuations can induce delayed rewetting, then local dry-out between heated walls and attached vapor bubbles, and hence, lead to premature CHF conditions. High frequency TPOs, whose frequency are two or three magnitudes higher, are most commonly achieved through active-controlled microsecond heating pulses with significant sacrifice of volumetric flow rates (Wu and Cheng 2003;Qu and Mudawar 2004;Wu and Cheng 2004;Xu, Liu et al. 2009;Liu, Xu et al. 2010).

Recent studies demonstrated that novel configurations of microchannels can suppress boiling instabilities and enhance several key flow boiling parameters including onset of nucleate boiling (ONB), heat transfer coefficient (HTC), and CHF (Chen, Chen et al. 1997;Andersson, van der Wijngaart et al. 2001;Deng, Lee et al. 2003;Liu, Xu et al. 2010). An example of reported configurations is inlet restrictors (IR) or valves/orifices to overcome reverse flows and mitigate flow boiling instabilities (Thome 2006;Cheng, Wang et al. 2009;Kandlikar 2012). Several studies have shown that other configurations, such as impingement jets, can effectively suppress flow reversal and at the same time enhance HTCs and CHFs (Qu and Mudawar 2003;Kandlikar, Kuan et al. 2006;Kosar, Kuo et al. 2006;Wang, Cheng et al. 2008).

Although the aforementioned techniques successfully enhanced nucleate boiling and suppressed the flow instabilities in micro-scale systems, the additional pressure drop (Δp) and power requirements introduced by those configurations are major hindrance. For example, inlet restrictors or orifices can effectively suppress flow instabilities and enhance CHF (Mudawar 2001;Liu, Tong et al. 2004;Bar-Cohen, Arik et al. 2006;Kandlikar and Bapat 2007), but, they increase the pressure drop by up to five-folds. High flow resistance can cause critical issues, such as high pumping power and coolant leakage. In this study, inlet restrictors are used to confine vapor slugs in microchannels however two secondary channels are added thru a cross junction to induce secondary sub-cooled flow, which not only reduce flow resistance and works as artificial nucleation sites but also create strong mixing by collapse of vapor slugs in the main channel.

It is a challenging task to passively generate appreciable mixing in microchannels without the participation of active controllers because two-phase flows in microchannels

are dominated by viscous and capillary flows (Kandlikar, Kuan et al. 2006;Kosar, Kuo et al. 2006;Chang and Pan 2007), which tend to suppress mixing. This, in turn, is detrimental to heat transfer at the micro scale as mixing enhances advection heat transfer. In order to create strong mixing in microchannels, a mechanism similar like water hammer is used in this study. The non-sustainable water hummer pulses driven by bubble growth and collapse have been observed and modeled in a single microchannel (Kandlikar 2010). Self-sustainable high frequency *TPO*s (pulses) powered by vapor bubble growth and collapse in microchannels were successfully demonstrated in previous study (Yang, Dai et al. 2012). In this study, significant flow boiling heat transfer enhancement under constant heat fluxes was achieved. The high frequency oscillations and enhanced heat transfer were enabled by this new microchannel architecture. Similar to microchannels with *IRs*, high *CHF* values and suppression of flow instabilities were observed. Moreover, *HTC*s were greatly enhanced with significant reduction in the pressure drop because of the introduction of secondary channels. The working mechanisms of heat transfer enhancement under investigation are discussed and revealed through visualization study. Further optimization is proposed.

3.1 EXPERIMENTAL PROCEDURES

In this section, the structures of micro testing chips, testing setup and micro/nanofabrication are introduced.

3.1.1 DESIGN OF A NOVEL MICROCHANNEL ARCHITECTURE

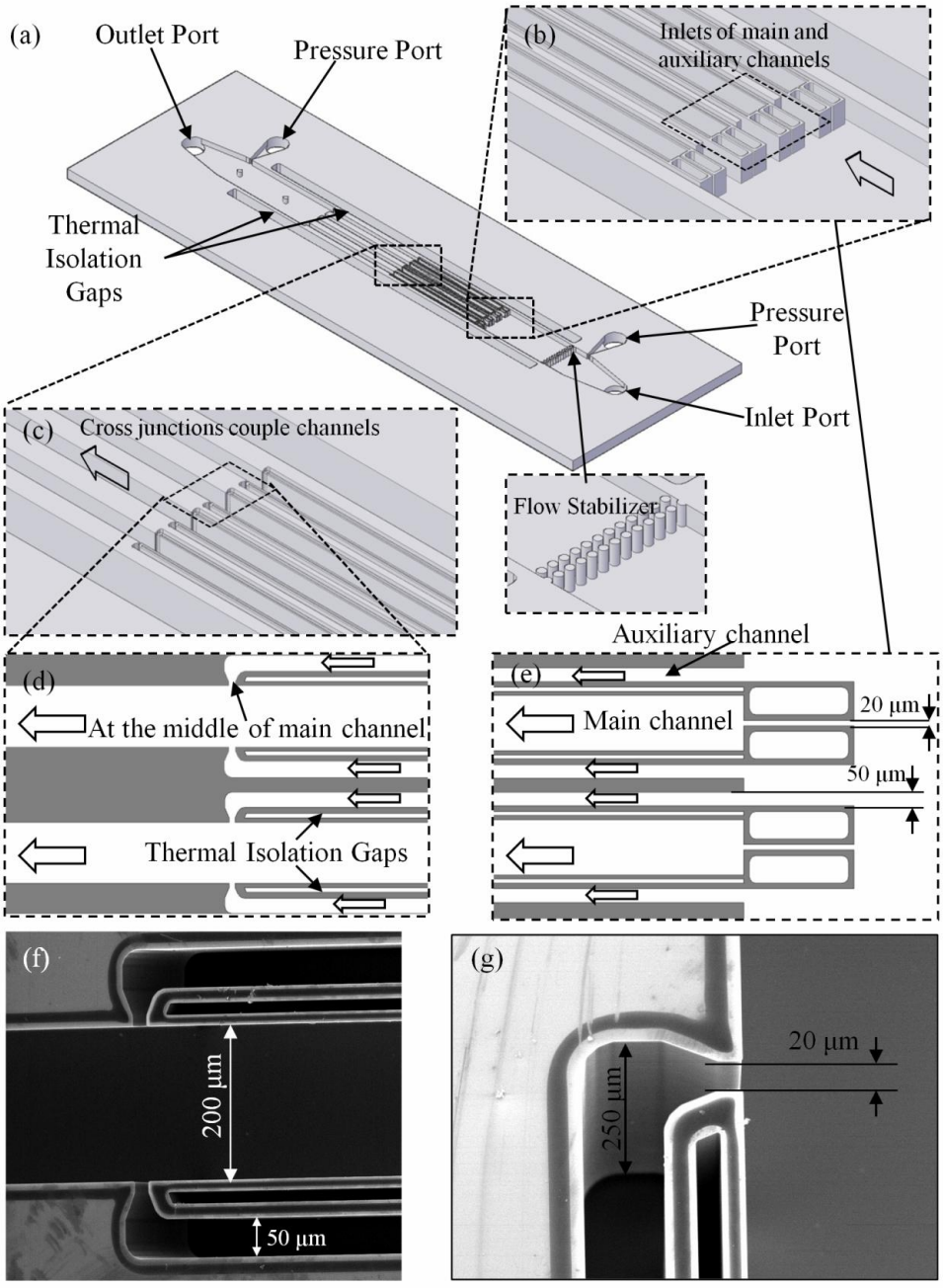

Figure 3.1 (a) 3D CAD model of the present microchannel architecture, (b) and (c) magnified views of entrance and cross-junction structures, (d) and (e) top-viewed of cross-junctions and entrances, (f) and (g) SEM images of the cross-junction.

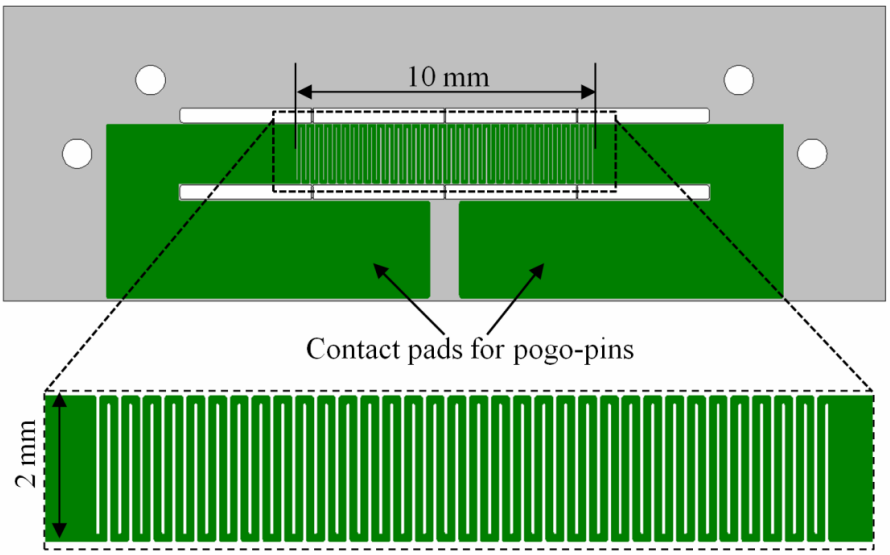

Figure 3.2. Built-in micro heater (dimension in mm).

The micro device consists of four main channels (*H*=250 μm; *W*=200 μm; *L*=10 mm) each connected to two auxiliary channels (*H*=250 μm; *W*=50 μm; *L*=5 mm) coupled at a cross junction (Figure 3.1). The auxiliary channels were open to the inlet manifold (Figure 3.1e), but *IRs* (*H*=250 μm; *W*=20 μm; *L*=400 μm) were placed in the inlet to each main channels. A 1 mm diameter inlet port, 1 mm diameter outlet port, and two 1 mm diameter pressure ports were fabricated in the micro heat exchanger. The inlet to exit pressure drop was measured between two pressure ports. To minimize heat loss, two thermal isolation gaps (air gaps) were etched on both sides of microchannel arrays as shown in Figure 3.1a. Flow stabilizers at the entrance to the inlet manifold were formed to evenly distribute the flow. All channels shared identical depth of 250 μm. The inlet restrictors are 400 μm long and 20 μm wide. Additionally, air gaps were etched between the auxiliary channels and the main channels to reduce the conjugation heating and hence decouple thermal interaction between channels. Two openings on both sidewalls of the main channel were made as shown inFigure 3.1f. This structure connects the two

auxiliary channels at the middle of a main channel. The width of the opening on the wall between the auxiliary channels and the main channels was 20 μm (Figure 3.1g).

A micro heater, which was patterned by a thin film of aluminum, was deposited onto the back side of silicon microchannels (

Figure 3.2). The heater area (10 mm × 2 mm), which was identical to the total base area of microchannel arrays and walls, served as a thermistor to measure the average temperature of the heater.

3.1.2 DESIGN AND FABRICATION OF THE MICROCHANNEL DEVICE

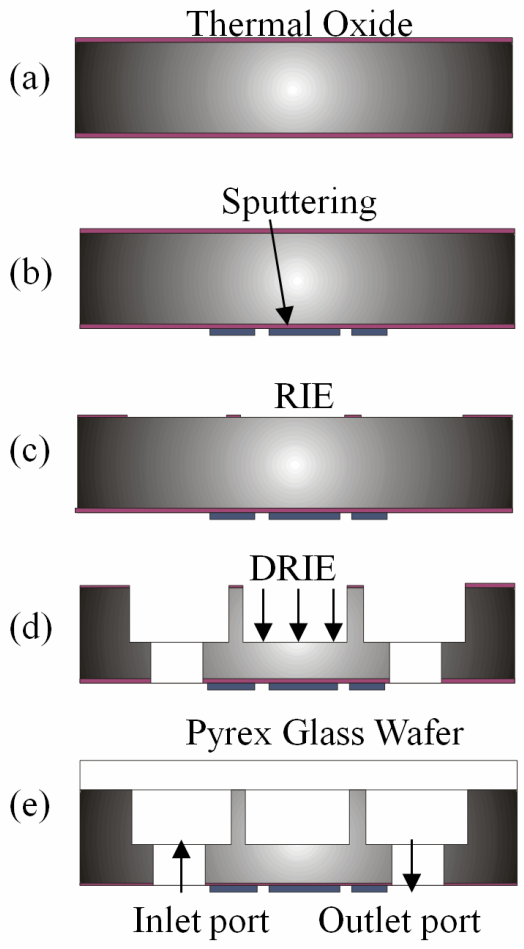

Figure 3.3. Major microfabrication steps.

The microchannel heat exchangers were made from a silicon wafer bonded to a Pyrex wafer by standard microfabrication processes (Figure 3.3). This process started

with a double-side-polished n-type <100> silicon wafer. First, 1 μm thick thermal oxide layers were grown on both side of the silicon wafer. The silicon oxide film provided electrical insulation for the micro heaters and acted as a mask for deep reactive ion etching (*DRIE*) in subsequent microfabrication steps. An additional 500 nm thick oxide layer was then deposited onto the front side as a shield layer by plasma-enhanced chemical vapor deposition (PECVD). Next, a 7 nm thick adhesive layer of titanium was deposited on the backside of the silicon wafer by *DC* sputtering followed by a 1 μm thick layer of aluminum. Once the thin films were successfully deposited, a thin film heater was made on the backside of the wafer by photolithography and wet etching (Figure 3.3b). A 500 nm thick PECVD oxide layer was then deposited to protect the thin film heater in the subsequent fabrication processes.

After the heater was formed on the backside, a pattern of microchannels on the top side of the wafer were formed on the silicon oxide through photolithography and reactive ion etching (RIE), which served as a mask. The area under the oxide mask was protected and the remaining areas were etched out to create 250 μm deep trenches by DRIE. The DRIE process formed deep vertical sidewalls with a root mean square(*RMS*) roughness of ~300 nm (Fogg and Goodson 2009). An inlet port, an outlet port, air gaps, and pressure ports were formed on the backside of the wafer by *DRIE*. Photolithography and wet etching (6:1 buffered oxide etchant) was used to remove patterned oxide in preparation for *DRIE*. Then through holes were etched through the wafer by *DRIE* (Figure 3.3d). *RIE* was used to remove patterned oxide coatings on the backside to expose the contact pads.

A Pyrex glass wafer was anodically bonded to the silicon substrate to seal the device as shown in Figure 3.3e. The transparent glass cover also served as observation windows in the visualization studies. The individual microchannel test chips (length 30 mm; width 10 mm; thickness 1 mm) were cut from the wafer by a dicing saw.

3.1.3 EXPERIMENTAL SETUP

Figure 3.4 depicts the two-phase apparatus used to conduct experiments. The microchannel test chip was placed at the middle of the test package module (Figure 3.4). This test package module provides hydraulic ports and electrical connections. Mechanical fasten units consist of two fasten bolts and two holding clamps. These units fix and fasten the microchannel test chips by mechanical force. The microchannel test chips were fixed at two ends, but with the middle suspended. This packaging was designed to minimize the tighten stresses on the thin film thermistors/heater and to reduce heat loss. Six micro o-rings between the silicon microchannel test chip and the test package were used to achieve mechanical seals. Probe-pins were placed under the backside of the device and two bolts were used to adjust the heights of the probe-pins to minimize electrical contacts resistance. Two pressure transducers were connected to the pressure ports to measure pressure drops.

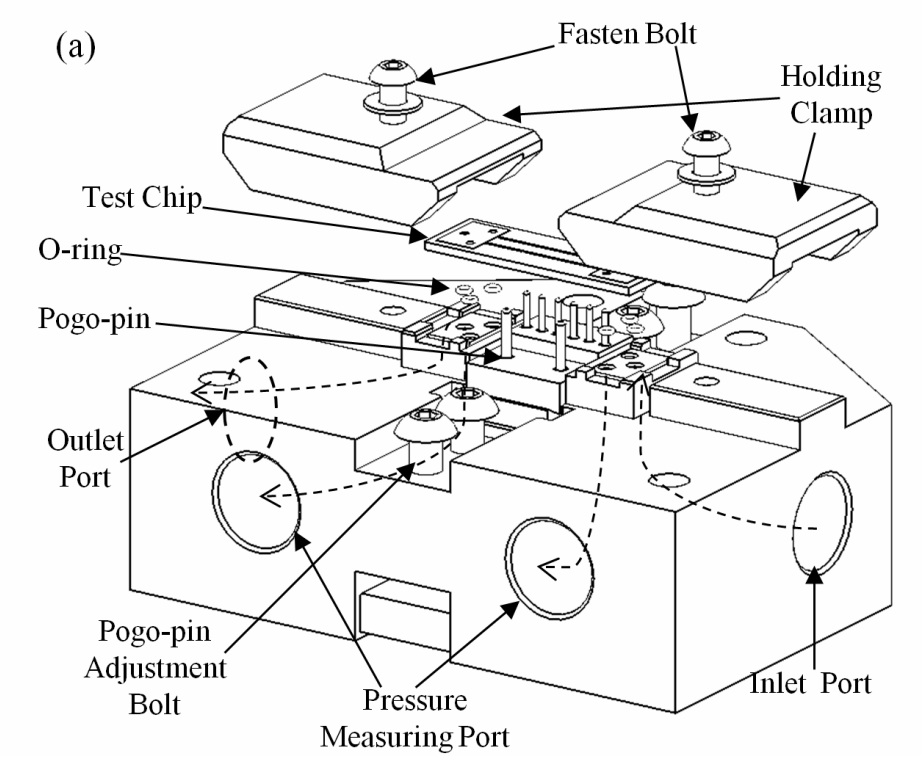

Figure 3.4. An exploded 3D model of testing package module, which provide hydraulic and electrical connections.

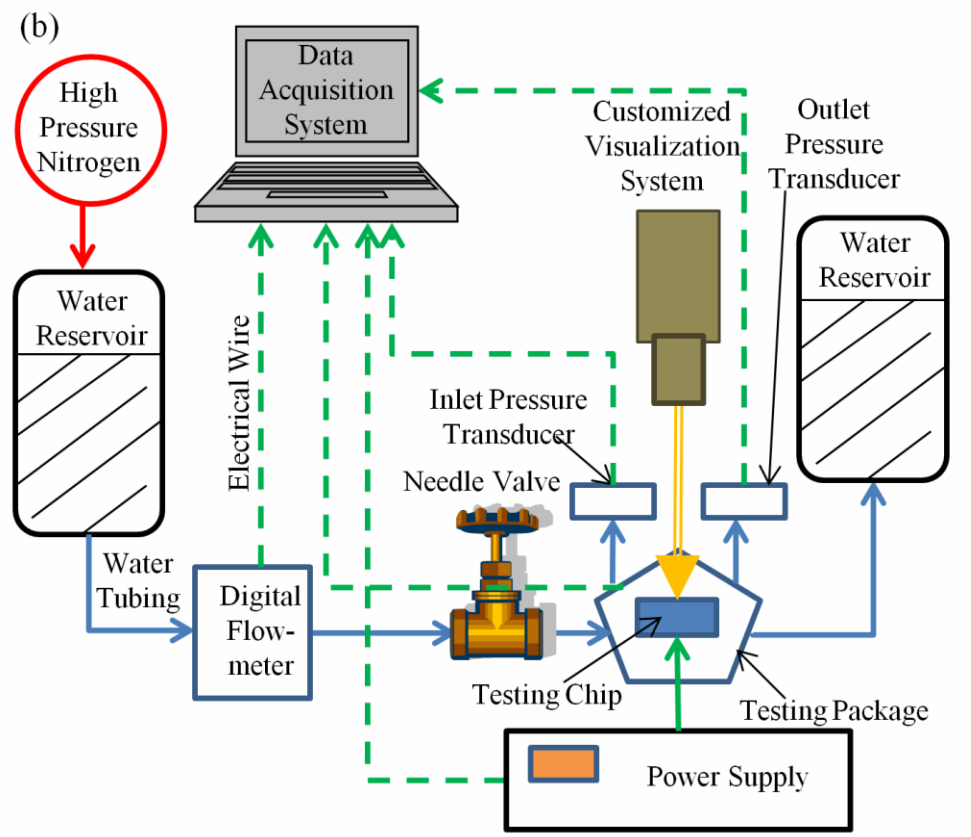

Figure 3.5. The two-phase testing platform.

Major components of the experimental setup include an optical imaging system, a data acquisition unit, and an open loop for coolant supply (Figure 3.5). A pressurized water tank was used to supply de-ionized (*DI*) water, which was pre-degassed prior to tests and pumped by compressed nitrogen (N_2). Mass fluxes were measured by Sensiron ASL1600 flowmeter with 0.03 kg m^{-2} s^{-1} resolution. Electrical power was supplied by a high precision digital programmable power supply. The partial voltage on the micro heater was measured by an Agilent digital multimeter. Two thermocouples were used to measure the inlet and outlet fluid temperatures. Flow rate, local pressures, inlet and outlet temperatures, and the heater's voltages and currents were recorded automatically by a customized data acquisition system developed from NI LabVIEW. A visualization

system comprised of a high-speed camera (Phantom V 7.3) with 256 x 256 pixels at approximate 40,000 frames per second and an Olympus microscope (BX-51) with 400× amplifications was developed to study bubble dynamics.

3.1.4 TESTING PROCEDURE

Prior to experiments, the heat loss as a function of temperature difference between a micro heat exchanger and the ambient was evaluated. The temperature of the device in steady state was plotted as a function of input heat fluxes without fluid flows. Thus, the heat losses as a function of steady state temperature difference was obtained by linear curve fit. The curve was then used to estimate heat loss with high accuracy (Vengallatore, Peles et al. 2004). The heater, which also functions as a thermistor, was calibrated in an isothermal oven with a proportional–integral–derivative (PID) controller. The temperature as a linear function of electric resistance was generated using a linear curve fit. The confidence of correlation coefficient was estimated to be higher than 0.9999. The line slope is denoted by S_l.

After assembly of the microchannel device on the test package, the flow rate was kept constant at a set value ranging from 150 kg/m^2 s to 480 kg/ m^2 s. Uniform heat flux was applied by a digital power supply through the heater at a step of approximate 2 W until *CHF* conditions. At each step, the data acquisition system recorded 120 sets of steady state experimental data including voltages, currents, local pressures and temperatures of inlet and outlet in four minutes intervals.

3.1.5 DATA REDUCTION

The electrical input power and resistance of the heater was calculated as, respectively,

$$P = V \times I \tag{2}$$

and

$$R = V / I \tag{3}$$

Then heat loss P_{loss} between the environment and the testing chip is deducted from *P*. The effective power

$$P_{eff} = P - P_{loss} \tag{4}$$

The heat loss is measured before testing. The average temperature of the thermistor (i.e., the thin film heater) was calculated as,

$$\bar{T}_{heater} = S_l (R - R_a) \tag{5}$$

where R_a is the resistance of the micro heater at room temperature. The average wall temperature of the base area of the microchannel heat exchanger was estimated from the heater as

$$\bar{T} = \bar{T}_{heater} - \frac{q''_{eff} t}{k_s} \tag{6}$$

where $q''_{eff} = P_{eff} / A_b$.

The microchannels length (*L*) was divided into two sections: single-phase region (L_{sp}) and two-phase region (L_{tp}) (Figure 3.7). The length of the two sections was observed to vary significantly with exit mass quality as shown from Figure 3.7 b to d. The average two-phase heat transfer coefficient, $\bar{h}_{tp}$, was used to evaluate flow boiling heat transfer performance in the two-phase region (L_{tp}) by excluding the weight of the single-phase heat transfer from the average temperature. The single-phase heat transfer coefficient was calculated as,

$$\bar{h}_{sp} = \frac{P_{eff}}{\left[A_t - NA_f(1-\eta_f)\right]\left[\bar{T}_{sp} - (T_i + T_e)/2\right]} \tag{7}$$

where the pin fin efficiency was estimated from $\eta_f = \tanh(mH)/mH$ and $m = \sqrt{2\bar{h}_{sp}(L+W)/k_s WL}$. The average temperature in the single-phase region is the mean value of the inlet and exit surface temperatures in this region.

$$\bar{T}_{sp} = \frac{T_{in,sp} + T_{exit,sp}}{2} \tag{8}$$

In the above equation, the inlet and the exit surface temperatures were estimated as,

$$\begin{aligned} T_{in,sp} &= T_i + \frac{P_{eff}}{\bar{h}_{sp} A_s}; \\ T_{exit,sp} &= T_{sat} + \frac{P_{eff}}{\bar{h}_{sp} A_s}; \end{aligned} \tag{9}$$

The average temperature of the two-phase heat transfer region, $\bar{T}_{tp}$, was obtained by a weighted average method (Kosar, Kuo et al. 2005) in terms of the single-phase and average wall temperatures:

$$\bar{T}_{tp} = \frac{\bar{T}L - \bar{T}_{sp} L_{sp}}{L_{tp}} \tag{10}$$

These length values (L_{sp} and L_{tp}) were measured through visualization. Taking into account fin effects on a single microchannel, the average two-phase heat transfer coefficient was calculated as,

$$\bar{h}_{tp} = \frac{P_{eff}}{(\sum(WL + 2HL\eta_f))(\bar{T}_{tp} - T_{sat})} \tag{11}$$

Because the thermal conductivity of Pyrex glass is approximately 1% of silicon, the interface between the microchannel walls and cover glass was assumed to be

thermally insulated in the fin approximation. Then, $\bar{h}_{tp}$, was iteratively obtained from Eq. 1 through 9. Additionally, the exit vapor quality was calculated with mass flow rate and net input power according to:

$$\chi = \frac{P_{eff} - \dot{m}C_p(T_{sat} - T_i)}{\dot{m}h_{fg}} \tag{12}$$

3.1.6 UNCERTAINTY ANALYSIS

Uncertainties of experimental variables are given in Table 1. Uncertainties of measured values were adopted from the manufacturers' specification sheets, and the uncertainties of derived variables were calculated according to the propagation of uncertainty analysis (Kosar, Kuo et al. 2005).

Table 3.1. Uncertainties of major parameters.

Name of Variables	Errors
Flow rate, Q	0.05%
Voltage on the heater, V	0.10%
Current on the heater, I	0.10%
Ambient Temperature, T_a	0.1 ˚C
Electrical power on the heater, P	0.20%
Electrical resistance, R	0.20%
Average temperature, $\bar{T}$	0.8 ˚C
Heat transfer coefficient, $\bar{h}$	2.20%

3.2 RESULTS AND DISCUSSION

3.2.1 FLOW BOILING CURVE

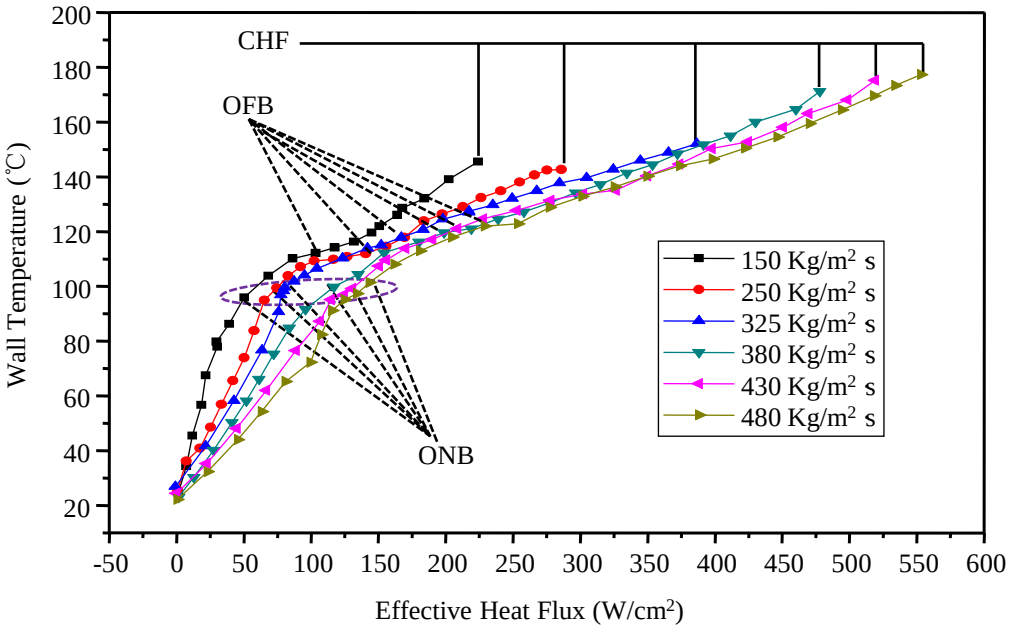

Figure 3.6. Boiling curves: average wall temperature $\bar{T}$ versus q''_{eff} .

The average wall temperature as a function of effective heat flux at different mass fluxes is shown in Figure 3.6. Boiling curves: average wall temperature $\bar{T}$ versus q''_{eff} .. Bubbly flow was observed following ONB (Figure 3.7a and Figure 3.7b) during which the mass quality was relatively low so that interactions between isolated bubbles are not significant. In this study, ONB was greatly reduced to approximately saturated temperature, i.e., 100 °C. The average superheats at *ONB* in this study is approximately 2 °C, which is significantly lower than prediction from Liu et al. model (i.e., ~12 °C) (Kline and McClintock 1953). In the current microchannel architecture, the nozzles/openings on the side walls of the main channels Figure 3.1g) appears to function as artificial nucleate cavities that reduce the superheat temperature at ONB similar to observation in previous studies on engineered surfaces in microchannels (Liu, Lee et al.

2005). Figure 3.7a and Figure 3.7b shows that bubbles were initially nucleating near the nozzles on the side walls and propagating in the posterior region of the main channels (L_{tp}). Onset of fully developed boiling (OFB) was defined as the first occurrence of nucleate boiling in all sections of the microchannels including the main channels (L_{sp} section in Figure 3.7a) and the auxiliary channels. When heat fluxes exceeded *OFB*, explosive bubbles grew inside the microchannels leading to direct condensation of vapor slugs, and hence complete collapse of the slugs in the microchannel (Figure 3.7b). As a result, the high frequency microbubble-excited and -modulated two-phase oscillations were successfully created to dramatically enhance flow boiling heat transfer. The detailed oscillation mechanism has been detailed in previous study (Kosar, Kuo et al. 2005;Kuo, Kosar et al. 2006;Kuo and Peles 2008).

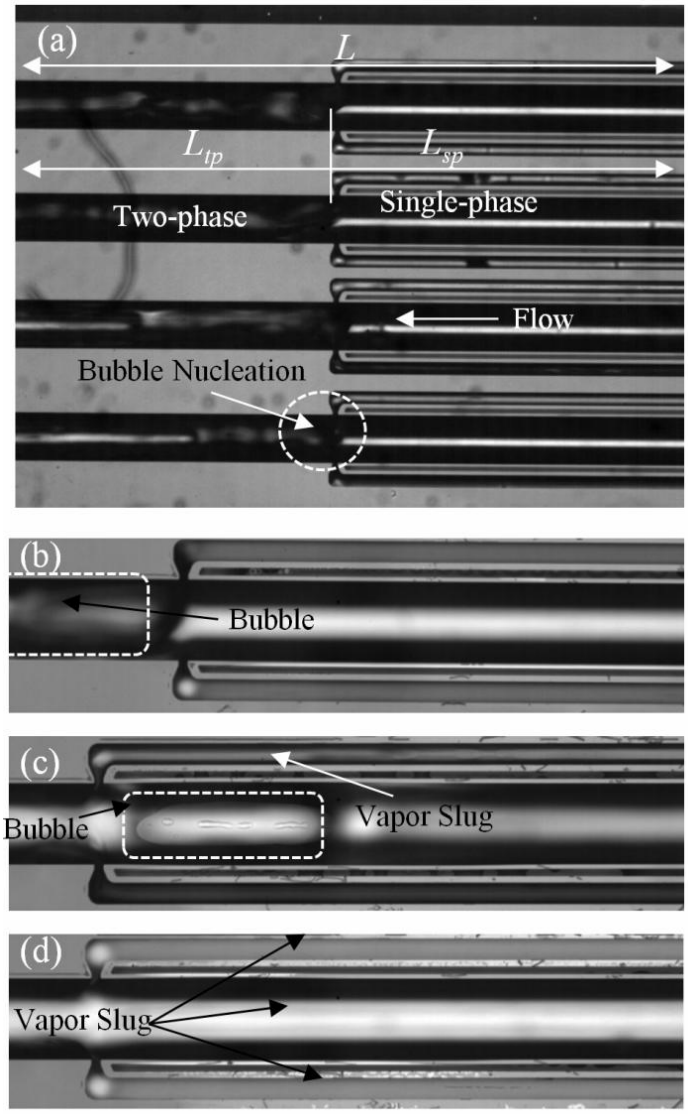

Figure 3.7. (a) Single-phase flow and two-phase flow in the present microchannel architecture during subcooled flow boiling. (b) Bubble growth at incipient boiling stage, $\chi = 0.10$. (c) Vapor slugs in all sections of microchannel during fully developed boiling, $\chi = 0.27$. (d) Persistent vapor slug was observed, which cannot be removed in the front section of a main channel when boiling was approaching CHF, $\chi = 0.49$.

3.2.2 TWO-PHASE HEAT TRANSFER

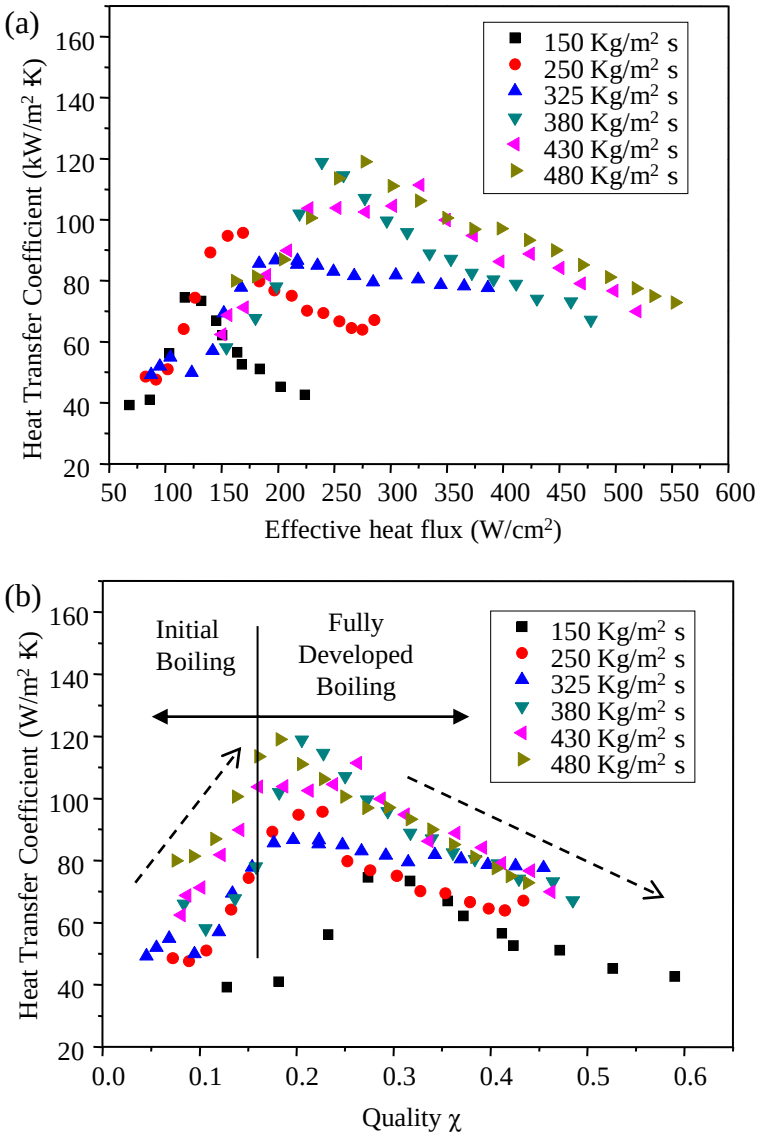

Figure 3.8. (a) Average two-phase heat transfer coefficient $\bar{h}_{tp}$ versus effective heat flux q''_{eff}, (b) $\bar{h}_{tp}$ versus exit vapor quality χ.

The boiling curves are plotted in Figure 3.6. Then, two-phase heat transfer coefficient as a function of effective heat flux and mass quality is depicted in Figure 3.8. The heat transfer coefficient initially increased with heat flux during fully developed boiling and then gradually decreased.

The bubble ebullition cycle started near the nozzles (highlighted by the dashed line in Figure 3.7b). When heat flux was below the threshold required inducing explosive boiling, and hence, to activate two-phase oscillations, the single-phase region (L_{sp}) and two-phase region (L_{tp}) had distinct boundaries (Figure 3.7a). With increasing heat flux, fully developed nucleate boiling gradually dominated in the front region of the main channels and in the auxiliary channels (Figure 3.7c). The corresponding heat transfer coefficients were observed to increase considerably until reaching a peak, which varies for different mass fluxes. As the mass quality increased, the two-phase heat transfer coefficients reached their maximum between exit qualities, χ, ranging from 0.15 to 0.3. The maximum heat transfer coefficient achieved in this study was approximately 120 $kW/m^2 \cdot K$ at G = 430 kg/m^2 s and G = 480 kg/m^2 s. The mechanism responsible for such high heat transfer coefficient is believed to be related to the strong mixing induced by the high frequency TPOs resulting from vapor slug growth/collapse process. The magnitude of TPO frequency was 100 Hz and the highest frequency in the present microchannel architecture was over 600 Hz (Yang, Dai et al. 2012). Heat transfer in microchannels during flow boiling is greatly enhanced by the strong mixing induced at such high frequencies. It is because that the high frequency of liquid rewetting, mixing promoted advection, and evaporation, and the induced cavitations nucleation of bubbles was promoted (Yang, Dai et al. 2012).

The gradual decline of the heat transfer coefficient is linked to the formation of vapor slugs with exit qualities above a certain threshold value in the main channels between the cross-junctions and the inlet (white areas) at high heat fluxes (Figure 3.7d) where the high frequency TPOs has not affected the flow. The absence of the high

frequency TPOs mixing, forced convection and rewetting resulted in nearly 50 % vapor-filled area and a decrease in the heat transfer coefficient. The appearance of such a vapor slug can be a result of the decline in condensation and increase in evaporation at a high heat flux. Optimization of the location and number of cross-junctions could improve this situation by increasing direct condensation rates.

3.2.3 COMPARISONS BETWEEN THE PRESENT ARCHITECTURE AND MICROCHANNELS WITH REENTRANT CAVITIES AND INLET RESTRICTORS

Comparisons between the current microchannel architecture and microchannels with reentrant cavities and inlet restrictors (Fogg and Goodson 2009) are shown in Figure 3.9 and Figure 3.10. In these figures, three types of architectures are compared to demonstrate enhancement and investigate its mechanism. These three different architectures use microchannels with the same length, width and height. Also, they all employ inlet restrictors to confine vapor vapor slugs and eliminate reverse flow. The base architecture is called I.R. architecture, which only use inlet restrictors without any

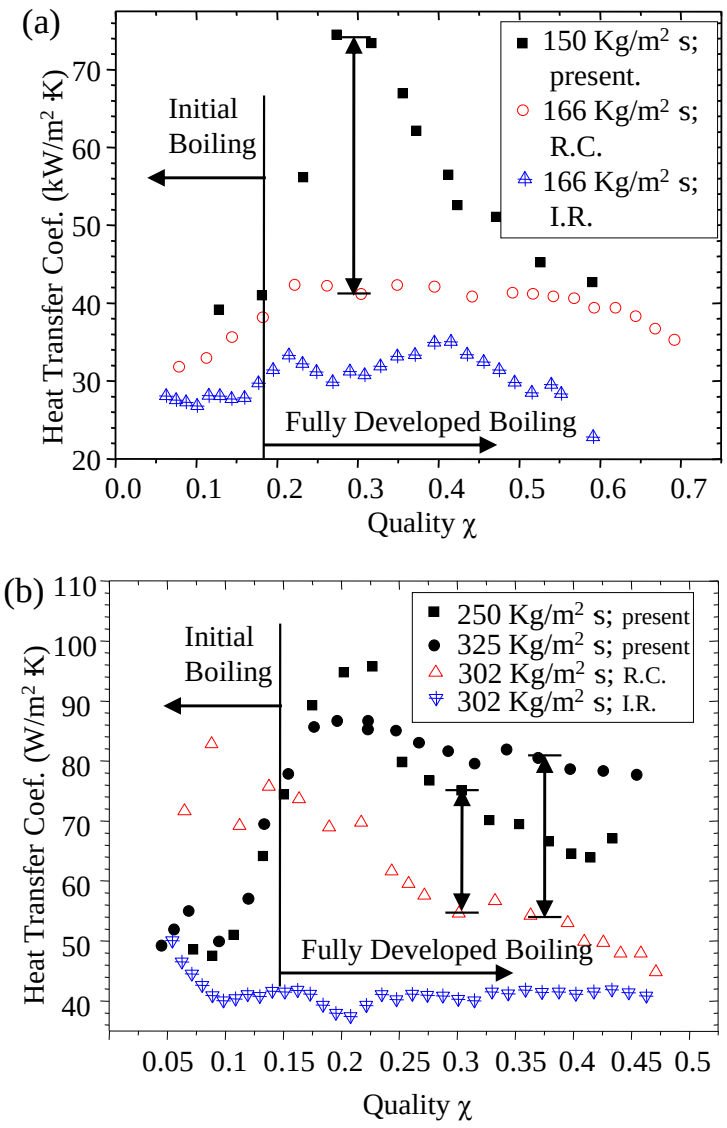

Figure 3.9. Comparing HTCs of present architecture with the R.C. architecture and the I.R. architecture, (a) at a low mass flux, and (b) at moderate mass fluxes. The I.R. architecture is parallel microchannel arrays with inlet restrictors (Kosar, Kuo et al. 2006;Schneider, Kosar et al. 2006) and the R.C. architecture is the I.R. architecture added with reentrant cavities (Kosar, Kuo et al. 2005).

other enhancing techniques. And in R.C. architecture, reentrant cavities are used to enhance nucleate boiling as artificial nucleation sites. Experimental data of R.C. architecture in Ref. (Kosar, Kuo et al. 2005) were selected because of the same

dimensions of the main channels and inlet restrictors. Additionally, all experimental data were reduced by the same method. Reentrant cavities have been demonstrated to enhance flow boiling in microchannels (Kosar, Kuo et al. 2005), which is also indicated by Figure 3.9. Although the overall heat transfer coefficient in the present study was significantly enhanced compared to microchannels with reentrant cavities and inlet restrictors (H. Kubo 1999;Kosar, Kuo et al. 2005;Kuo and Peles 2008), there were several interesting observations. First, at low vapor qualities, deviations in heat transfer coefficient between the present microchannel architecture and the R.C. architecture developed by Koşar et al. (Kosar, Kuo et al. 2005) is insignificant as shown in Figure 3.9a. Although the heat transfer coefficient was dramatically increased during fully developed boiling, the heat transfer coefficient in the new microchannels rapidly decline after reaching a maximum heat transfer coefficient and eventually overlapping with the boiling curve documented in (Kosar, Kuo et al. 2005). The enhancement is believed to be a result of the induced mixing at low mass qualities. The enhancement from the reentrant cavities is not significant at low heat fluxes for both designs. Furthermore, the heat transfer coefficient in the present heat exchangers are lower prior to reaching fully developed boiling than these reported in (Kosar, Kuo et al. 2005) for moderate mass fluxes (Figure 3.9b). The number of reentrant cavities are much larger in (Kosar, Kuo et al. 2005) than in the current microchannel architecture. The enhanced nucleation by reentrant cavities in (Kosar, Kuo et al. 2005) is the primary cause for the enhanced heat transfer when nucleate boiling dominates. However, heat transfer rate in the present device is above that reported in (Kosar, Kuo et al. 2005) during fully developed boiling, which suggests that the strong induced mixing inside the microchannels plays a critical role in enhancing

two-phase heat transfer. In summary, heat transfer coefficient in the present microchannel architecture was enhanced by up to 87 % (Figure 3.9a) and 57 % (Figure 3.9b) with approximately identical mass fluxes and heat fluxes compared to the configuration developed in (Kosar, Kuo et al. 2005).

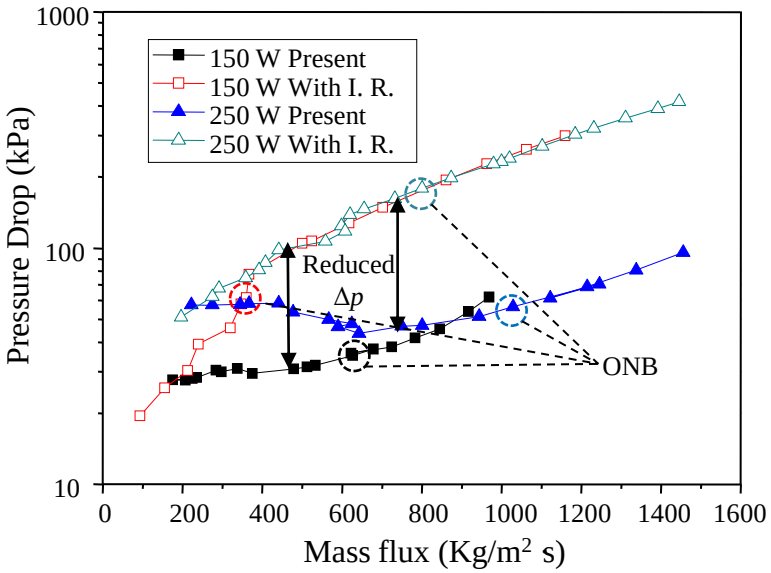

Figure 3.10. Δ*p*-*G* curves of flow boiling in present microchannel architecture and microchannels with I.R. configuration and reentrant cavities.

The pressure drop-mass flux (Δ*p*-*G*) curves for heat fluxes of 150 W/cm^2 and 250 W/cm^2 are shown in Figure 3.10. A pressure drop reduction between 71 % to 90 % compared to (Kosar, Kuo et al. 2005) for mass flux ranging from 400 kg/m^2 s to 1400 kg/m^2 s were observed. The primary objective of the microchannel architecture aims to create sustainable high frequency two-phase oscillations to promote flow boiling and to reduce hydraulic resistance by managing vapor slug expansion rate and introducing bypasses. The significant reduction of the pressure drop can be a result of the effective management of the confinements of compressible vapor bubbles enabled by high frequency bubble collapse as detailed in Section 3.3 as well as the increased cross-

sectional area from the auxiliary channels (Figure 3.1f). For mass fluxes below 400 kg/m^2 s, the Δp-G curves of the two configurations gradually converge because pressure drop of single-phase vapor flow is dominated.

Additionally, as illustrated in Figure 3.10, ONB in the present microchannels were observed to be greatly reduced compared to microchannels with smooth walls for a given heat flux. This can be because the nozzles on both walls of the microchannels also serve as artificial nucleation sites.

3.2.4 TWO-PHASE FLOW INSTABILITIES

Inlet restrictors (orifices) have been developed and demonstrated as an effective method to mitigate two-phase flow instabilities (Kennedy, Roach et al. 2000;Qu and Mudawar 2003;Wu and Cheng 2003;Wu and Cheng 2004;Chang and Pan 2007) by reshaping the Δp-G curve such that the curve is rendered positive. The Δp-G curves of the present

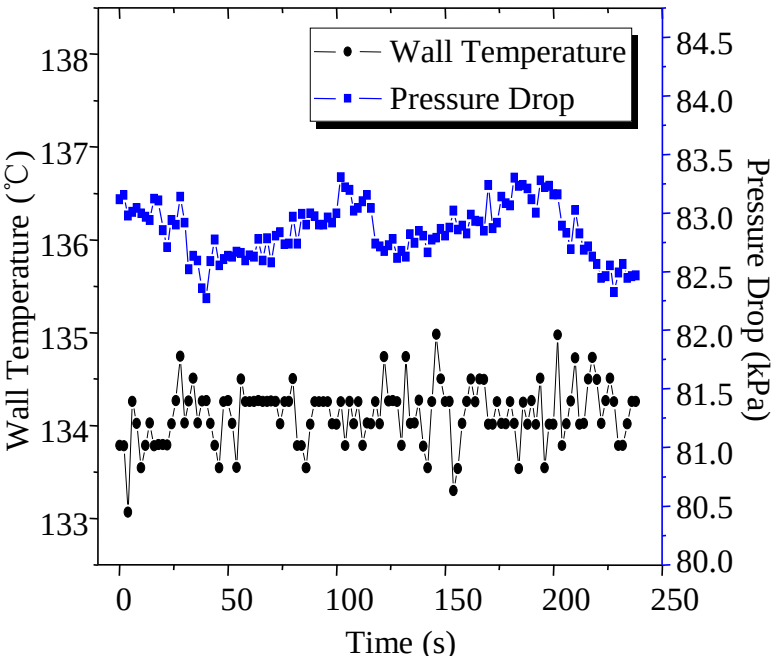

Figure 3.11. Transient wall temperatures and pressure drops in 240 seconds at a mass flux of 380 kg/m^2 s and effective heat flux of 296.6 W/cm^2 in present novel microchannel architecture.

heat exchanger at two heat fluxes, q''_{eff} = 150 and 250 W/cm^2 are compared to microchannels with *IRs* in Figure 3.10. The slopes of these two Δp-G curves from microchannels with inlet restrictors are positive, which enables high *CHF* by suppressing flow oscillations (Wang, Cheng et al. 2008), but, with a significant penalty in the form of elevated pressure drop (Kandlikar, Kuan et al. 2006;Kosar, Kuo et al. 2006;Wang, Cheng et al. 2008). It has been observed that the slopes in the current systems were greatly moderated (the slope of Δp-G curve at 150 W/cm^2 is even positive). As a result, two-phase instabilities were suppressed such that high *CHF* was demonstrated, i.e., 552 W/cm^2 at a moderate mass flux of 480 kg/ m^2 s (Figure 3.6), with a significant pressure drop reduction compared to microchannels with *IRs* obtained in previous studies. Transient pressure drops and wall temperatures at a mass flux of 380 kg/m^2 s and effective heat flux of 296.6 W/cm^2 are shown in Figure 3.11. At such high heat flux, pressure drop and wall temperature have been observed to fluctuate within 1.2% (1 kPa) and 1.5% (2 ℃), which verify the stability of the system.

3.2.5 VISUALIZATION STUDY

To obtain better fundamental knowledge of the processes governing the heat transfer enhancement discussed above, a visualization study was conducted using a high-speed imagery system (Phantom V7.3) and an Olympus microscope (BX-51). Figure 3.12 shows seven frames selected from sequential images in 8 ms at 10,000 frames per second to represent the entire bubble ebullition processes near a cross-junction where two auxiliary channels and a main-channel are connected. The interactions between vapor slugs in auxiliary channels and subcooled liquid in the entrance of the auxiliary channels are illustrated in Figure 3.13.

Figure 3.12 shows how vapor slugs filling auxiliary channels *A* and *B* triggered a bubble growth cycles (marked as time t=0). A thin liquid film between the vapor slugs and the walls was observed. The vapor slugs in the auxiliary channels only expanded toward the inlet, i.e., toward the subcooled region of the main channel, due to the restriction of the converging nozzles. The vapor slug in auxiliary channel *B* was observed to shrink due to direct condensation at 0.6 ms. The large vapor slug in the main channel was broken by the subcooled flow that was pumped through auxiliary channel *B* at 1.4 ms,

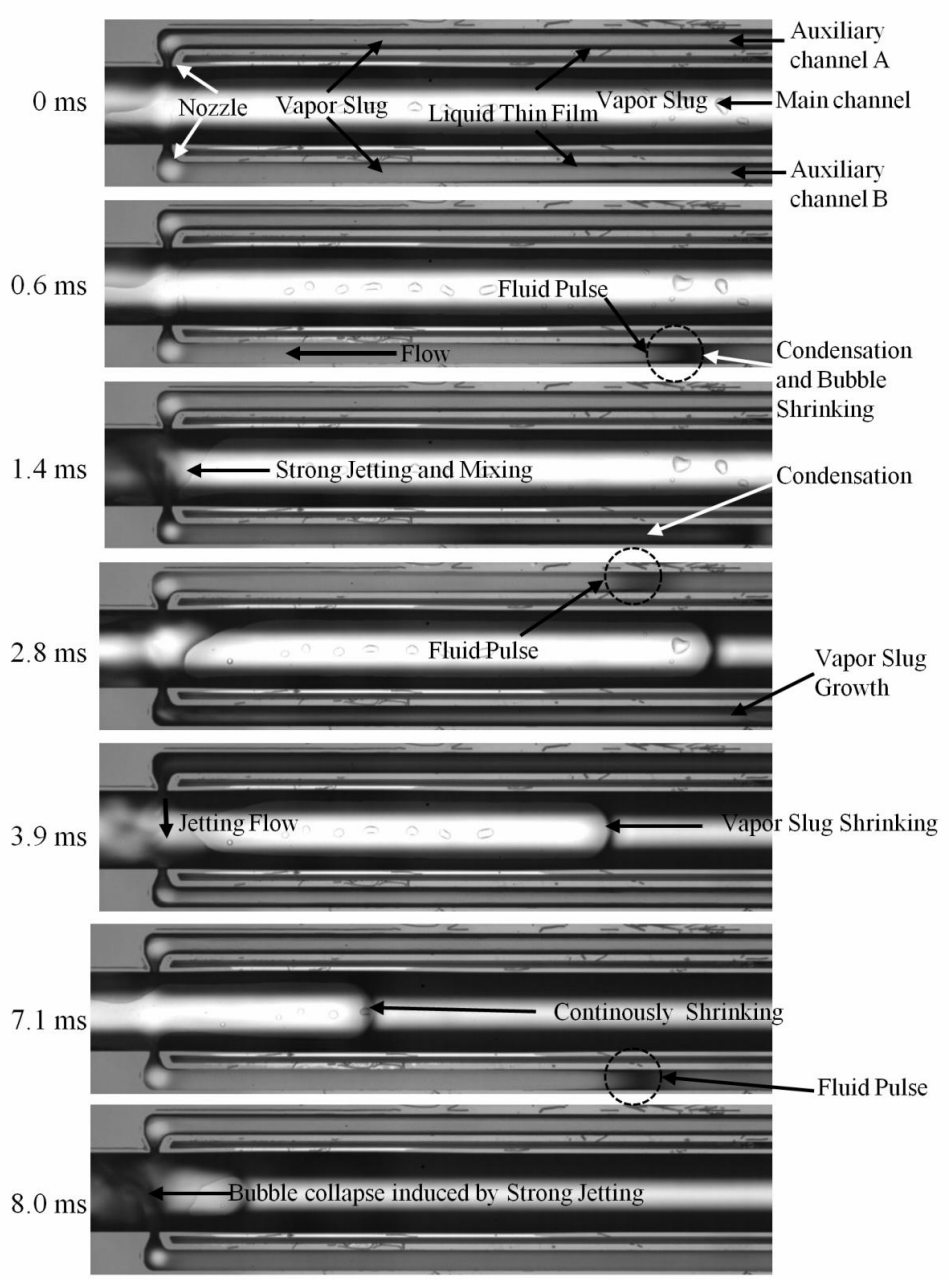

Figure 3.12. High frequency two-phase oscillations powered by bubble growth/collapse processes at a heat flux of 100 W/cm^2 in a mass flux of 400 kg/m^2 s.

which induced fluid pulses. The movement of two-phase interfaces, which could be observed and measured by high speed camera, determines the superficial velocity of fluid. The velocity of the liquid jetting was evaluated to be nearly five times higher than the

average liquid velocity from the inlet, i.e., accelerated. Alternatively, the vapor slug in auxiliary channel *A* started to shrink at 2.8 ms and completely collapsed at 3.9 ms, which led to a jetting flow via a converging nozzle and further shrinkage of the vapor slug in the main channel. This jetting flow is similar to water hammer in microchannels, however, the frequency of these pulses in the auxiliary channels and the main channel were measured to be approximately 100 and 200 Hz, respectively, at a heat flux of 100 W/cm^2 with a mass flux of 400 kg/m^2-s. The highest oscillation frequency achieved in the present microchannel architecture was over 613 Hz (Kosar, Kuo et al. 2006;Wang, Cheng et al. 2008). Such high frequency two-phase oscillations did not affect the system temperature and pressure drop. The third fluid pulse in this observation period was formed and accelerated into the cross-junction at 7.1 ms. A large vapor slug in the main channel was observed to completely collapse or had been removed at 8 ms, which significantly limits the impacts of bubble expansion rate and confinements as well as the influence of capillary force on two-phase flows in the microchannel. The walls in the microchannels can be wetted by high frequency two-phase oscillations, which, consequently, enhance heat transfer because of the thin film evaporation and convection. It should be noted that nucleate boiling heat transfer was also greatly enhanced due to induced cavitations during the collapse of large vapor slugs (Yang, Dai et al. 2012).

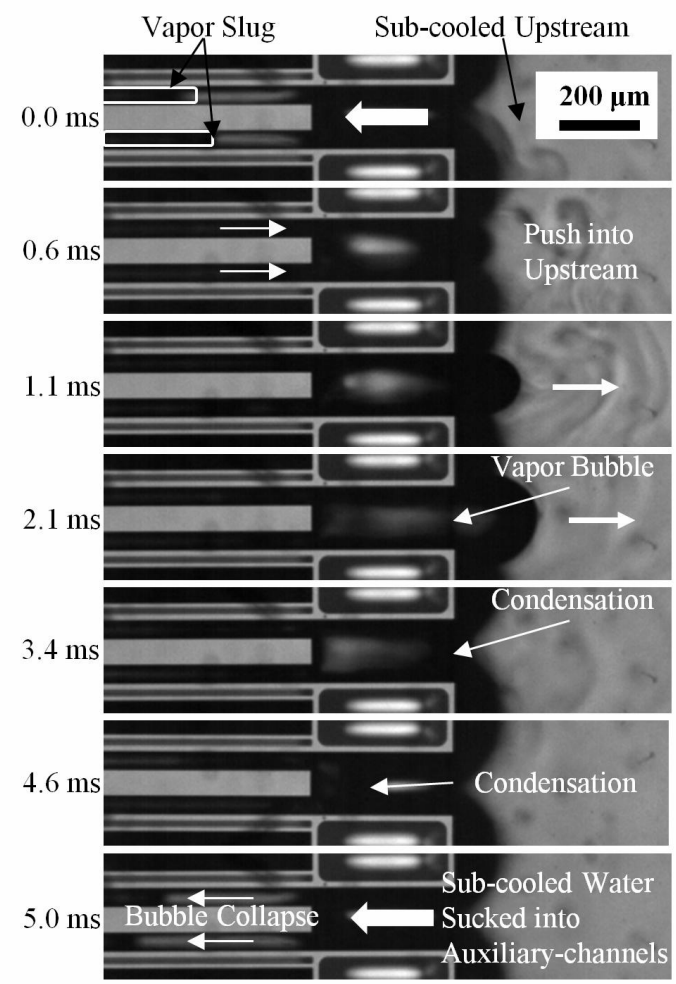

Figure 3.13. Vapor slug expansion and collapse in the entrance area.

Flow reversal driven by the rapid vapor slug expansion in the auxiliary channels was observed. The complete process of a vapor slug expansion and collapse due to direct condensation is shown in Figure 3.13. Flow reversal appeared at time 0 ms. The vapor slug expanded toward the subcooled fluid in the inlet region due to the restriction of the nozzles. The volume of vapor slug reached a maximum value at 2.1 ms when the evaporation and direct condensation heat transfer was approaching equilibrium. Disappearance of the vapor slug fronts and reassumed subcooled flow in the auxiliary

channels indicated the collapse of vapor slug and the completion of the vapor slug ebullition process.

3.3 MECHANISM

The development of high frequency two-phase oscillations (HF-TPOs) (Raven and Marmottant 2006;Fuerstman, Garstecki et al. 2007;Prakash and Gershenfeld 2007;Choi, Yu et al. 2011;Kabov, Zaitsev et al. 2011) is needed to advance ultra-efficient and compact microfluidic controllers and actuators. The volume flow rate of a thermally driven microbubble actuator, as defined by (Tsai and Lin 2002),

$$Q = 2\Delta V f \xi \tag{13}$$

where ΔV is the volume difference resulting from liquid and vapor transition, and ξ is nozzle/diffuser efficiency, can be linearly enhanced by simply increasing TPO frequency, *f*. High frequency TPOs are most commonly achieved through local microsecond heating pulses with significant sacrifice of volumetric flow rates.(Chen, Chen et al. 1997;Schasfoort, Schlautmann et al. 1999;Andersson, van der Wijngaart et al. 2001;Deng, Lee et al. 2003;Prakash and Gershenfeld 2007;Liu, Xu et al. 2010) The frequency of thermal driven TPOs is limited by slow thermal diffusivity and confinements of compressible vapor bubbles in micro-domains.(Ory, Yuan et al. 2000;Das and Wilson 2010) Most flow boiling instabilities are associated with two-phase oscillation (TPO) frequencies that range from 0.06 to 2 Hz in the laminar flow regime (e.g., parallel channel instability and upstream compressible volume instability).(Wu and Cheng 2004;Balasubramanian and Kandlikar 2005;Xu, Zhou et al. 2005;Wang, Cheng et al. 2007;Wang, Cheng et al. 2008)

The key challenge to produce and regulate HF-TPOs under a constant heat flux working condition, a normal operating mode of majority microfluidic devices, is the pronounced two-phase instabilities in microfluidic systems. The severe two-phase instabilities resulting from parallel channel instability and upstream compressible volume instability are characterized by low frequency and large magnitude TPOs.(Wu and Cheng 2004;Zhang, Tong et al. 2009) Because of the high surface tension forces induced at both ends of a confined bubble as well as the low thermal diffusivity in a microdomain, it is challenging to manage the bubble growth/expansion rate, or remove/collapse the confined bubbles rapidly(Das and Wilson 2010) in micro-domains.

In this dissertation, direct condensation was sustainably introduced and promoted to achieve high frequency collapse of confined bubbles in microchannels, which resulted in a significantly enhanced thermal bubble actuation mechanism under a constant heat flux, and hence, in generating HF-TPOs. A microfluidic unit comprised of one cross-junction, two auxiliary channels and one main channel as shown in Figure 3.14c was conceptualized and termed as a microfluidic transistor by analogizing to an electric transistor, which can passively sustain and modulate TPOs in microchannels. Fluid flows driven by pressure gradient in microfluidic systems can be fully analogous to electron transport in circuits.(Schasfoort, Schlautmann et al. 1999;Fuerstman, Garstecki et al. 2007;Prakash and Gershenfeld 2007;Rabaud 2011) Specifically, pressure drop, flow resistance, and flow rate are analogous to voltage, electrical resistance and current, respectively. In this study, fluid flows represent as either an “on” or “off” state in a bubble logic, which is switched by a confined bubble. During flow boiling in microchannels, a bubble explosively grows and expands until it is confined and shaped

by solid walls. In this situation, a confined bubble or vapor slug causes a sharp increase in the flow resistance or system pressure drop, then flows are nearly blocked by a confined bubble (or a vapor slug) and represent as an “off” state in the bubble logic.(Prakash and Gershenfeld 2007) The flows are switched to an “on” state when flow resistance is abruptly reduced due to the rapid bubble collapse enabled by direct condensation in this study.

A microfabricated test microdevice was built to experimentally demonstrate the actuation mechanism as illustrated in .. The top view of the microdevice is shown in Figure 3.14a and Figure 3.14b. Four ports (one for flow inlet, one for flow outlet and two for pressure measuring ports) were fabricated on the backside of the wafer. A 500 μm thick Pyrex glass wafer was bonded onto a 500 μm thick silicon wafer substrate as an observation window. A built-in aluminum thin film heater with size of 10 mm x 2 mm as detailed in

Figure 3.2 was integrated on the backside of a silicon chip to generate microbubbles at a constant heat flux (.d). The dimensions in length by width by depth of the main channels, auxiliary channels and restrictors are 10 mm x 200 μm x 250 μm, 5 mm x 50 μm x 250 μm and 0.4 mm x 20 μm x 250 μm, respectively. Converging nozzles with 20 μm wide opening (Figure 3.14c and Figure 3.14d) and microscale inlet restrictors

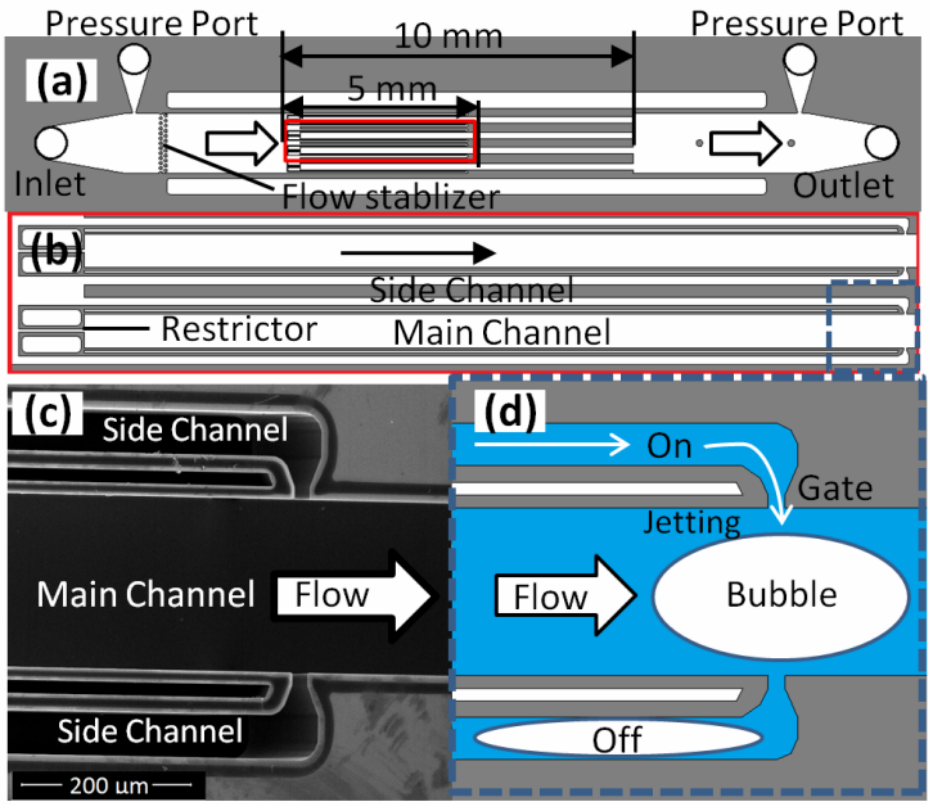

Figure 3.14. The detailed structure of a test microdevice comprised of a microchannel array with microfluidic transistors. (a) The top-view of a microfludic test chip. (b) A close-look at the side-channels and main-channels, which are connected through cross-junctions highlighted by a blue dash line. (c) A scanning Electron Microscope (SEM) image of a a microfluidic transistor. (d) The schematic mechanism of a microfluidic transistor.

(.b) were used to trap bubbles and to guide bubble expansion direction in auxiliary channels and main channels, respectively. In this study, deionized (DI) water was employed as the working fluid. Subcooled fluid (50 ℃ to 60 ℃) is supplied from inlet and is heated by a thin film heater to generate bubbles in the microchannels and exit to outlet.

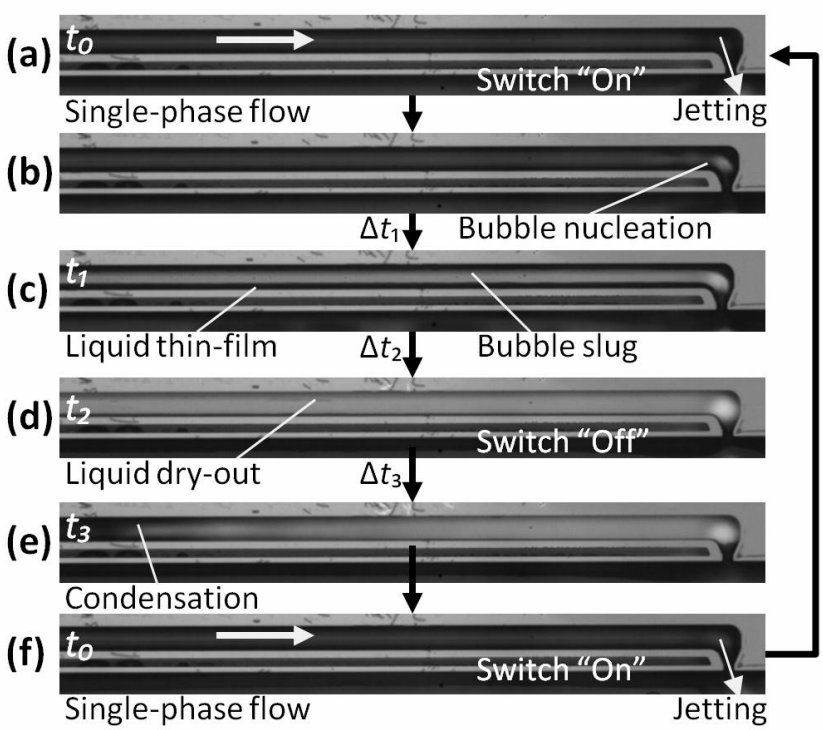

Figure 3.15. Visualization of a bubble growing/collapsing cycle in an auxiliary channel at a volumetric flow rate of 11.2 μL/s and an effective heat flux of 111.7 W cm^{-2} (for one micro fluidic transistor). White and dark areas indicate vapor and liquid phase. (a) Single phase liquid flows in the side-channel. (b) A bubble nucleates on the wall. (c) The bubble explosively grows and is confined. (d) Liquid thin film between a confined bubble and the solid wall is drying out. (e) A confined bubble rapidly collapses when its front cap directly contacts with subcooled liquid and results in a bubble shrinkage and collapse. (f) A fluid flow from the side-channel is jetted into the main-channel by the pressure gradient established from the rapid bubble collapse. Refer the detailed processes in Movie S2.

In principal, the functionality of a unit cross-junction is same as an electrical transistor during HF-BGC processes and termed as a microfluidic transistor in this work. A transistor has three terminals: "Gate", "Source" and "Drain". The carriers flow through semiconductor channel from "Source" to "Drain", which was modulated by current through "Gate". Similarly, microbubble growth (Figure 3.15b to Figure 3.15d) and

collapse (Figure 3.15e and Figure 3.15f) processes served as switches in auxiliary channels in the visualization study. As shown in Figure 3.15**,** HF-BGC processes occurred in side-channels and resulted in HF switch between "on" (Figure 3.15a and Figure 3.15f) and "off" states (Figure 3.15d). Since bubbles in side-channels were restricted by converging-nozzles, they only expanded towards inlet and contacted with subcooled liquid to induce and promote direct condensation, which led to rapid bubble collapse (Figure 3.15e) in auxiliary channels. The pressure gradient established by the rapid bubble collapse in the side-channels, in return, pumped subcooled fluid to the main channel through the "Gate" (Figure 3.15e) from inlets. Introducing subcooled fluid on the larger confined bubble pre-trapped in the main channel resulted in direct condensation, and hence, a rapid and complete bubble collapse, which abruptly reduced the flow resistance and amplified the flow rate through the main-channel (from "Source" to "Drain") as detailed in Figure 3.16.

A typical BGC process in the main-channel modulated by a microfluidic transistor was visualized (Figure 3.16). The subcooled fluid pumped from one side-channel started to attack the confined bubble in the main-channel through the "Gate" as shown in Figure 3.16 at 0 ms at a mass flux of 150 kg m^{-2} s^{-1} (volumetric flow rate at 7.5 μL/s) and heat flux of 184 W cm^{-2}. Again, a confined bubble only expands toward

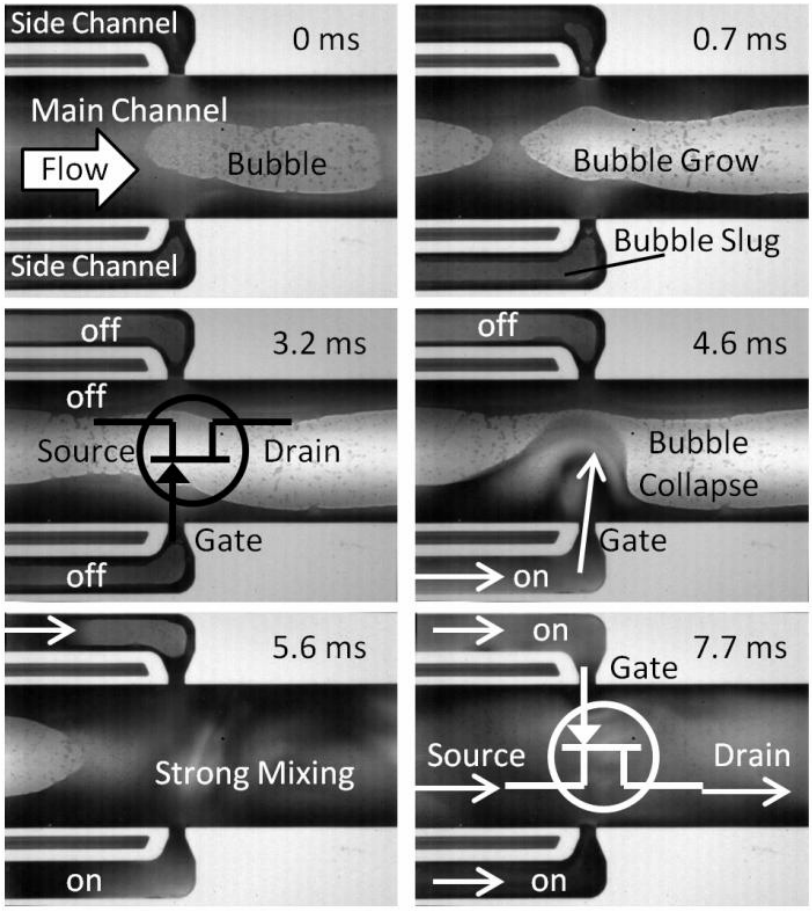

Figure 3.16. Visualization of a detailed bubble growth/collapse process modulated by a microfluidic transistor. Arrows show the flow directions. The whole process was self-sustained under a constant heat and mass flux.

downstream in the main channels because of the guidance from inlet restrictors (.b). Once the liquid in one auxiliary channel was drained out, the auxiliary channel was blocked by a confined bubble and remained in an "off" state as shown in Figure 3.16 at 3.2 ms until the bubble collapsed. Moreover, a confined bubble in the other auxiliary channel collapsed due to direct condensation and was in an "on" state at 4.6 ms as shown in Figure 3.16. The confined bubble in the main channel started to deform and shrink at 4.6 ms. Then, the additional fluid pulse induced in the side channel at 5.6 ms eventually led to a complete collapse of the confined and pre-trapped bubble in the main channel near

the “gate” area within 1 ms. Thus, the flow rate in the main-channel was amplified to reach its maximum value. The functionalities of a microfluidic transistor have been experimentally demonstrated through a whole BGC process in the main channel.

A transient flow resistance model during a TPO period in a microchannel was established in this work to capture the primary features of microbubble-switched oscillations as illustrated in Figure 3.15 and Figure 3.16. Flow resistance, *R*, is defined in this letter as pressure drop per volume flow rate (Pa S m^{-3}). Rather than focusing on understanding bubble dynamics in a component level, this modeling as shown in Eq. (1) aimed to outline the mechanism of the HF-TPOs at a system level. Since Reynolds number, Re, is less than 2300 in this study, the Hagen-Poiseuille law was employed to estimate the single-phase flow resistance, denoted as, R_{1h}, for an “on” state as shown in Figure 3.15a. Choi et al’s modified model(Choi, Yu et al. 2010) was adopted in this study to estimate the additional hydraulic resistance resulting from confined bubbles, R_{2h}. This state is a short intermediate state between “off” and “on” states as shown in Figure 3.15c. Then the thin liquid film between the confined bubble and solid wall was assumed to keep evaporating until the confined bubble eventually attaches to solid wall (i.e., drying out) as shown in Figure 3.15d. Thus the high surface tension forces induced on bubble caps result in additional flow resistance, R_{3h}, which turns “off” the channel until the confined bubbles collapse.

$$R(t)=\begin{cases} R_{1h}, t=t_0 \\ R_{1h}+R_{2h}(t),\ t_0 \le t \le t_1 \\ R_{1h}+R_{3h}(t),\ t_1 \le t \le t_2 \\ R_{1h}+R_{3h}(t_2),\ t_2 \le t < t_3 \end{cases} \tag{14}$$

$R(t)$ is a non-linear transient flow resistance during a period of BGC as plotted in Figure 3.17b and c.

According to Choi et al's modified model(Choi, Yu et al. 2010) , the hydraulic resistance of confined bubble is estimated by Eq. (15) as following

$$R_{2h}(t_1) = (0.07 + 106.8/\mathrm{Re})\rho_l v^2 / Q \tag{15}$$

where Reynolds number is defined as $\mathrm{Re} = D_h \rho_l v / \eta$, and D_h is the hydraulic diameter, ρ_l is the mass density of liquid phase, v is the superficial velocity of fluid. This empirical equation fits most cases of different Re from 50 to 700.

The flow resistance resulted from capillary pressure or surface tension force on the two ends of a bubble attaching on the walls is derived,

$$R_{3h}(t_2) = 4\gamma / (QD_h) \tag{16}$$

where γ is the surface tension. The time of bubble growing prior to directly attaching on solid walls can be calculated from several proposed models(Ory, Yuan et al. 2000;Kenning, Wen et al. 2006) as described,

$$\Delta t_1 = r_h^2 / (\alpha_l Ja^2 C_b{}^2) \tag{17}$$

where, α_l is the liquid thermal diffusivity. Jacob number is calculated as,

$$Ja = \rho_l c_l T_{sat} / \rho_v h_{fg} \tag{18}$$

and C_b is a constant with value from $\sqrt{4/\pi}$ to $\sqrt{12/\pi}$.

An additional critical time during the thin liquid film evaporation is calculated as

$$\Delta t_2 = d_{film} \rho_l h_{fg} / q \tag{19}$$

where, q is the heat flux. h_{fg} is the latent heat. The thickness of liquid film d_{film} is estimated as below

$$d_{film} = 0.67 D_h Ca^{2/3} / (1 + 3.35 Ca^{2/3}) \quad (20)$$

Above equation is called Taylor's law from fitted experimental data(Aussillous and Quere 2000). Ca is the Capillary number and estimated by $Ca = 0.445\eta / \gamma$. Finally, $\Delta t_3 = \Delta t - t_3$, which is primarily governed by the critical size of bubble collapsing and has not been well studied in a micro-domain, is estimated from the visualization study due to the complex physics. According to high speed camera videos, $\Delta t = N_f / N_{FPS}$, here N_f is the average number of frames in an oscillation period and N_{FPS} is number of Frames Per Second (FPS). A numerical fitted logistic function,

$$R(t) = R_{1h} + R_{3h}(t_2) / (1 + ae^{-bt}) \quad (21)$$

was used to estimate the transient flow resistance of microbubble-switched oscillations. The least square curve fitting method was employed to estimate coefficients *a* and *b* from regression analysis of flow resistances. This system-level lumped model was sketched in Figure 3.17a. The flow resistance from a restrictor (also refer the detailed structured in .b), R_1, which was designed to against the reverse flow in main-channels, was assumed to be a constant during the HF oscillations due to the high-aspect-ratio geometry of the restrictor.(Kosar, Kuo et al. 2006) As shown in Figure 3.17a, each switch unit was expressed by the non-linear function $R(t)$ with corresponding coefficients during HF-BGC processes. Because of the rapid bubble collapse in the main-channel, flow resistance $R_3(t)$ from "Source" to "Drain" was reduced in a short time, which can be estimated by Bernoulli's equation,

$$p_{gate} - p_{bubble} = \rho(v_j^2 - v_s^2) / 2 \quad (22)$$

where, ρ is the liquid density, v_j is the jetting fluid velocity, and v_s is bulk fluid velocity in auxiliary channels. To simplify the HF-TPO model during a typical BGC process, the time for ultrafast bubble collapse process was neglected in this study for its much shorter duration (e.g., less than 0.2 ms) compared to the total duration, approximately, 5 ms, according to visualization study. As a reference pressure, outlet pressure is assumed to be the constant environment pressure. High frequency low amplitude TPOs caused fluctuations in inlet pressure. The amplitude of pressure fluctuations was measured. Numerical simulation and experimental data of system pressure drop were compared and plotted in Figure 3.17d.

The test results were summarized and also compared with results by other researchers in Figure 3.17e. The frequency of BGC processes in the auxiliary channels were predicted at approximately 123 Hz at a heat flux of 125 W/cm^2 and mass flux of 258 kg/m^2s, which is approximately three orders higher than TPO frequency reported micro devices(Ory, Yuan et al. 2000;Das and Wilson 2010) (Figure 3.17e). An interesting phenomenon observed was that the switching motions from two auxiliary channels were alternative, which further improved the frequency of the bubble-switched oscillations in the main channel because of superimposition effects. The overall TPO frequency in the main channel was superimposed to approximately 246 Hz according to numerical simulations, which is approximately doubled and agrees well with the experimental measurement 240 Hz (Figure 3.17d). Great agreement implies that the major characteristics of the proposed HF-TPOs and microfluidic transistors were well captured.

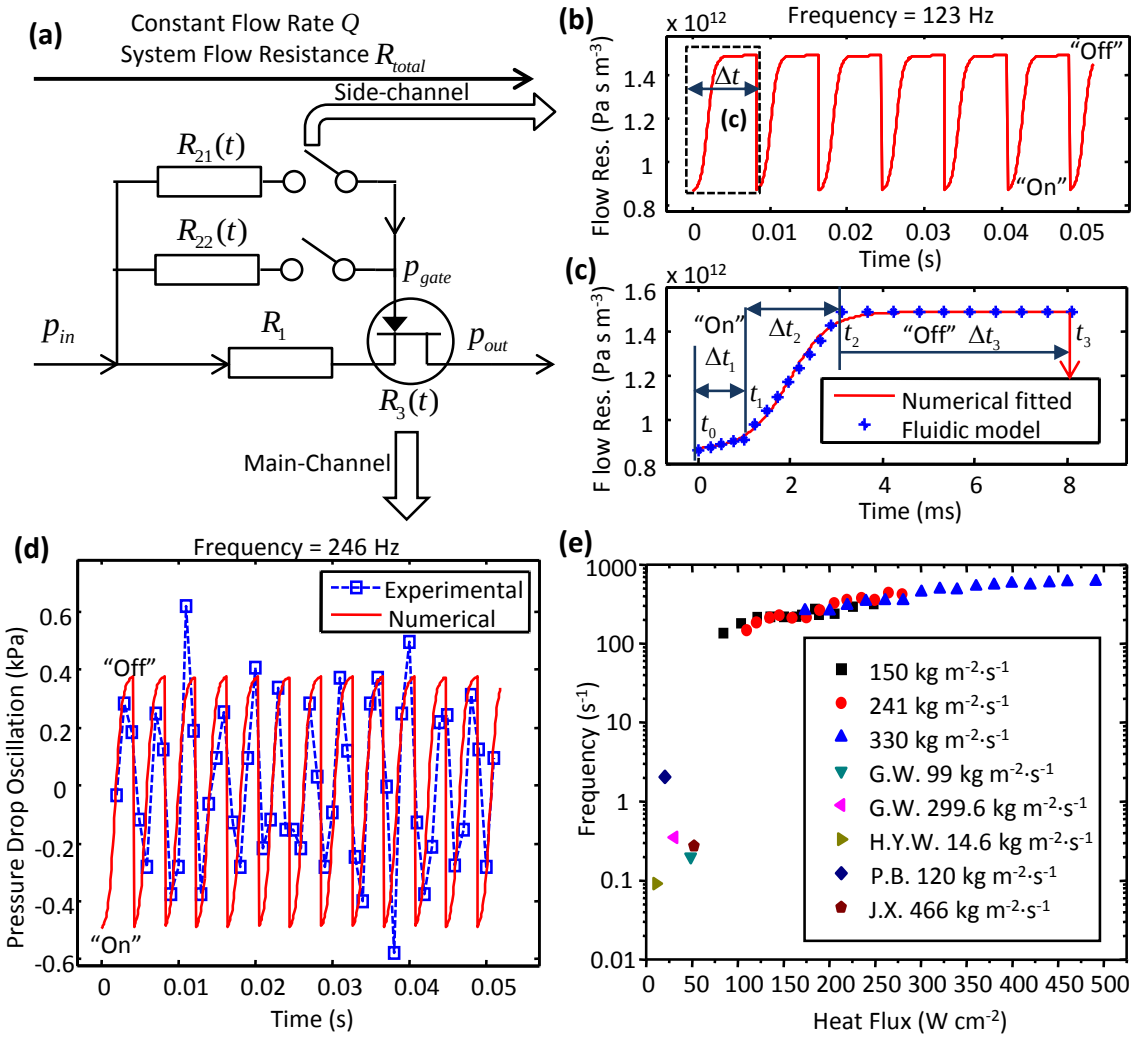

Figure 3.17. HF-TPO model and experimental measurements. (a) A lumped system model. R_{21} and R_{22} are transient flow resistances in side-channels as illustrated in (b) and (c) (the unit of R reads as "Pa s m^{-3}"). R_1 and R_3 denote flow resistance from a restrictor and the cross junction (i.e., from "source" to "drain"), respectively. (b) Periodic flow resistance in side-channels during HF-TPO processes within a period Δt. (c) Periodic flow resistances during a BGC process in side-channels were predicted by physical models and numerically fitted by a logistic function, where, $\Delta t_1 = t_1 - t_0$, $\Delta t_2 = t_2 - t_1$ and $\Delta t_3 = t_3 - t_2$ denote the bubble growing time prior to attaching on walls, the duration for liquid film evaporating and the time of a bubble sustaining and collapsing, respectively. (d) pressure drop oscillations around mean value in the main channel were measured by transducers at 1 kHz sampling rate and predicted numerically at the heat flux of 125 W/cm ²and mass flux of 258 kg/m ²s. (e) TPO Frequency measured by a high-speed camera ranges from 134 Hz to 613 Hz under various heat and mass fluxes and were compared with reported data on flow oscillations in confined micro-domains(Wu and Cheng 2004;Balasubramanian and Kandlikar 2005;Xu, Zhou et al. 2005;Wang, Cheng et al. 2007;Wang, Cheng et al. 2008).

In this dissertation, a parametric study was also conducted to assess the impacts of mass fluxes and input heat fluxes on the TPO frequency. The overlapped curves under various mass fluxes clearly indicated that the mass flux has not shown significant impacts on the TPO frequency. The TPO frequency was observed to increase with input heat flux, which suggests a strong dependence on the input heat flux. The increase of nucleate boiling and evaporation heat transfer rates with increasing heat flux is believed to be the primary reason to induce a higher bubble growing rate and hence a high TPO frequency.

Finally, a HF microbubble-switched oscillation mechanism has been conceptualized and experimentally demonstrated, which can be passively sustained and modulated by microfluidic transistors. A lumped model of HF-TPOs was developed and captured the major physical processes of HF-TPOs. Efficiency of the mass and heat transfer in microfluidic systems would be dramatically enhanced because of the strong mixing introduced by HF-TPOs in micro domains, which holds promise to further advance high heat flux thermal management technologies as well as highly efficient and compact reactors and heat exchangers. Additionally, HF-TPOs have great potential to develop high performance chip-scale bubble-driven actuators.

3.4 SUMMARY

In this study, a new microchannel architecture was developed and built to enhance flow boiling in microchannels. Experiments demonstrated that this novel architecture can considerably enhance flow boiling heat transfer rate, suppress two-phase flow stabilities, and enhance *CHF* conditions with a significant reduction in the pressure drop compared to microchannels with reentrant cavities and inlet restrictors. A visualization study was

conducted to better understand the enhancement mechanisms of the new system. The main conclusions are presented below:

High frequency bubble growth/collapse process in microchannels can be passively excited and sustained to create two-phase flow oscillations and to generate strong mixing. This in turn, is an effective method to enhance flow boiling heat transfer by promoting thin film evaporation, nucleate boiling, and advection.

The management of compressible vapor slugs in the confinements and the high frequency of vapor slugs collapse can reduce the pressure drop and achieve self-stabilized two-phase flows by reshaping the Δp-G curves during flow boiling in microchannels.

Since no extra activation method or moving parts was introduced, the present microchannel architecture can achieve compact and efficient cooling systems at low cost and with high reliabilities. Optimized configuration of the present microchannel architecture by improving the direct condensation capabilities will further improve flow boiling in microchannels.

CHAPTER 4

SINGLE AND PERIODIC ANNULAR FLOW IN MICROCHANNEL

Interest in two-phase heat and mass transfer in microfluidic systems has been rapidly growing because of its wide range of applications in diverse scientific and engineering disciplines including biology (Tadashi Okamoto 2000), chemistry (Kobayashi, Mori et al. 2004), and thermal management (R. B. Maxwell 2003;Bergles and Kandlikar 2005). Moreover, flow boiling in microchannels or microdomains is highly demanded in cooling high power microelectronics (Royne, Dey et al. 2005;Agostini, Fabbri et al. 2007;Luo and Liu 2007) and developing compact heat exchangers and chemical reactors (Jensen 2001;Kobayashi, Mori et al. 2004;Shui, Pennathur et al. 2008;Hartman and Jensen 2009).

As a result of its extensive applications, it has been extensively studied in the last decade (Thome 2004;Thome 2006;Agostini, Fabbri et al. 2007;Cheng, Wang et al. 2009). Significant progress has been made in understanding two-phase heat transfer mechanisms (Hailei and Peterson 2010;Harirchian and Garimella 2011), two-phase flow instabilities (Kandlikar, Kuan et al. 2006;Wang, Cheng et al. 2008;Zhang, Tong et al. 2009), and critical heat flux mechanisms (Wojtan, Revellin et al. 2006;Vafaei and Wen 2010;Hsieh and Lin 2012). Various techniques such as micro reentry cavities (Kosar, Kuo et al. 2005), microporous structures (Hailei and Peterson 2010), nanostructures (Singh, Sathyamurthy et al. 2010;Li, Wu et al. 2012;Morshed, Yang et al. 2012), inlet restrictors (IRs) (Kosar, Kuo et al. 2006;Wang, Cheng et al. 2008), pin fins (Krishnamurthy and Peles 2010), microjets (Guo, Wei et al. 2011), and seed bubbles

(Xu, Liu et al. 2009;Liu, Xu et al. 2010) were developed to promote flow boiling in microchannels. For example, micro cavities and micro/nanostructures can improve nucleate boiling by increasing active nucleation site density. Microjets were used to promote convections/advections by disturbing flows in microchannels. However, these reported techniques have various drawbacks such as reduced reliability induced by complex structures (Xu, Liu et al. 2009;Liu, Xu et al. 2010;Guo, Wei et al. 2011) and low HTC on IRs and finned boiling surfaces (Kandlikar 2002;Kosar, Kuo et al. 2006;Wang, Cheng et al. 2008;Cheng, Wang et al. 2009;Krishnamurthy and Peles 2010). Moreover, the flow boiling stabilities often result in premature critical heat flux (CHF) conditions and hence low CHF (Bergles and Kandlikar 2005). And, the pressure drop of a two-phase flow is significantly higher than that of a single phase flow for a given mass flux because of the reduced average fluid density (Cheng, Wu et al. 2007).

Many techniques such as inlet restrictors (IRs) (Kosar, Kuo et al. 2006;Schneider, Kosar et al. 2006;Lee, Liu et al. 2010), seed bubbles (Guohua and et al. 2009;Xu, Liu et al. 2009;Guohua, Jinliang et al. 2010), and diverging cross-section channels (Po Chang and Chin 2008;Chun Ting and Chin 2009;Lin, Fu et al. 2011;Fu, Tsou et al. 2012) were developed to manage flow boiling instabilities and hence to enhance CHF. The most effective configuration before this study is the inlet restrictors (IRs) or orifices (Kosar, Kuo et al. 2006;Wang, Cheng et al. 2008;Mukherjee and Kandlikar 2009). Neverthesless, IRs usually led to a dramatic escalation of pressure drops (Kandlikar, Kuan et al. 2006;Kosar, Kuo et al. 2006;Wang, Cheng et al. 2008) as shown Figure 4.14. Thus, current solutions have to face these dilemmas.

To radically solve these problems, two-phase flow regimes shall be considered. Two-phase flow regime transitions in conventional microchannels (Thome 2004;Raven and Marmottant 2006;Harirchian and Garimella 2011) are challenging to predict, often transport processes at the micro scale are not designed properly, which in turn, hinders performance and can cause severe two-phase flow boiling instabilities(Thome 2004;Bergles and Kandlikar 2005;Raven and Marmottant 2006;Wang, Cheng et al. 2008;Kashid, Renken et al. 2011;Liu, Li et al. 2011). Although, previous studies applied nanostructured surfaces inside microchannels to suppress flow boiling instabilities, (Khanikar, Mudawar et al. 2009;Liu, Li et al. 2011;Kousalya, Hunter et al. 2012;Li, Wu et al. 2012;Morshed, Yang et al. 2012) the flow regimes in these studies were not exclusively annular flow and hence the significant enhancement of critical heat flux (CHF) was not reported. Furthermore, none of these techniques aimed to enhance flow boiling in microchannels through manipulating or even controlling two-phase flow structures, i.e., regimes or patterns. The methodology or technique aiming to enhance CHF and manage pressure drop of flow boiling in microchannels by directly manipulating two-phase flow regimes or fluid structures has not been reported (Kuo and Peles 2008;Hailei and Peterson 2010;Vafaei and Wen 2010).

During flow boiling in microchannels, boiling surfaces play critical roles in governing bubble nucleation, growth, separations, interactions, and two-phase flow regimes. Microchannels are usually microfabricated on Si substrates by wet-etching or deep reactive ion etching (DRIE) (Losey, Jackman et al. 2002;Kobayashi, Mori et al. 2004;Luo and Liu 2007;Kuo and Peles 2008). The peak-to-peak roughness of etched Si wafers can be as low as 3 nm at bottom wall (Chandrasekaran and Sundararajan 2004)

and less than 300 nm at scalloped sidewalls (Kuo, Kosar et al. 2006), which are not favored by nucleate boiling due to the lack of optimized nucleation sites and, hence, result in explosive boiling and low heat transfer rate because of the high onset of nucleate boiling (ONB) (Li, Peterson et al. 2008). Various artificial nucleation cavities were developed to enhance nucleate boiling (H. Kubo 1999;Hailei and Peterson 2010;Cao, Xu et al. 2011). Recently, one dimensional (1D) nanosturctures such as nanowires (Li, Wang et al. 2008;Chen, Lu et al. 2009) and carbon nanotubes (CNTs) (Ujereh, Fisher et al. 2007;Khanikar, Mudawar et al. 2009) were used to enhance nucleate boiling during pool boiling and convective boiling in microchannels (Khanikar, Mudawar et al. 2009;Singh, Sathyamurthy et al. 2010;Liu, Li et al. 2011;Kousalya, Hunter et al. 2012;Li, Wu et al. 2012;Morshed, Yang et al. 2012). Enhanced HTC and CHF were reported because of the higher nucleation site density and enhanced wettability. However, it has not been demonstrated that the boiling surfaces could play critical roles of governing the bubble size, manipulating the dominant surface tension force and hence eventually determining two-phase flow patterns/regimes and then heat transfer modes. To date, flow boiling in microchannels is still dominated by bubble confinements (Kandlikar 2010;Rashid, Bjorn et al. 2010), laminar and capillary flows, which result in unpredictable flow pattern transitions (Serizawa, Feng et al. 2002;Harirchian and Garimella 2011) and tend to induce severe flow boiling instabilities and suppress evaporation and convection. This, in turn, is detrimental to heat transfer.

A novel boiling surfaces with optimal submicron pores (formed by nanowire bundles) surrounded by nanoscale pores (created by individual nanowires) were developed (Yang, Dai et al. 2013). Applying these nanowired surfaces on all inner walls

of microchannels, the transitional flow boiling regimes in microchannels can be reduced to a single annular flow from ONB to the critical heat flux (CHF) condition by controlling the flow structures in two aspects: reducing bubble size and transforming the direction of surface tension force from the cross-sectional plane to the inner-wall plane (Yang, Dai et al. 2013).

However, the nanowired surface will induce a question. Will the high roughness increase the flow resistance? Existing studies indicate that roughness (Cavallini, Del Col et al. 2009;Hailei and Peterson 2010;Dai, Yang et al. 2013) and wettability (Rapolu and Son 2011;Trieu Phan, Caney et al. 2011;Ahn, Kang et al. 2012) of the wall surfaces play important roles in determining the thermal-hydraulic characteristics of two-phase flow. It was demonstrated that the pressure drop in microchannels may be determined by capillary forces, which could be reduced by increasing surface wettability (Rapolu and Son 2011;Trieu Phan, Caney et al. 2011). Thin liquid films were assumed to be formed between vapor slugs and walls (Cavallini, Del Col et al. 2009;Rapolu and Son 2011). However, the vapor quality was low, i.e., $\chi < 0.08$, with low flow rates and superficial vapor velocities. Additionally, CHF could be enhanced using high-roughness microscale wicking structures in microchannel (Hailei and Peterson 2010;Ahn, Kang et al. 2012;Dai, Yang et al. 2013). The capillarity resulting from super-hydrophilic wicking structures was believed to be the primary reason. However, higher wall roughness can also induce higher pressure drop (Cavallini, Del Col et al. 2009). From this brief literature review, a study that aims to reduce pressure drop of flow boiling by manipulating flow patterns is still lacking.

.In this dissertation, enhanced flow boiling heat transfer in the single and periodic annular flow regime was experimentally studied and systematically characterized. The mechanisms of enhanced heat transfer were analyzed and then discussed. And the hydraulic characteristics of the single and periodic annular flow were studied. As compared to microchannels with smooth walls, the pressure drop was substantially reduced and CHF was greatly enhanced without applying IRs. When compared to microchannels with IRs, CHF was slightly reduced at high mass fluxes. Visualization and theoretical studies showed that the new fluid structure, i.e., the ideal separation of vapor and liquid flows, plays critical roles in reducing pressure drops. The greatly enhanced global liquid supply, which was enabled by rapid wetting and local liquid spreading by capillary flow induced by superhydrophilic SiNWs, was behind the dramatically enhanced CHF. In this study, the exit vapor quality achieved 0.52 and Reynolds number based on the exit vapor flow was less than 2200.

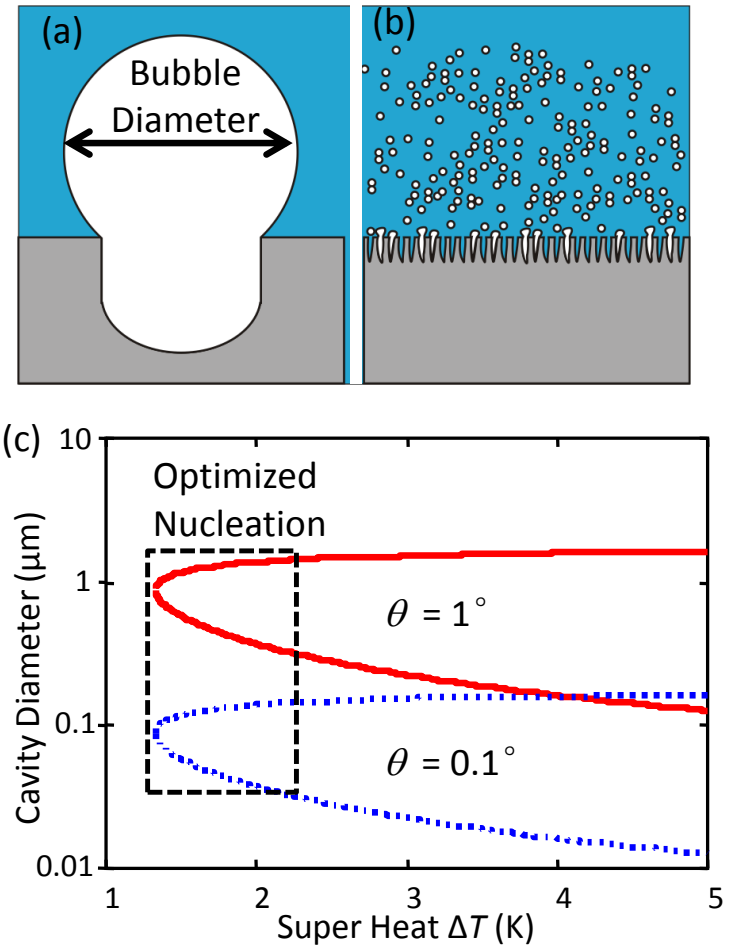

Figure 4.1. Design of nano-engineered boiling surfaces. (a) Bubble size in plain-wall microchannels. (b) Bubble size in SiNWed microchannels. (c) Optimal range of cavity diameters that can be formed by superhydrophilic SiNWs.

Compared with submicron cavities (Figure 4.1a) (Kuo, Kosar et al. 2006), the nucleation site density can be dramatically enhanced on the bi-porous cavities formed on the nanostructured boiling surfaces (Li, Wang et al. 2008;Yang, Dai et al. 2013) because the microscale cavities can be activated by vapor molecules generated in nanoscale cavities during the whole boiling process (Figure 4.1b) (Li, Wang et al. 2008). In this study, the nucleation cavity size was optimized to enhance HTC by minimizing the

superheat, ΔT, i.e, the temperature difference between wall and saturation temperature. As shown in Figure 4.1c, the range of active cavity opening diameter, D_c, was estimated from Eq. 14 (Hsu 1962).

$$D_{c\max,\min} = \frac{\delta_t \sin\theta}{2(1+\cos\theta)} \cdot \left(\frac{\Delta T}{\Delta T + \Delta T_{sub}} \right) \cdot \left[1 \pm \sqrt{1 - \frac{8\sigma_f (\Delta T + \Delta T_{sub}) T_{sat} (1+\cos\theta)}{\rho_v h_{fg} \delta_t \Delta T^2}} \right] \tag{23}$$

where h_{fg}, ΔT_{sub}, θ, σ_f, ρ_v, and δ_τ denote latent heat, subcooling degree, contact angle, surface tension, vapor density, and boundary layer thickness, respectively. The optimal range of nucleation cavity size on superhydrophilic surface was estimated between 100 and 2000 nm when the apparent contact angles were assumed between 0.1˚ and 1˚.

Guided by the classic nucleate boiling theory (Hsu 1962) and previous work (Li, Wang et al. 2008), boiling surfaces with micropores (formed from nanowire bundles) surrounded by nanoscale gaps (created by individual nanowires) as shown in Figure 4.2c were created by Si nanowires (SiNWs) using the nanocarpet effect (Fan, Dyer et al. 2004). The SiNWs and their coverage in microchannels were illustrated in Figure 4.2. The scanning electron microscopy (SEM) images were taken with a tilt angle as shown in Figure 4.2a. These images clearly show that inner walls, including the side walls (Figure 4.2b) and bottom wall in a microchannel (Figure 4.2c and Figure 4.2d), were nearly uniformly coated by SiNWs (approximately 20 nm in diameter and 5 μm long). The top surfaces of the microchannel array were covered by Pyrex glass as visualization windows (Figure 4.3i). The SiNWs were oxidized to achieve superhydrophilicity (approximately 0˚ apparent contact angle) using the Wenzel effect (Kuo and Gau 2010). This type of boiling surfaces intrinsically comprised of interconnected microscale and nanoscale cavities created by hydrophilic SiNWs and were used to improve nucleate boiling (Li, Wang et al.

2008;Li, Furberg et al. 2008;Chen, Lu et al. 2009) and induce capillary flow and hence, thin film evaporation in this experimental study.

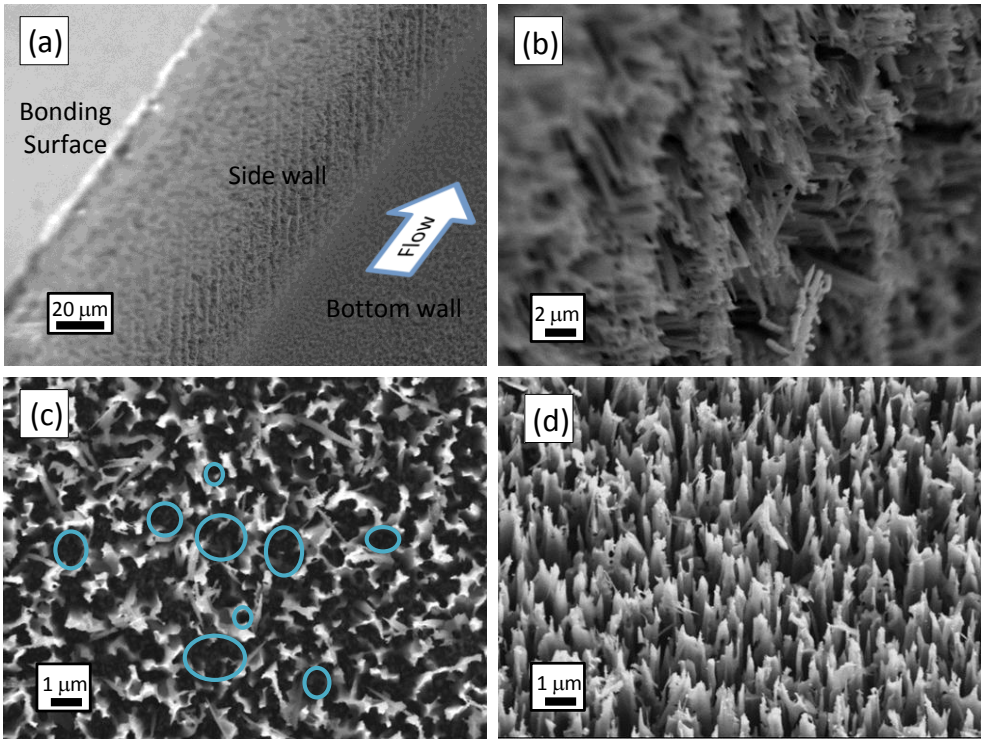

Figure 4.2. Scanning Electron Microscope (SEM) images of SiNW boiling surfaces. (a) Tilted view of SiNWs in vertical and bottom walls in microchannels. (b) Tilted view of SiNWs on a vertical wall. (c) Top view of SiNWs on a bottom wall. Typical microscale pores were highlighted. (d) Tilted view of SiNWs on the bottom wall.

4.2 EXPERIMENTAL PROCEDURES

In this section, the structures of micro devices and testing systems are introduced. Moreover, the data reduction procedures are stated.

4.2.1 DESIGN OF MICRO DEVICES

As shown in Figure 4.3a, a micro device consists of five parallel straight microchannels (width, depth, length: 200 μm x 250 μm x 10 mm). A flow stabilizer was placed in front of the inlets. Two pressure measuring ports were located at inlet and outlet to measure pressure drops. Thermal isolation air gaps were created to reduce heat loss during flow boiling tests. The thin-film heater was integrated on the backside to supply heat and to measure average temperature as a thermistor. Additionally, as shown in Figure 4.3b, three thermistors (i.e., thermistors 1 to 3) were integrated underneath the microchannel array to measure the local temperatures. Specifically, the thermistor #1, 2 and 3 were located near the inlet, the one third length of the channel and the 2/3 length of the channel from the inlet.

In this experimental study, as shown in Figure 4.3c, flow boiling in three types of microchannel configurations was studied and compared. The objective is to achieve better understanding of the mechanisms of enhanced flow boiling heat transfer in the single and periodic annular flow through comprehensive comparisons with two baseline configurations: plain-wall microchannels with and without IRs. All three configurations have nearly identical channel dimensions (width, depth, length: 200 μm x 250 μm x 10 mm). To reflect the HTC enhancement resulted from high nucleation site density and the

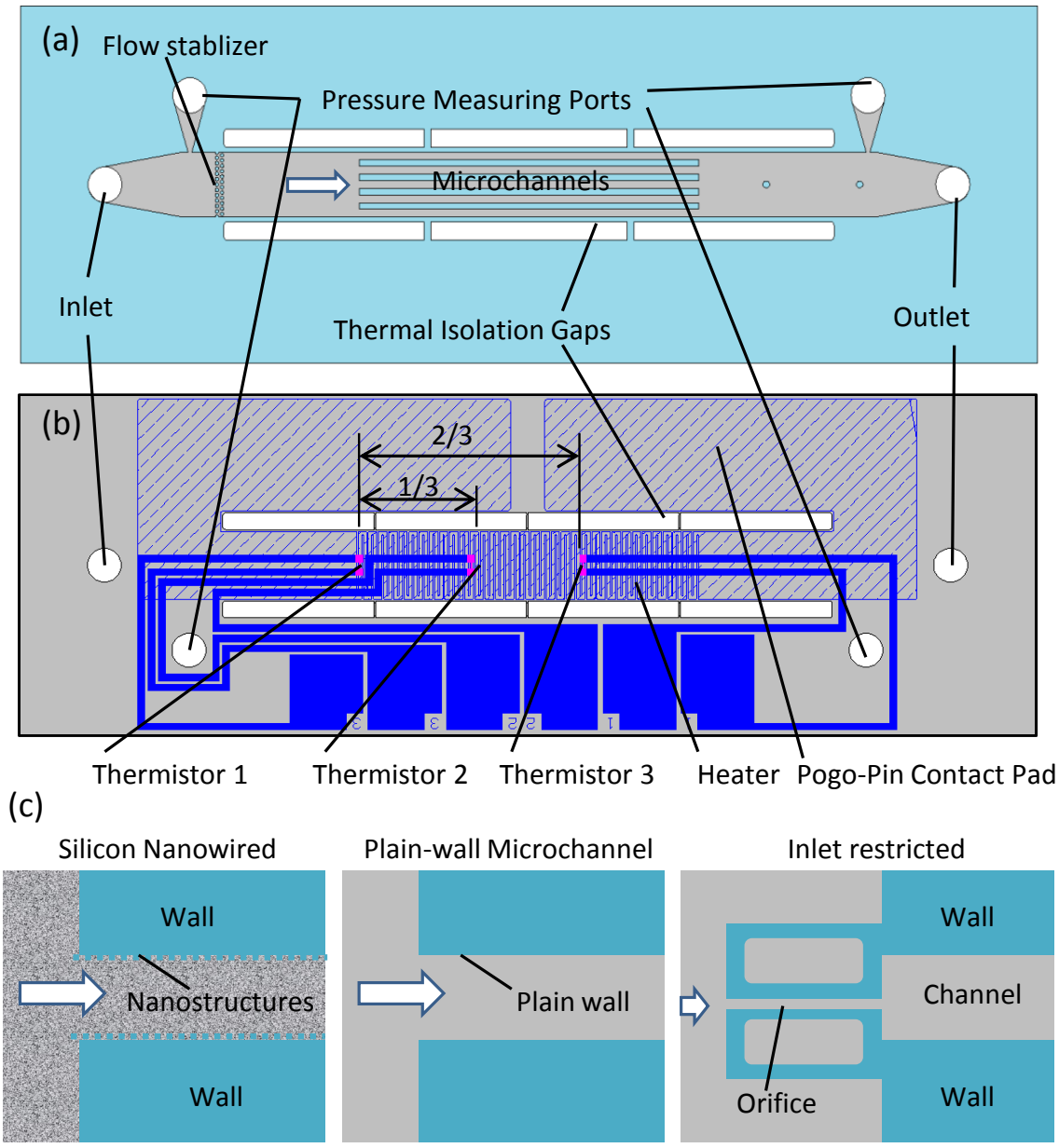

Figure 4.3. The configurations of micro devices for flow boiling experiments. (a) The front side of a micro device. (b) The back side of a micro device. (c) Three types of microchannel configurations were studied and compared in this study. single and periodic annular flow in SiNWed microchannels(Yang, Dai et al. 2013), flow boiling in plain-wall microchannels (Kuo and Peles 2008) was compared. Moreover, plain-wall channels with IRs (width, depth, length: 20 μm x 250 μm x 400 μm) were further compared to demonstrate the enhancement induced by rewetting flows and enhanced thin-film evaporation in the new flow boiling regime (Yang, Dai et al. 2013).

4.2.2 MICRO DEVICE FABRICATIONS AND SINWS INTEGRATION

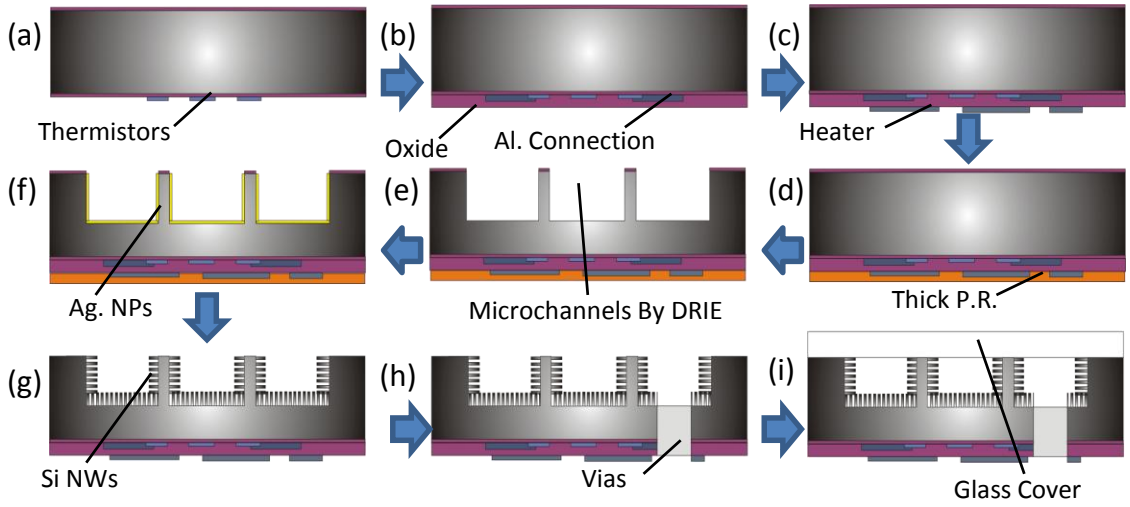

Figure 4.4. Major micro/nanofabrication steps. Gray, blue, purple, orange and white areas represent silicon, metal, silicon oxide, photoresist and glass, respectively.

The microchannel heat exchangers were made from a silicon wafer bonded to a Pyrex wafer by micro/nanofabrication processes (Figure 4.4) (Yang, Dai et al. 2013). Thin-film heaters and thermisters on the backside were integrated on the micro devices for flow boiling tests in order to improve the measurement accuracy. The fabrication processes started with a 100-mm-diameter <100> heavily doped P-type silicon wafer. The wafer thickness is ~500 μm. 500 nm dense oxide layers were induced onto both sides of silicon wafer as an isolation layer by thermal oxidation (Figure 4.4a). 10-nm-thickness titanium and 200-nm-thickness aluminum were deposited by DC sputtering and patterned as thermistors and metal connection pads, respectively (Figure 4.4a and Figure 4.4b). Then, thin-film heaters were patterned by wet-etching (Figure 4.4c). Aluminum metal connections for electrical power were also patterned by wet-etching as shown in Figure 4.4c. After that, a 500-nm silicon oxide layer and a thick photoresist layer (SPR 220-7.0) were deposited and spin-coated to protect backside devices (Figure 4.4d). On the front

side of wafer, five parallel microchannels (width, depth, length: 200 μm x 250 μm x 10 mm) were etched by DRIE (Figure 4.4e).

Various techniques were developed to create nanostructured boiling interfaces such as sputtering (Li, Wang et al. 2008), electrochemical etching (Chen, Lu et al. 2009) and electrochemical deposition (Li, Furberg et al. 2008;Chen, Lu et al. 2009;Morshed, Yang et al. 2012), however, functional nanostructures on the vertical walls were not reported. In this study, an electroless electrochemical etching technique was employed and improved to directly grow Si nanowires on the vertical and bottom walls in microchannels using silver nanoparticles (AgNPs) as catalysts (Peng, Yan et al. 2002;Zhang, Peng et al. 2008). Although AgNPs were only used to create two-dimensional (2D) arrays of nanowires previously (Fan, Dyer et al. 2004;Chen, Lu et al. 2009;Li, Wu et al. 2012), it was the first time to experimentally demonstrated that AgNPs can be coated on high aspect ratio structures such as microchannel arrays to create SiNWs on all inner walls. In this study, 4.5 M hydrofluoric acid and 0.005 M silver nitrite solution were prepared for the deposition of catalysts. The wafer was then carefully placed into the solution to coat a layer of AgNPs thin film on inner walls by slowly stirring in the solution (Figure 4.3f). The AgNPs were attached on smooth surfaces of microchannels as etching catalysts while the rest areas were protected as bonding interfaces by covering oxide or nitride from etching. The finished wafer was rinsed in DI water to remove the residual Ag+ and etched in 4.8 M hydrofluoric acid and 0.15 M hydrogen peroxide solution. The etching time was about 15 minutes to achieve 5 micrometer long SiNWs as shown in Figure 4.4g. These SiNWs were naturally oxidized to achieve super-hydrophilicity (approximately 0˚ apparent contact angle) using the

Wenzel effect (Chen, Lu et al. 2009;Liu, Li et al. 2011). To reduce the vapor bubble departure diameter and enhance nucleate boiling, the height of Si nanowires was designed and carefully controlled during the etching process to form bi-porous boiling surfaces with optimized openings using the nanocarpet effect (Fan, Dyer et al. 2004). In preparation of SiNWs, morphology of SiNWs can be controlled by varying of AgNPs deposition density and the etching time. Denser AgNPs layer and longer etching duration would create higher porosities and hence, larger cavities.

After integrating SiNWs, four thorough vias were fabricated by DRIE to create two pressure ports, one liquid inlet, and one outlet as detailed in Figure 4.4h. As shown in Figure 4.4i, a Pyrex glass wafer was anodically bonded onto the silicon substrate to seal the microchannels and also serve as windows for optical visualization. The individual microchannel test chips (length, width, thickness: 30 mm x 10 mm x 1 mm) were cut from the wafer by a dice-saw.

4.2.3MEASUREMENTS AND DATA REDUCTION

Deionized (DI) water was employed as the working fluid. The flow boiling testing system was built and calibrated in previous work (Yang, Dai et al. 2013). The pressures in the inlet and outlet were measured by two pressure transducers and used to estimate pressure drops in transient and steady states. The flow rate was measured by a Sensiron ASL1600 flowmeter with 0.03 kg m^{-2} s^{-1} resolution. The average temperature of heater was measured by the thin film aluminum heater. All measurements were carried out at 1 atm and room temperatures (~22℃). All experimental data were collected by an Agilent data acquisition system. The temperature on the heater, *T*, was calculated as a linear function of its resistance, *R*, with a correlation coefficient larger than 0.9999.

$$T = K(R - R_{ambient}) + T_{ambient} \tag{24}$$

$T_{ambient}$ and $R_{ambient}$ are the temperature and resistance in the ambient environment. The slope, *K*, was pre-calibrated (Fanghao Yang, Xianming Dai et al. 2012). The heat loss, $\dot{Q}_{loss}$, between the micro heat exchanger and the ambient was evaluated as a function of the corresponding temperature difference. Additionally, the sensible heat from subcooled fluid, $\dot{Q}_{subcooled} = \dot{m}C_p\Delta T_{sub}$, was excluded. The electrical power, *P*, was calculated from the product of voltage and current, $P = V \times I$. The effective power, which participates in phase change, is

$$P_{eff} = P - \dot{Q}_{loss} - \dot{Q}_{subcooled} \tag{25}$$

Then, exit vapor quality of two-phase flow was estimated as

$$\chi_e = P_{eff} / (h_{fg}\dot{m}A_c) \tag{26}$$

The effective heat flux based on the heating area, q''_{eff}, was estimated as $q''_{eff} = P_{eff} / A_{eff}$. The wall temperature was calculated from

$$T_{wall} = T - q''_{eff}t_w / k_s A_{eff} \tag{27}$$

where, t_w, is the thickness of wall, k_s, is the thermal conductivity of silicon and the effective heating area, A_e, is 20 mm^2 (2 mm x 10 mm). Considering the fin effect, the two-phase heat transfer coefficient, h_{tp}, based on wall areas is given by

$$h_{tp} = \frac{q''_{eff}W_{unit}}{(T_{wall} - T_{sat})(W + 2\eta H)} \tag{28}$$

where, W_{unit}, W, and H are the unit width, the channel width and the channel height, respectively (Table 1). The fin efficiency, η, was calculated as

$$\eta = \frac{\tanh(mH)}{mH} \tag{29}$$

The fin parameter, *m*, is given by

$$m = \sqrt{\frac{2h_{tp}}{k_s W_w}} \tag{30}$$

The converged heat transfer coefficients can be solved by iterations.

The dimension of microchannels was detailed in Part I. In this study, experimental frictional pressure drop, $\Delta p_{f,\exp}$, is derived by subtracting accelerational pressure drop, Δp_{acc}, pressure drop of the flow distributor, $\Delta p_{distributor}$, pressure drop of plenum chambers, Δp_{plenum}, pressure drop of the inlet effect, Δp_i, and outlet effect, Δp_o, from the total pressure drop, Δp_{total}, which was measured by two pressure transducers at pressure-drop measuring ports. The frictional pressure drop can be reduced as,

$$\Delta p_{f,\exp} = \Delta p_{total} - \Delta p_{acc} - \Delta p_i - \Delta p_o - \Delta p_{plenum} - \Delta p_{distributor} \tag{31}$$

The accelerational pressure drop is given by

$$\Delta p_{acc} = G^2 \left(\frac{1}{\rho_i} - \frac{1}{\rho_{2\phi,o}} \right) \tag{32}$$

where, mass flux is $G = \dot{m} / A_c$; ρ_l and ρ_v denote the densities of liquid and vapor, respectively. The density of inlet flow, ρ_i, is assumed to be the density of liquid flow, ρ_l. The density of outlet two-phase flow, $\rho_{2\phi,o}$, is two-phase and estimated by

$$\rho_{2\phi,o} = \alpha\rho_v + (1-\alpha)\rho_l \tag{33}$$

where, α, is the void faction.

The pressure drop of inlet effects was estimated from the model developed in (Abdelall, Hahn et al. 2005)

$$\Delta p_i = \rho_l \frac{\bar{u}_{l,i}^{\ 2}}{2} \frac{1-\beta\tau^2 C_C^2 - 2C_C + 2C_C K_d}{C_C} \tag{34}$$

The model to estimate pressure drop of outlet effects was adopted from (Abdelall, Hahn et al. 2005):

$$\Delta p_o = \rho_v \frac{\bar{u}_{v,o}}{2} \left[\frac{1-2K_d\tau + \tau^2(K_d - 1)}{2} - (1-\tau^2) \right] \tag{35}$$

where, the parameter, C_C, was proposed by Geiger (Geiger 1964),

$$C_C = 1 - \frac{1-\tau}{2.08(1-\tau) + 0.5371} \tag{36}$$

From Eq. 8 to 9, $\bar{u}_{l,i}$ and $\bar{u}_{v,o}$ represent the average liquid velocities at inlet and outlet, respectively, were estimated as

$$\bar{u}_{l,i} = \dot{m} / (A_l \rho_l) \tag{37}$$

and

$$\bar{u}_{v,o} = \dot{m}\chi_e / (A_v \rho_v) \tag{38}$$

The momentum correction factor, $K_d = 1.33$, was used for laminar flow. τ is the flow area contraction ratio.

The pressure drop of plenum chambers was broken into two parts:

$$\Delta p_{plenum} = \Delta p_{i,plenum} + \Delta p_{o,plenum} \tag{39}$$

where, the pressure drop of inlet plenum was estimated by

$$\Delta p_{i,plenum} = f_{plenum} \rho_l \frac{L_{i,plenum}}{D_{i,plenum}} \frac{\bar{u}_{plenum}^2}{2} \tag{40}$$

and the pressure drop of outlet plenum was estimated by

$$\Delta p_{o,plenum} = f_{plenum}\rho_v \frac{L_{o,plenum}}{D_{o,plenum}} \frac{\bar{u}^2_{plenum}}{2} \tag{41}$$

, where, L_{plenum}, is the length of plenums; and D_{plenum}, is the hydraulic diameter of plenums. The friction factor was calculated as

$$f_{plenum} = \frac{C_f}{\mathrm{Re}_{plenum}} \tag{42}$$

where, C_f, was adopted from (Shah and London 1978).

The pressure drop of flow distributors was given by

$$\Delta p_{distributor} = N f_{cross}\rho_l \left(\frac{S_T}{S_T - D_{pin}} \right)^2 \frac{\bar{u}^2_{plenum}}{2} \tag{43}$$

where, *N*, is the number of pin fins in a single row of flow distributers and the f_{cross}, as estimated by Gunther and Shaw (Gunther and Shaw 1945); S_T, is the transverse pitch; and D_{pin}, is the hydraulic diameter of pin fins.

The uncertainties of measured values were derived by the uncertainty theory. According to the datasheet of instruments in the test system, the measurement uncertainties were estimated and listed in Table 1. The uncertainties of derived parameters were calculated by applying the method in Kline and McClintock's article (Kline and McClintock 1953).

Table 4.1. Microchannel Dimensions

W_w (μm)	W (μm)	H (μm)	t_w (μm)	t (μm)
180	220	250	250	500

4.3 RESULTS AND DISCUSSION

4.3.1 SINGLE AND PERIODIC ANNULAR FLOW BOILING REGIME

The behaviors of flow boiling in microchannels would be fundamentally altered when bubble size was reduced down to nanometer or submicrometer (< 5 μm) as schematically shown in Figure 4.1b (Borkent, Dammer et al. 2007;Jin, Gong et al. 2008). As a result, a single and periodic annular flow as illustrated in Figure 4.5 was formatted by superhydrophilic SiNWs grown on all inner walls in microchannels (Yang, Dai et al. 2013).

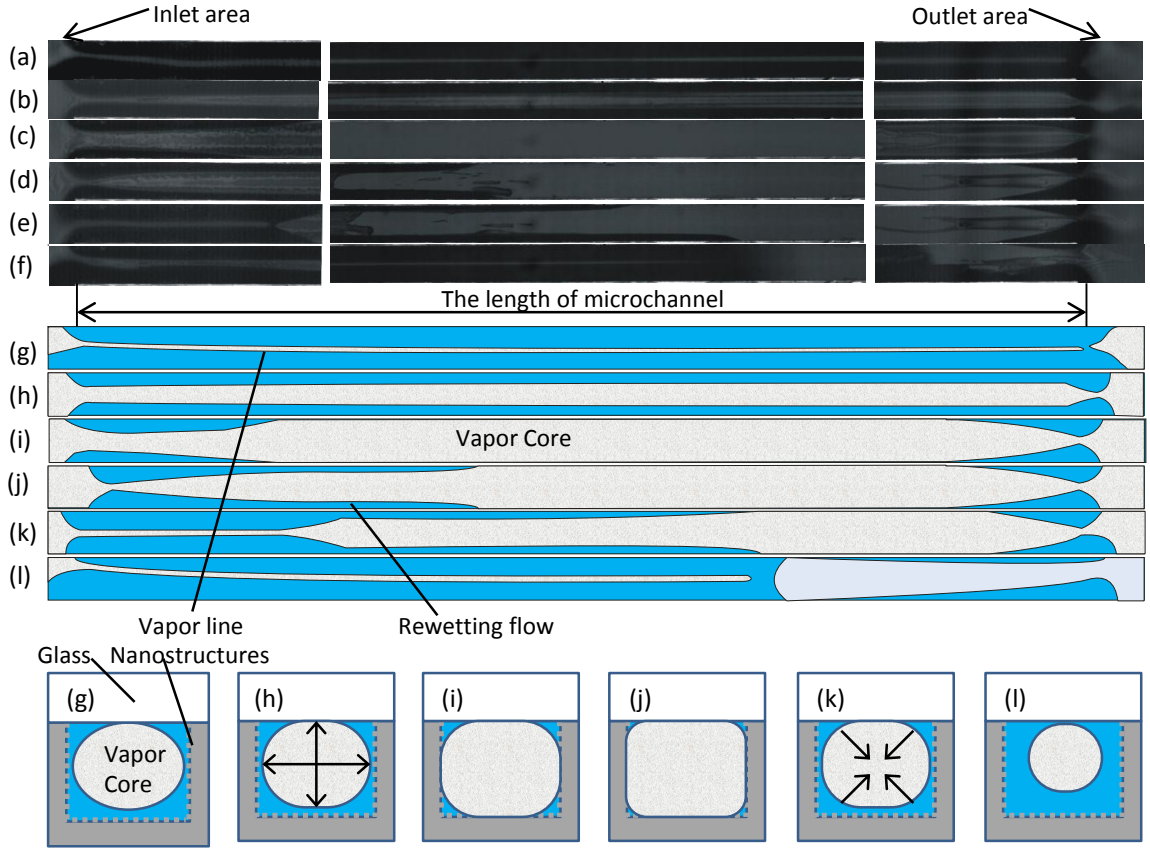

Figure 4.5. Characterization of the single and periodic annular flow in microchannels enabled by SiNWs. (a) to (f) the sequent images of the new flow boiling regime in a typical cycle. These images were captured from the top-view by a visualization system consisting of a high-speed camera (Phantom V7.3) and an optical microscope (Olympus BX-51). Images were taken under working condition: 303 kg/m^2·s and 250 W/cm^2. The white/gray areas denote vapor bubbles and black/dark areas stand for liquid or droplets.

(g) to (l) the schematic maps of top views and cross-sectional views of the new flow boiling regime in a cycle.

In the new flow boiling regime, a vapor core at the center of channels periodically grows and shrinks (Figure 4.5a, b, c, g, h and i) because of the induced high frequency rewetting flows (Figure 4.5d, e, f, j, k and l) by SiNWs (Yang, Dai et al. 2013); while liquid films are on walls. The cross-sectional viewed vapor core was schematically illustrated in Figure 4.5 to assist visualization of the fluid structure in the single and periodic annular flow. These characteristics of the new flow boiling pattern are favorable for heat and mass transfer. Specifically, the high frequency rapid rewetting process (Yang, Dai et al. 2013) triggered by capillary flows on the superhydrophilic bi-porous interfaces can greatly improve CHF by improving the global liquid supply and further enhance HTCs by introducing thin film evaporation and additional advections.

4.3.2 HEAT TRANSFER CURVES AND MAJOR HEAT TRANSFER MODES

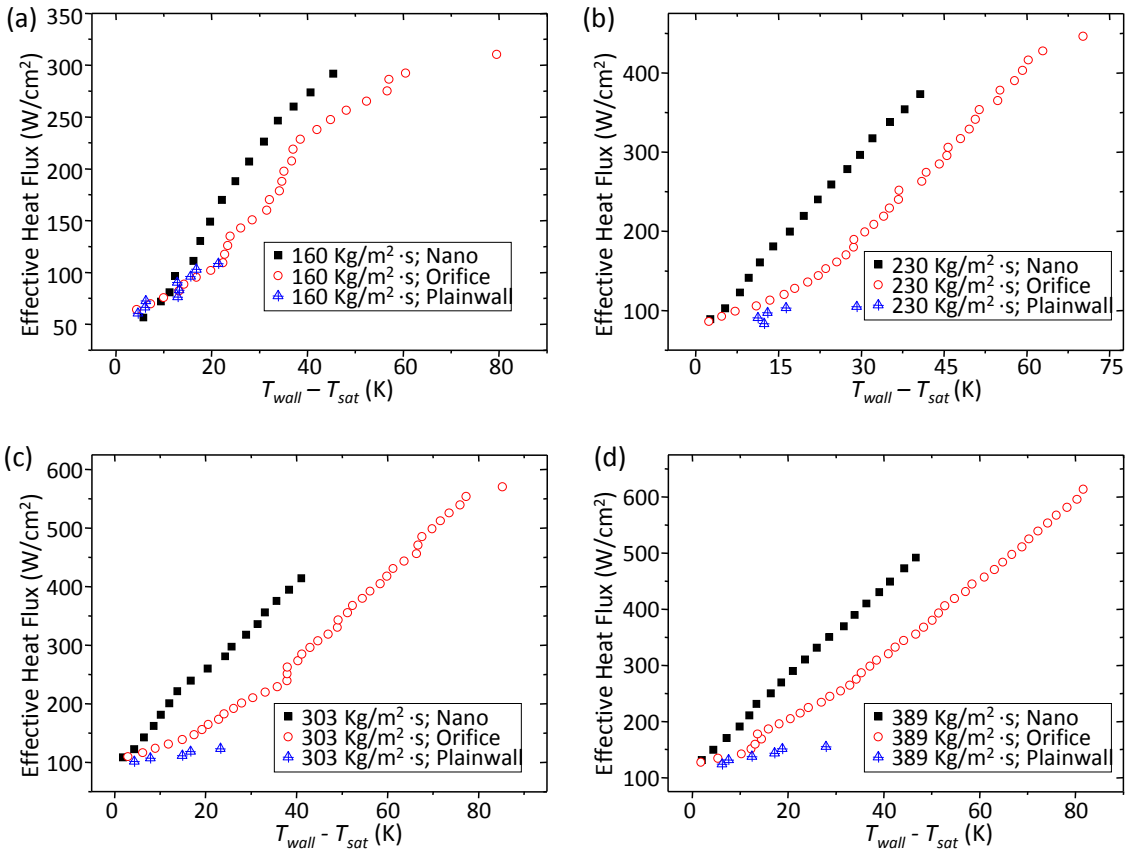

Figure 4.6. Boiling curves at low, medium and high mass fluxes.

In this study, the flow boiling curves, i.e., heat flux versus superheat (Figure 4.6), HTC versus superheat (Figure 4.7), and HTC versus vapor quality (Figure 4.8), were presented. The flow boiling in smooth-wall microchannels and IR microchannels (Figure 4.4c) were compared to understand the enhanced flow boiling in the single and periodic flow boiling regime enabled by SiNWs (Yang, Dai et al. 2013).

From Figure 4.6, for a given superheat, the dissipated heat fluxes, q''_{eff}, in the SiNWed microchannels were the highest among the three types of microchannel configurations with the mass fluxes, G, ranging from 160 to 389 kg/m^2 s. For example,

q''_{eff} is improved from 155 W/cm^2 in smooth-wall microchannels and 240 W/cm^2 in IR microchannels to 350 W/cm^2 at ΔT = 28 K and G = 389 kg/m^2 s.

Additionally, the HTC was plotted as a function of superheat, T_{wall}-T_{sat}, and exit vapor quality, χ, and compared in Figure 4.7 and Figure 4.8, respectively. HTC was dramatically enhanced in SiNWed microchannels in this experimental study. Figure 4.7 shows that HTC was significantly enhanced from 25.2 kW/m^2 ·K in the smooth-wall microchannels to 65.2 kW/m^2 ·K in SiNWed microchannels under the working condition of ΔT = 28 K and G = 389 kg/m^2 s. HTCs in the SiNWed microchannels can be improved up to 326 % (i.e., from 29.6 kW/m^2 ·K to 96.3 kW/m^2 ·K) compared with the smooth-wall microchannels under a similar working condition, i.e, χ = 0.07 and G = 230 kg/m^2 s. HTCs in the IR microchannels were between these in the smooth-wall microchannels and SiNWed microchannels (Schneider, Kosar et al. 2006).

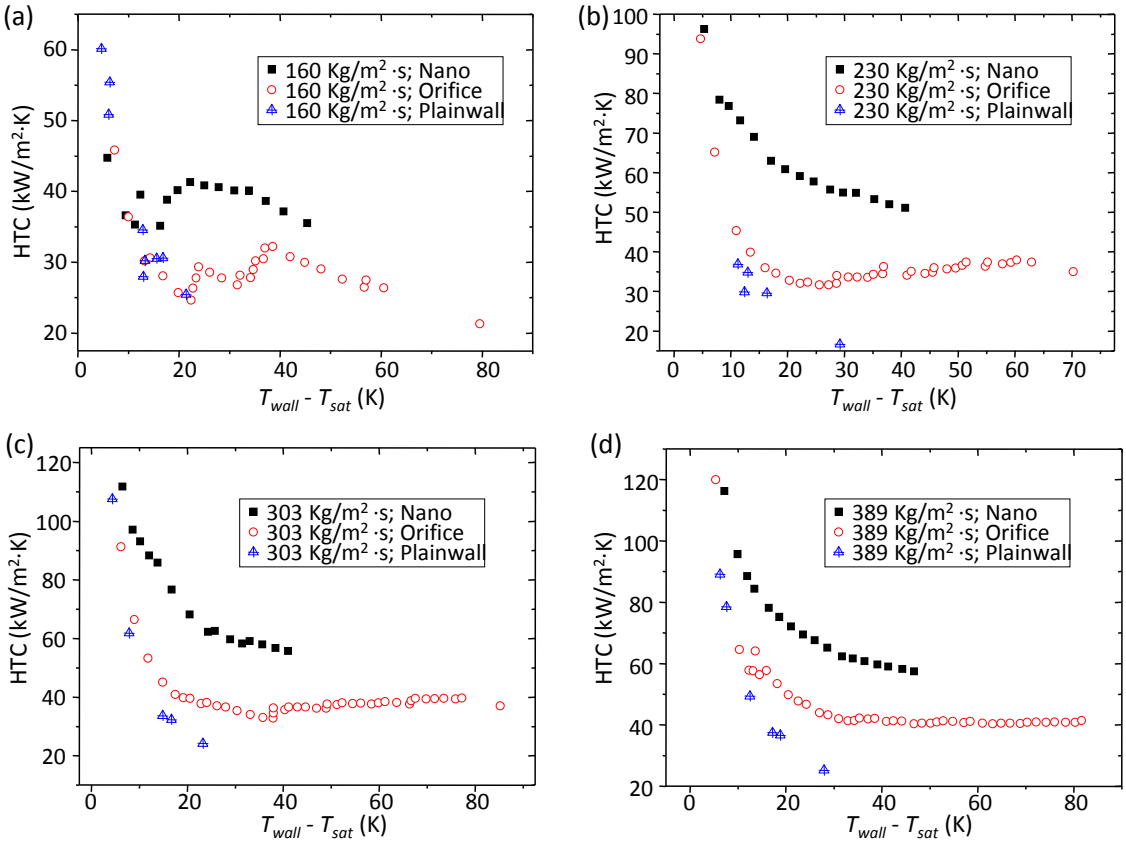

Figure 4.7. The average HTC as a function of superheat under various mass fluxes.

As shown in Figure 4.8, the smooth-wall channel cannot work at a high exit vapor quality, χ, (i.e., usually less than 0.1) because the premature CHF (Bergles and Kandlikar 2005). Microchannels with IRs can work at an exit vapor quality, χ, as high as 0.55, but only deliver HTCs at a magnitude of 40 kW/m^2 ·K, which could be caused by the partial dry area resulting from vapor slugs inside microchannels (Wang, Cheng et al. 2008).

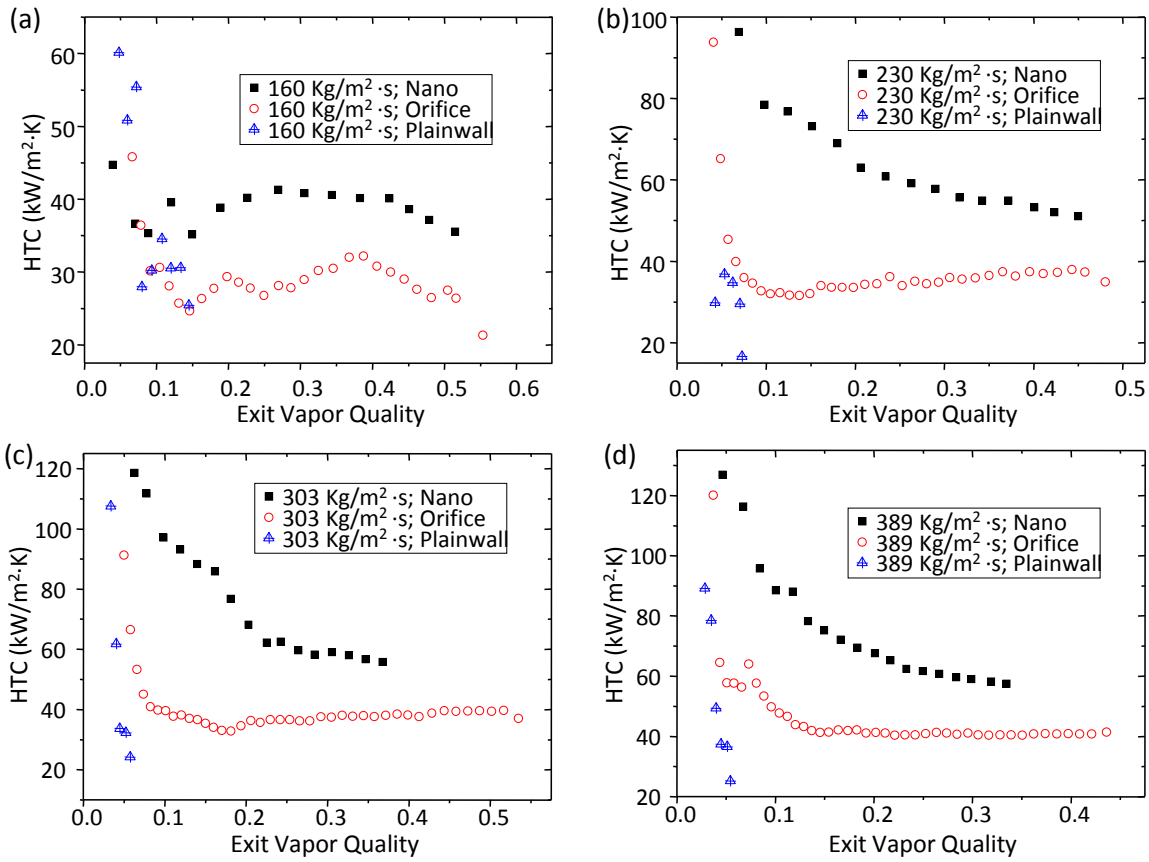

Figure 4.8. The average HTC as a function of exit vapor quality under various mass fluxes.

However, without applying IRs, SiNWed microchannels can work at an exit vapor quality as high as 0.52, more importantly, with a significantly higher averaged HTC, 60 kW/m^2 K by promoting thin film evaporation and nucleate boiling as well as advections using capillarity (Yang, Dai et al. 2013). This implies that IRs can be used to effectively suppress flow instabilities, but not as efficient as SiNW boiling surfaces in enhancing HTC as illustrated in this study.

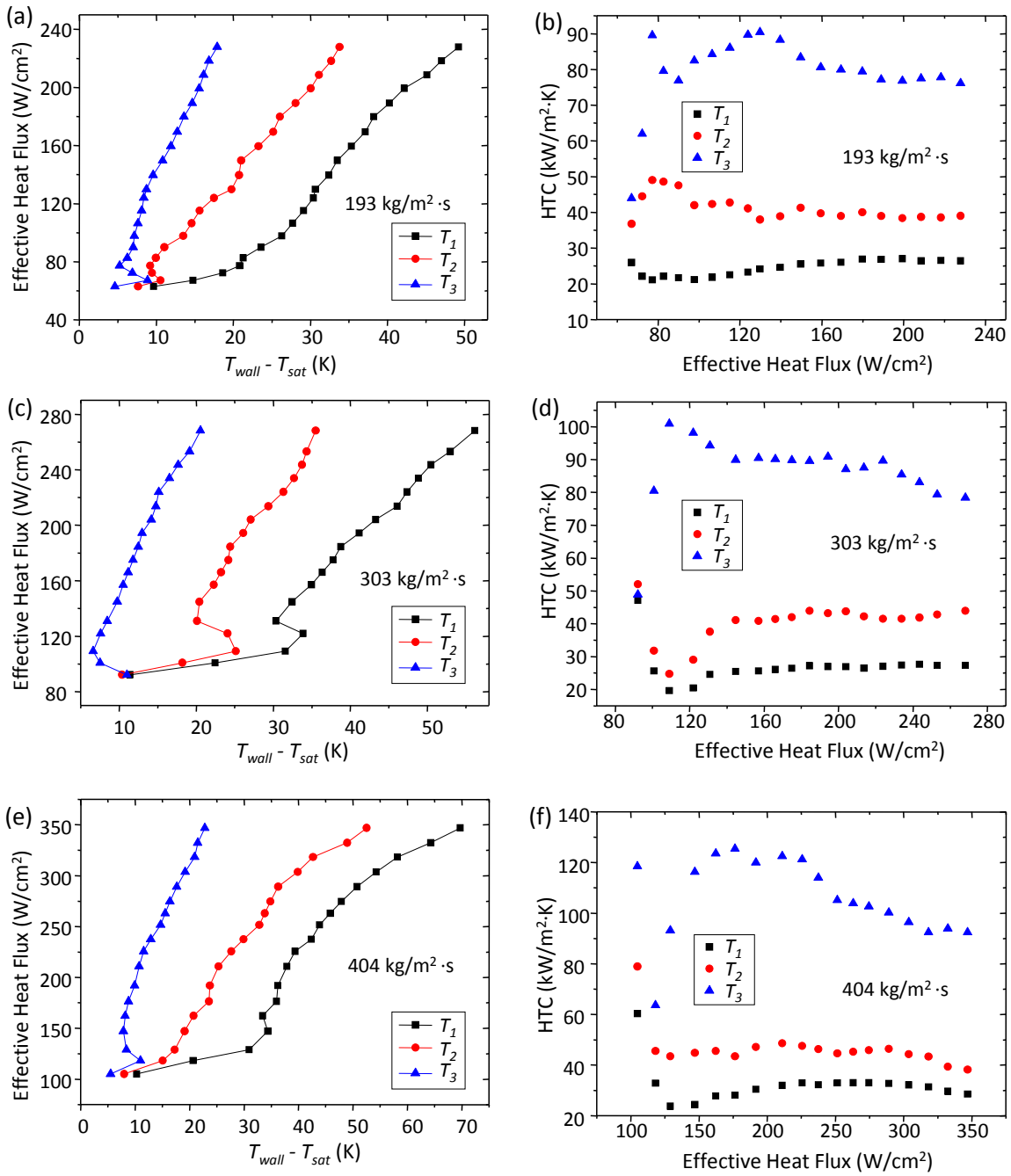

Figure 4.9. Comparison of local heat transfer performance in microchannels. T_1, T_2 and T_3 represents thermistors locate at the entrance, 1/3 length and 2/3 length along the channel from the entrance, respectively. (a), (c) and (e) the effective heat fluxes as a function of superheats at various mass fluxes and positions. (b), (d) and (f) the local HTCs as a function of superheats under various mass fluxes.

To further understand the heat transfer mechanism, the local boiling and heat transfer curves were studied and summarized in Figure 4.9 under various mass fluxes.

The locations of local thermistors were described in Figure 4.3. From Figure 4.9, it was shown that the HTC highly depended on the location in the microchannels. Moreover, as illustrated in Figure 4.9, the strong dependence of HTC on locations is consistent with the distribution of liquid film thickness (Figure 4.5), implying the contribution of the thin film evaporation in the enhanced HTCs. Additionally, Hysteresis in the region of nucleation incipience (Nukiyama 1966) was observed in all locations as shown in Figure 4.9a, c, and e. Thus, nucleate boiling should be one of the basic heat transfer modes during flow boiling in SiNWed microchannels.

Specifically, HTCs near the entrance indicated by T_1 were the lowest during the entire flow boiling domain. As observed in the visualization study (Figure 4.5), the heat transfer in the entrance should be dominated by single-phase convection and nucleate boiling since the annular flow was not fully established near the entrance. The resulting low HTCs should be the lack of thin film evaporation heat transfer and advections induced by capillarity. The other two thermistors were located at a distance of 1/3 and 2/3 of total channel length from the entrance inside the SiNWed microchannels. As shown in Figure 4.9, HTC was significantly improved at these two locations because of the enhanced nucleate boiling, the thin film evaporation and advections induced by capillary flows in the single and periodic annular flow (Yang, Dai et al. 2013). Noted that the highest HTCs, which was located at the 2/3 of channel length (i.e., the thermistors 3 in Figure 4.3), were 90 to 150 % higher than the second highest HTC at the location of 1/3 of channels. The local HTC was up to 125.4 $kW/m^2 \cdot K$ at a mass flux of 404 $kg/m^2 s$ because of the ultra-efficient thin film evaporation and strong advection adjacent the frontier area of rewetting.

The existence of the hysteresis in the region of nucleation incipience (Figure 4.9a, c, and e) indicated the popularity of nucleate boiling in the whole boiling regime. Equally important, the consistence of the distributions of the local HTCs and liquid film thickness in the single and periodic annular flow (Figure 4.5) well implied the primary role of thin film evaporation in enhancing HTC during flow boiling in the SiNWed microchannels. The high frequency rewetting induced by superhydrophilic SiNWs would introduce strong advections (Yang, Dai et al. 2013).

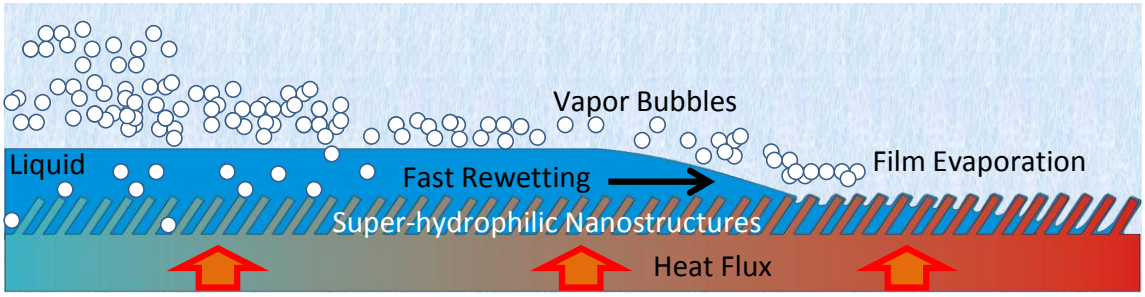

Figure 4.10. A comprehensive schematic map of heat transfer mechanisms in nano-engineered microchannels, including nucleation boiling heat transfer, advection heat transfer and thin-film evaporation heat transfer.

As schematically shown in Figure 4.10, three major heat transfer modes were involved during flow boiling in the SiNWed microchannels. These include nucleate boiling, thin film evaporation and advection. The nucleate boiling on SiNW boiling surfaces should be dominant in the upstream of the microchannels because the heat transfer surface was submerged in the working fluid most of the time; while the thin film evaporation and advections govern the heat transfer in the downstream because of the thin liquid film and high frequency capillary flows induced by the superhydrophilic SiNWs (Yang, Dai et al. 2013).

4.3.3 ENHANCED NUCLEATE BOILING

Visualization study and theoretic analysis were conducted to understand bubble dynamics in SiNWed microchannels, which led to a better understanding of the role of the nucleate boiling behind the dramatically enhanced HTC. Through the use of novel and optimized nanoscale boiling surfaces in microchannels, the bubble sizes during flow boiling were reduced to be less than 5 μm, i.e., termed nanobubbles (NBs). It was experimentally demonstrated that the nano-engineered boiling surfaces could not only reduce the bubble departure diameter (Liu, Li et al. 2011;Yang, Dai et al. 2013) but also increase the nucleate site density. In this study, the active bubble nucleation sites, as highlighted by dashed lines in Figure 4.11a and b, was estimated at a magnitude of 10^{10} m^{-2} on the SiNW boiling surfaces because of the interactions between interconnected and super-hydrophilic nano/micro-cavities (Li, Wang et al. 2008).

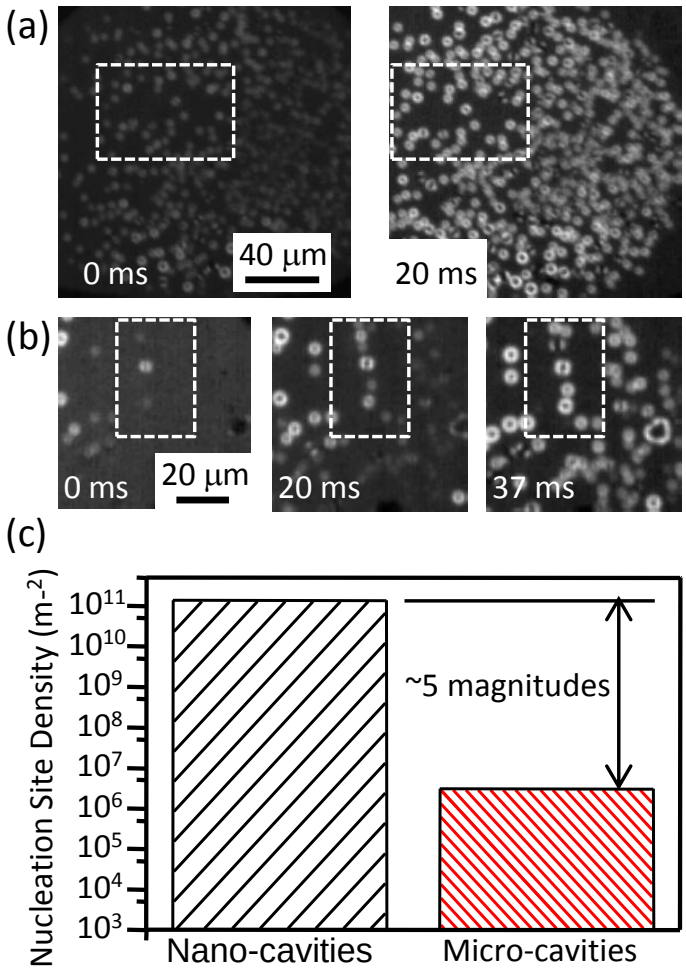

Figure 4.11. Enhanced nucleation boiling near entrance areas. (a) and (b) bubble nucleation at an effective heat flux of 70 W/cm^2 and a mass flux of 213 kg/m^2 s. (c) Active nucleation site density on a boiling surface with superhydrophilic SiNWs and smooth walls.

As shown in Figure 4.11c, this value is four orders of magnitudes larger than that in plain-wall microchannels during flow boiling (Kuo, Kosar et al. 2006). Such an enhancement on nucleation site density should be primarily caused by the enhanced surface wettability (Liu, Li et al. 2011) and the reduced cavity size (Li, Wang et al. 2008), both of them are critical to determine the bubble departure diameter and frequency.

To better understand the enhanced nucleate boiling, a theoretical study was conducted to obtain qualitatively understandings. An equation to describe bubble departure process, was developed from force analysis (Thorncroft and Klausner 2001),

$$F_{QS} + F_{AM} \simeq F_C \tag{44}$$

, where, F_{QS} , F_{AM} , and F_C , are quasi-steady drag force, added mass force (or inertia force), and anchoring capillary force. The quasi-steady drag force, F_{QS} , can be estimated from the equation developed in (Thorncroft and Klausner 2001),

$$F_{QS} = 3\pi\rho_l \nu \left(\bar{u} - u_b\right) D_b \left\{ \frac{2}{3} + \left[\frac{12}{\mathrm{Re}_b} + 0.75\left(1 + \frac{3.315}{\mathrm{Re}_b^{0.5}}\right)\right]^{-1} \right\} \tag{45}$$

where, bubble departure diameter is, D_b ; the bubble Reynolds number is given by $\mathrm{Re}_b = D_b(\bar{u} - u_b)/\nu$; ρ_l is the density of liquid; $\bar{u}$ is average flow velocity; u_b is the bubble growth velocity; and *v* is the kinematic viscosity. F_{AM} , is stated as (Thorncroft and Klausner 2001)

$$F_{AM} = 2\pi\rho_l D_b^2 \bar{u} \dot{D}_b \tag{46}$$

where, the bubble inclination angle could be neglected in microchannels on the horizontal direction. The anchoring capillary force is estimated from,

$$F_C = \pi D_c \gamma \sin\theta \tag{47}$$

In the previous study (Li, Tseng et al. 2004), bubble growth rate in term of bubble diameter, $\dot{D}_b$, was assumed to be a positive constant. While a bubble is growing at a nucleation site, drag force F_{QS} , and inertial force, F_{AM} , can balance, capillary force, F_C , to assist bubble departure as indicated in Eq. 9. Additionally, Eq. 10 and 11 implied that

drag force, F_{QS}, and inertial force, F_{AM}, shall increase as bubble departure diameter, D_b, increasing. These implications agreed with experimental results (Li, Tseng et al. 2004;Kuo, Kosar et al. 2006) that the departure diameter of regular size bubbles on smooth surface with a contact angle of approximately 36 °(Liu, Li et al. 2011) was at a magnitude of millimeter. However, when the apparent contact angle on a super-hydrophilic bi-porous interface was assumed to nearly zero (estimated at less than 0.1 °) (Chen, Lu et al. 2009;Liu, Li et al. 2011). According to the Eq. 12, a smaller contact angle, θ, would lead to a smaller anchoring capillary force, F_C. It implies that an earlier and faster departure of small bubbles could be achieved because the required forces to assist the departure of bubbles, i.e., drag force, F_{QS} and inertial force, F_{AM}, are reduced. Noted that the drag force, F_{QS}, is an order of magnitude higher than capillary force, F_C when the bubble diameter is less than 5 μm (Yang, Dai et al. 2013).

The magnitude of the increased bubble departure frequency, *f*, which cannot be measured in this experimental study, can be estimated from the energy equation developed in (Mikic, Rohsenow et al. 1970)

$$fN_a = \frac{q_b''}{K\Delta T\sqrt{\pi k_l C_p}}\frac{1}{D_b^2\sqrt{\gamma}} \tag{48}$$

where, k_l, D_b, f, N_a and γ, are the liquid thermal conductivity, bubble departure diameter, bubble release frequency, nucleation site density and surface tension, respectively. K is a constant. Two-phase heat transfer coefficient, h_{tp}, can be related to bubble departure frequency, f, nucleation site density, N_a, and bubble departure diameter, D_d, as shown in Eq. 14.

$$h_{tp} = \frac{q''_b}{\Delta T} \sim f N_a D_b^2 \quad (49)$$

Compared to plain-wall microchannels, with approximately 300% enhancement in h_{tp} (Figure 4.7 and Figure 4.8), 10^5 times higher in nucleation site density, N_a (Figure 4.11), and the 10^{-3} times less in departure diameter, D_b (Figure 4.11) (Yang, Dai et al. 2013) in SiNWed microchannels, the departure frequency, *f*, should be an order of magnitude higher than that on plain-wall microchannels. Even though existing models to predict the growth characteristics based on regular-sized bubbles are not applicable at nanoscale, they are still insightful to qualitatively understand the mechanism of enhanced nucleate boiling.

4.3.4 PROMPTED THIN FILM EVAPORATION AND ADVECTIONS

In the previous section, the enhanced nucleate boiling was discussed and analyzed. In this section, the capillary flows and the resulted thin film evaporation, which was induced by the superhydrophilic SiNWs on all inner walls of microchannels as evidenced by the rapid rewetting liquid flows along walls in microchannels (Figure 4.12a), are discussed.

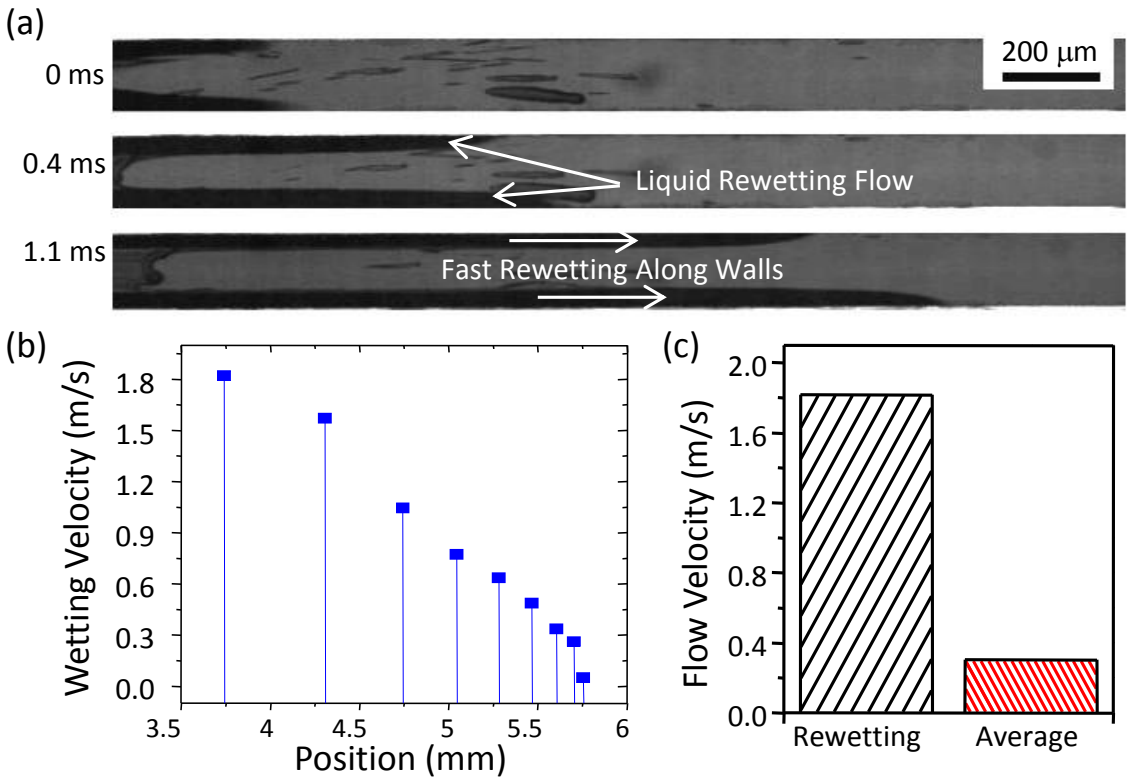

Figure 4.12. The capillary flows along inner walls in microchannels. (a) Visualize capillary flows along inner walls and the high frequency rewetting mechanism. (b) Fast rewetting flows in a microchannel during flow boiling under the working condition: G = 193 kg/m^2 s, χ = 0.4. (c) Rewetting velocity profile during a rapid and periodic rewetting process. (d) The comparison between the average velocity of rewetting flow and average velocity of inlet flow.

As the liquid film thickness decreasing along the flow direction (as shown in Figure 4.12a), SiNWs were eventually exposed to vapor and hence meniscus were formed. As a result, rapid rewetting occurred in a periodic pattern because of the induced strong capillary force generated by superhydrophilic SiNWs. Instead of nucleate boiling, thin film evaporation and advections on the downstream inner walls in microchannels dominated heat transfer. The rewetting velocity profile along the length of the channel is plotted in Figure 4.12b. The strong advections were evinced by the high rewetting velocity, which is approximately five times faster than the average flow velocity as

shown in Figure 4.12c. Additionally, the fast rewetting flow can greatly improve the global liquid supply. The local dry-out inside microchannels could even be eliminated by the capillary flows generated by superhydrophilic SiNWs. The greatly improved liquid supply in the single and periodic annular flows result in high CHF (Yang, Dai et al. 2013). The mechanism behind the enhanced CHF will be discussed in detail in Part II.

The significantly extended thin-film region should be one of the primary reason behind the enhanced HTCs since it produces the highest heat transfer rate due to low thermal resistance across the thickness of liquid film (Kabov, Zaitsev et al. 2011). However, the length of thin-film region in a traditional microchannel is limited to several hundred nanometers as a result of the domination of intrinsic meniscus in a vapor slug (Mukherjee and Kandlikar 2006;Wang, Garimella et al. 2007). On the contrary, in this study, the vapor slugs inside the microchannel were not observed during the entire flow boiling region and process. The transitional flow regimes were reduced to a single and periodic annular flow regime (Yang, Dai et al. 2013). As a result, the thin film evaporating region as schematically shown in Figure 4.10 can be extended to nearly the whole length of microchannels (Figure 4.5) companying a high frequency rewetting during the entire flow boiling process.

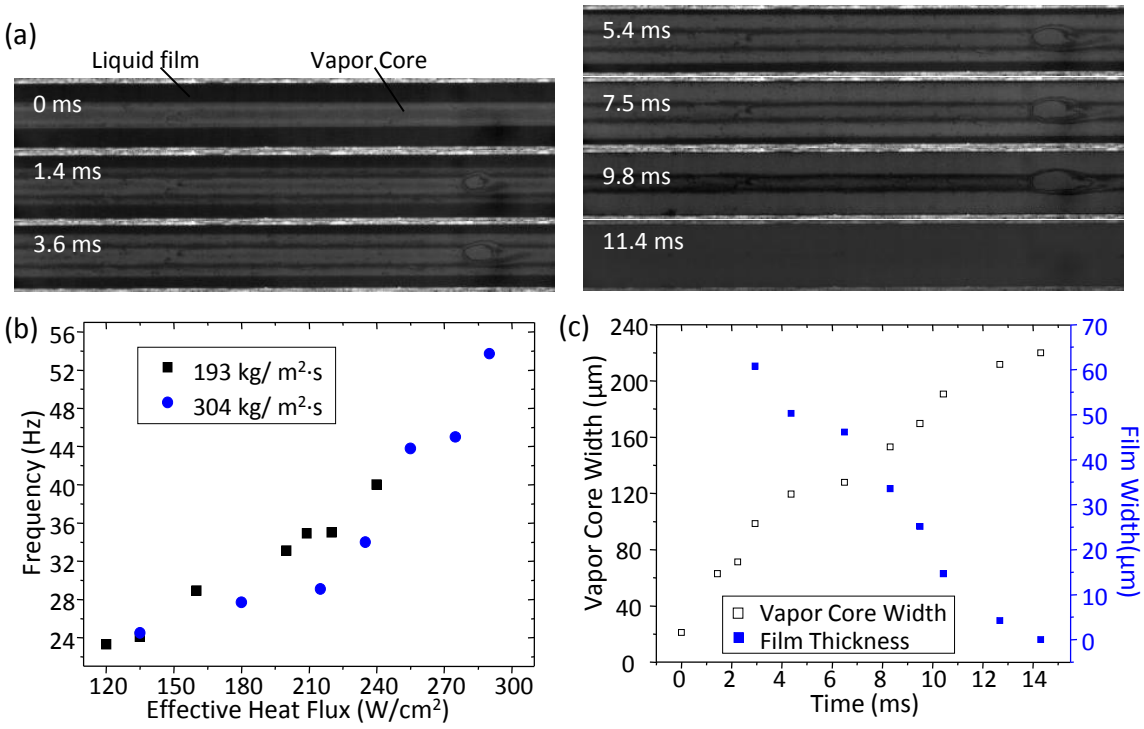

Figure 4.13. Dynamic liquid thin film evaporation and vapor core growth processes. (a) Visualization of liquid thin film evaporation. (b) Transient width of contact lines between vapor core and glass cover as well as liquid film thickness.

A typical film evaporating process was detailed in Figure 4.13a. Once the liquid films resulting from the capillary flows were established inside microchannels, a vapor core at the center of a microchannel (Figure 4.13a) would be formed. The size of the vapor core keeps growing in a cycle as the thin film evaporation and nucleate boiling are intensifying, which were indicated by the gradually decreasing liquid film thickness (Figure 4.13a). When the liquid film was nearly evaporated out, i.e., reaching the minimum thickness, and SiNWs started to dry out; the capillary flows would be resumed by the high capillary pressure induced by hydrophilic SiNWs on inner walls and consequently, triggered rapid rewetting. The width of vapor core and the thickness of liquid film were cyclic at a high frequency (Figure 4.13c) as measured by a high speed camera. A typical change of vapor core size and liquid film thickness with time were

shown in Figure 4.13b. It shows that thin-film could be generated and extended along the length of the microchannel in a short period (~10 ms). Bubble departure and bubbles were not visualized during this process. The local HTC, which should be dominated by thin film evaporation, at furthest position was measured up to 125.4 kW/m^2 K at a mass flux of 404 kg/m ²s.

4.3.5 THE REDUCED PRESSURE DROPS IN SINWED MICROCHANNELS

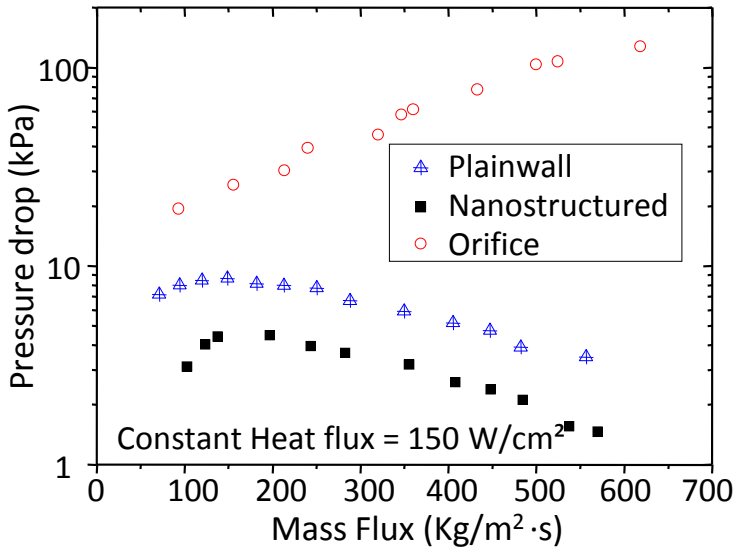

Figure 4.14. Comparison of pressure drops between plain-wall microchannels with & without IRs and SiNWed microchannels. Pressure drops are plotted as a function of mass fluxes

The overall pressure drops of SiNWed microchannels and plain-wall microchannels with or without IRs are plotted as functions of mass fluxes in Figure 4.14. Due to the identical dimensions (height, width, length and number of microchannels) of these three designs, the major difference of pressure drops shall be induced by the frictional resistance of two-phase flow. For example, the inlet restrictors would lead to extra high flow resistance hence large pressure drops. Furthermore, the SiNWed microchannels has significantly lower pressure drop than plainwall microchannels

(Figure 4.14). This result implies that the two-phase flow pattern induced by SiNWed walls has dominating impacts on pressure drops.

4.3.6 THE IMPACTS OF TWO-PHASE FLOW PATTERNS ON PRESSURE DROPS IN MICROCHANNELS

As shown in Figure 4.15a, the existence of vapor slugs generates capillary pressure drop along meniscus at the onset of flow boiling in microchannels with smooth walls then the churn flow are introduced with increasing vapor quality and then superficial vapor velocity (Kandlikar 2002;Serizawa, Feng et al. 2002). These smooth-wall microchannels are fabricated from polished silicon wafers by DRIE with roughness ranging from 3 nm to 300 nm (Chandrasekaran and Sundararajan 2004;Kuo, Kosar et al. 2006). The contact angle between DI water and smooth Si surface is estimated from 40 ٩to 60 °as a result of native oxide layers (Chen, Lu et al. 2009). After growth of SiNWs by an electroless chemical etching method (Kuo-Shen, Ayon et al. 2002), the wettability of inner walls of microchannels were modified into super-hydrophilic with the apparent contact angles less

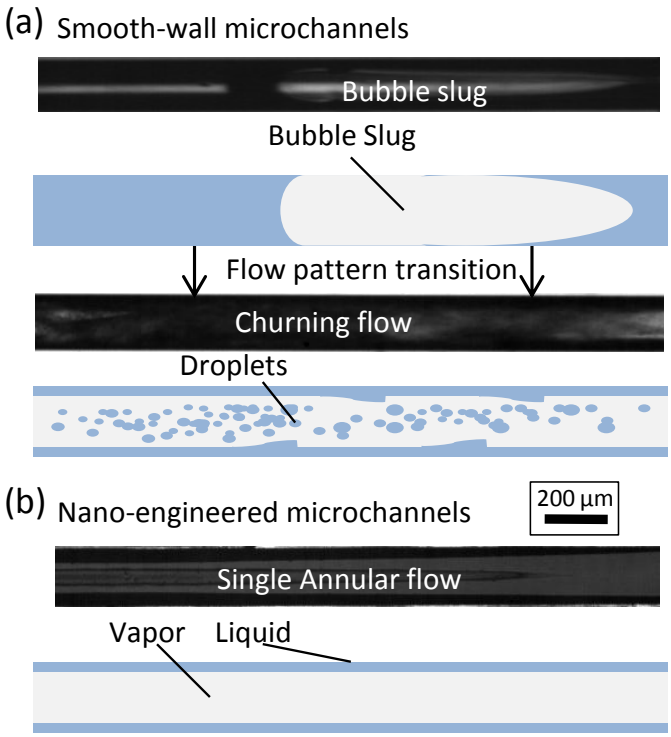

Figure 4.15. Major differences in the fluid structures between traditional flow patterns and the single and periodic flow pattern in microchannels. (a) Slug and churning flows in plain-wall microchannels. (b) The single and periodic flow in SiNWed microchannels.

than 0.1 °by the Wenzel effect (Egatz-Gomez, Majithia et al. 2012). Moreover, the inner wall peak-to-peak roughness was significantly increased to approximate 5 micron. The high capillary pressure generated by the superhydrophilic SiNWs separated laminar liquid and vapor flows. Visualization studies revealed that liquid layer exists between the gas core and the walls of rectangle microchannels (Figure 4.15b) and a significant difference between fluid and vapor superficial velocities was observed. According to visualization studies (Figure 4.15b), it is supposed that surface tension force associated with these nano-coatings redistributed liquid and vapor flows during the convective boiling. Consequently, the multiple and transitional two-phase flow patterns (Fore, Beus et al. 2000;Bonaccurso, Butt et al. 2003;Sbragaglia, Benzi et al. 2006) (Figure 4.15a)

were reduced into a single and periodic annular flow boiling regime (Kandlikar 2002;Serizawa, Feng et al. 2002) (Figure 4.15b). In existing microchannel configurations, annular two-phase flow only occurs at high superficial gas velocity (Vassallo and Kumar 1999). However, in the new flow boiling regime enabled by superhydrophilic SiNWs (Figure 4.16a), the annular flow started from the onset of flow boiling (Peng, Yan et al. 2002). It was noted that the hydraulic diameter of the vapor core was observed to expand periodically (Figure 4.16a). Usually, the adhesion forces between the liquid fluid (water) and smooth walls are not strong enough to form uniform liquid layers onto inner surfaces. Therefore, high-velocity vapor flow could blow liquid away from walls and form a churn flow (Figure 4.16b) unless high adhesion forces were applied on the inner surface by using SiNW coatings.

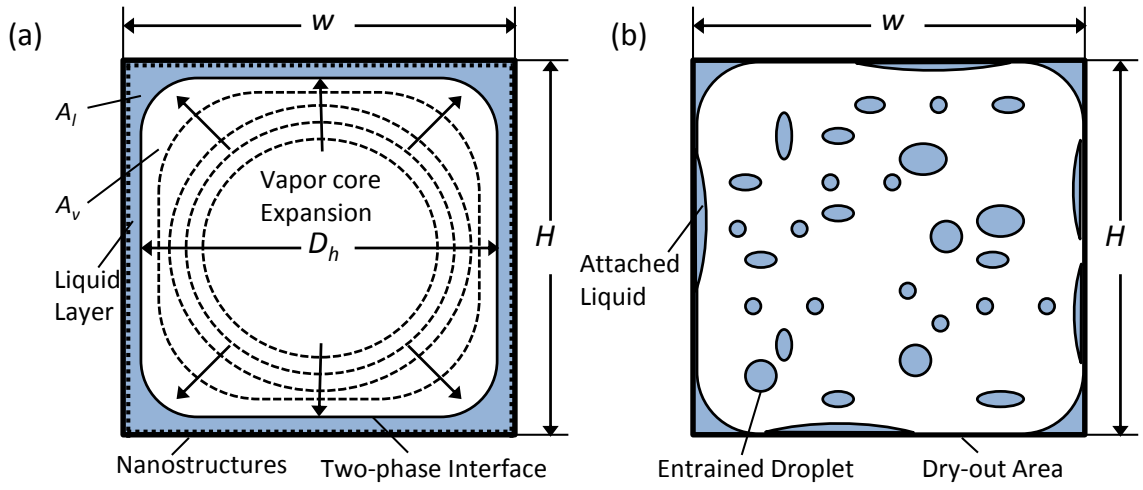

Figure 4.16. The schematic of fluid structures in a cross-sectional view. (a) The periodic expansion of the vapor core in the single and periodic annular flow. (b) Entrained liquid droplets in the churning flow.

4.3.7 REDUCED FRICTIONAL PRESSURE DROP

As a result of superficial velocity difference, there is an interfacial shear stress along interfaces of phases, which lead to frictional pressure drop along the vapor core. We therefore conclude that the frictional pressure drop of two-phase flow is mainly dominated by difference of superficial velocity between liquid and vapor, especially, for annular flow.

The capillary flow on superhydrophilic interfaces could create a smooth liquid layer between the solid wall and annual vapor nanobubble flow to reduce pressure drop (Rovinsky, Brauner et al. 1997). Experimental study quantitatively reveals friction reduction due to unified flow patterns in microchanenls with nanoporous coatings (Figure 4.17a). The frictional pressure drops as functions of Reynolds number of exit vapor flow are plotted in Figure 4.17b. In the view of experimental results in Figure 4.17b, the frictional pressure drop is dominated by Re of vapor core. And the optimized flow structure in this study, which is well-separated annular two-phase flow, would reduce interfacial shear stress by containing less entrained droplets in the vapor core. The two-phase pressure drop during the entire convective boiling can be reduced approximately 48 % compared with microchannels with smooth walls.

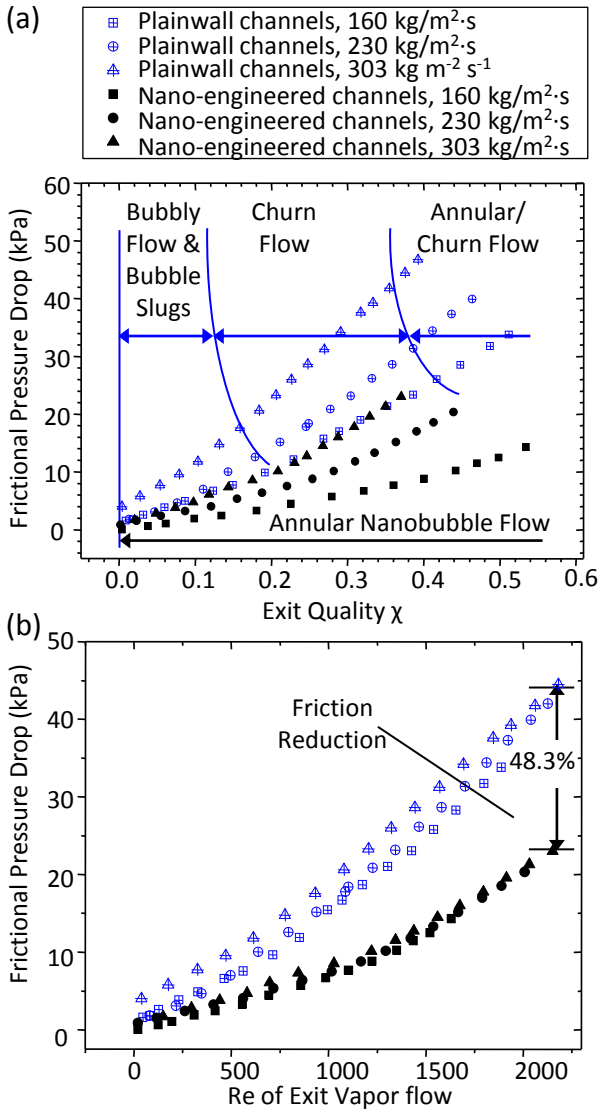

Figure 4.17. Comparisons of pressure drops between traditional flow boiling regimes and the single and periodic annular regime. (a) Pressure drops as functions of exit vapor qualities. (b) Pressure drops as a function of Re based on exit vapor flow.

4.3.8 ANALYSIS OF FRICTIONAL PRESSURE DROP REDUCTION

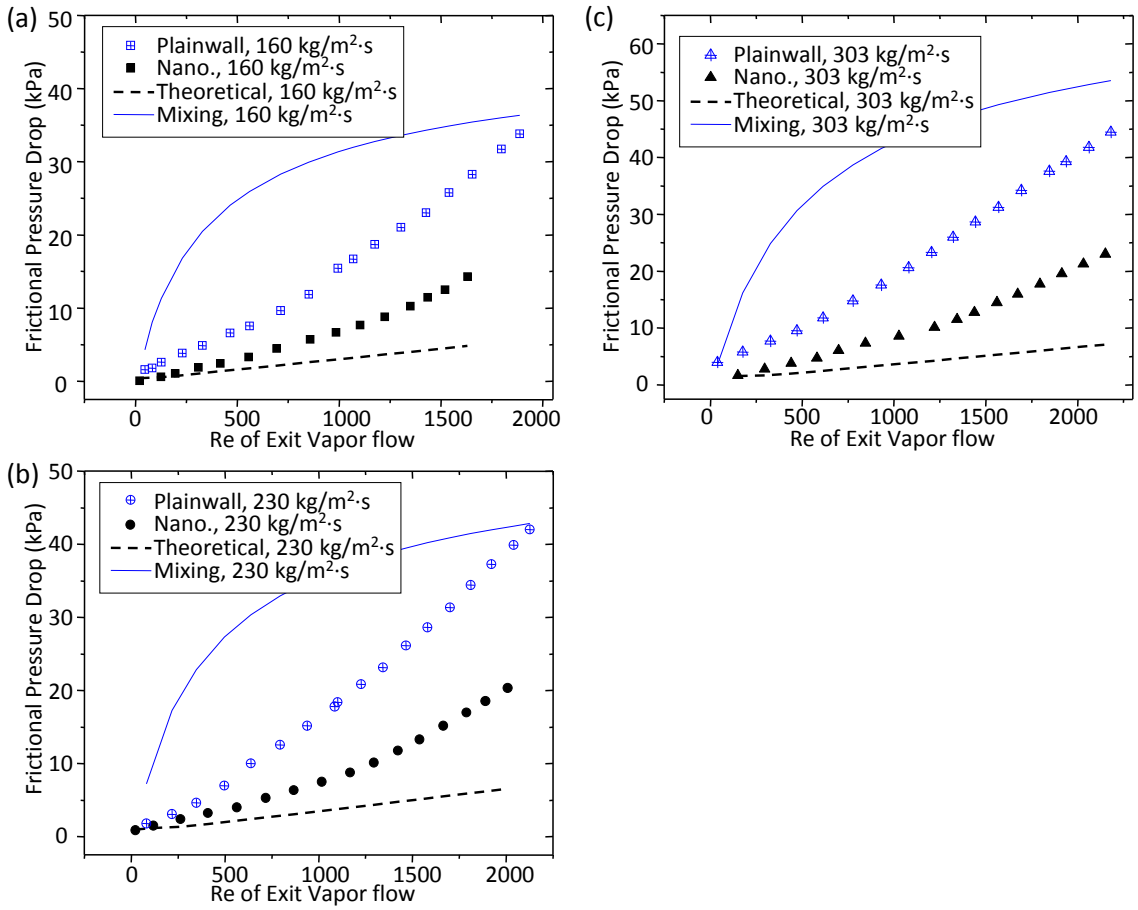

Figure 4.18. Analysis of pressure drops under various mass fluxes. (a) G = 160 kg/m^2 s, (b) G = 230 kg/m^2 s, and (c) G = 303 kg/m^2 s.

It is important to better understand how flow patterns affect on the inner shear stress in two-phase flow. A non-homogeneous thermo-hydraulic model theoretically estimates the frictional pressure drop of the "ideal" annular flow (minimum friction) as shown in Figure 4.16b and Figure 4.15a. A homogeneous two-phase flow in Figure 4.15a and Figure 4.16b is also modeled to show the highest frictional pressure drop. The first theoretical model assumes that no liquid are entrained into vapor flow so that it has minimum pressure drop. The second model assumes homogeneous fine liquid droplets are fully mixed into vapor flow (similar like churn flow) with much higher frictional

pressure drop. Comparison between these two models helps us deliver an explanation of the friction reduction. Top-viewed liquid and vapor distribution of this well-separated annular flow in a microchannel is depicted in Figure 4.19a.

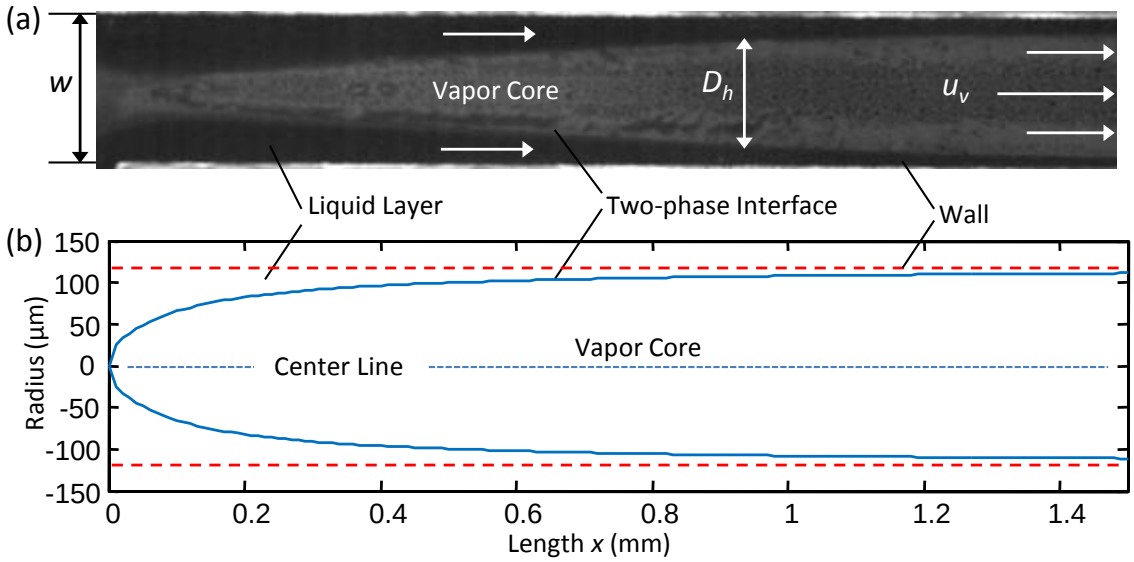

Figure 4.19. The typical fluid structure in the lateral direction in the single and periodic annular flow. (a) The top-viewed image of single and periodic annular flow. (b) The modeled profile of fluid structure in the single and periodic annular flow.

There are several major assumptions in this model to simplify this problem: first, although the flow boiling process is a dynamic process, we approximately consider this process as an equivalent steady state. Secondly, the major contribution of frictional pressure drop is the drag of high-velocity vapor inside the annular liquid flow. Thirdly, the vapor core is concentric. Forth, all vapor flows into the downstream direction (Because the reverse flow is successfully suppressed by eliminating elongated vapor slugs as shown in Figure 4.19 of Part I, the reserve flow in annular NB flow is ignored in this model). Finally, the vapor flow and liquid flow are viscous laminar flows (Re < 2100).

Along axial direction of a uniformly heated microchannel during flow boiling, assuming fluid is saturated at the inlet of microchannel, the local vapor mass flow rate $\dot{m}_v$ is linearly increased along axial direction *x* as a result of uniformly distributed heat energy. $\dot{m}_v = (x/L)P_{eff}/h_{fg}$, where *L* is the length of microchannel and h_{fg} is the latent heat. Then local vapor quality is $\chi = \dot{m}_v/\dot{m}$, where $\dot{m}$ is the total mass flow rate. And local void fraction of two-phase flow,

$$\alpha = 1/\left(1+\frac{1-\chi}{\chi}\frac{\rho_v}{\rho_l}S\right) \tag{50}$$

For non-homogeneous annular flow, the superficial velocity of vapor flow u_v shall be significantly larger than the superficial velocity of annular liquid flow u_l. Therefore the slip correlation *S* is necessary to calculate void fraction. Assuming that no liquid droplet is entrained in the central vapor core as an ideal annular flow, S. M. Zivi proposed a void fraction model based on minimum kinetic energy of the annular flow (Vassallo and Kumar 1999). Where the minimum value of kinetic energy is found, the slip correlation is

$$S = (\rho_l/\rho_v)^{1/3} \tag{51}$$

Then, the theoretical annular flow pattern is given in Figure 4.19b by using this theory. It shares many important characteristics with visualization results in Figure 4.19a, including gradually growth of vapor core and annular liquid layers. However, there is lack of instrumentation for microscale void fraction measurements.

Although rewetting on solid walls is a dynamic process and then liquid flow along walls is not constant, an equivalent steady state is assumed for simplified calculation of

local velocities. In this steady state with minimum kinetic energy, $u_v = \dot{m}\chi/(A_v\rho_v)$ and $u_l = \dot{m}(1-\chi)/(A_l\rho_l)$, where the cross-section area of vapor core is $A_v = \alpha A_c$ and the cross-section area of annular liquid is $A_l = (1-\alpha)A_c$ (Figure 4.15a). A_c is the cross-section area of the microchannel. And the hydraulic diameter of vapor core could be estimated as,

$$D_h = 2\sqrt{A_v/\pi} \tag{52}$$

Unless D_h is larger than the width of microchannel,

$$D_h \approx 2\sqrt{\frac{A_v}{A_c}}\frac{WH}{(W+H)} \tag{53}$$

where *W* and *H* are the width and height of microchannel, respectively. According to this model, a map of liquid and vapor distributions at the length of microchannel is illustrated in Fig. 4b. Assuming the vapor core is a laminar flow of incompressible gas, a differential equation of frictional pressure drop along axial direction is derived as

$$\Delta p_{f,annular} = 0.5\int_0^L \frac{f\rho_v(u_v-u_l)^2}{D_h}dx \tag{54}$$

, where fanning friction factor, $f = C_f/\mathrm{Re}$. And C_f is 58 for a rectangle vapor core or 64 for a round vapor core in fully developed laminar flow. The Reynolds number of vapor flow is

$$\mathrm{Re} = \rho_v(u_v-u_l)D_h/\mu_v \tag{55}$$

where, μ_v, is the dynamic viscosity of vapor.

Current experimental study turn outs that the transitions between churning flow and other flow patterns (Figure 4.14a) occurs during flow boiling in a plain-wall

microchannel (Kandlikar 2002;Serizawa, Feng et al. 2002) and leads to the entrainment of large portion of liquid in the vapor flow (Figure 4.15a). If assuming this two-phase mixture as fluid continuum when fine droplets are significantly smaller than D_h of the vapor core, the mean viscosity of two-phase mixture in churning flow μ_m is higher than single-phase vapor flow. And the mean viscosity, mean density of two-phase mixture and mean velocity are supposed to be,

$$\begin{aligned} \mu_m &= \left[x / \mu_v + (1-x) / \mu_l \right]^{-1} \\ \rho_m &= \alpha \rho_v + (1-\alpha) \rho_l \\ u_m &= \dot{m} / (\rho_m A_c) \end{aligned} \tag{56}$$

In this model, two-phase mixing flow is assumed as homogeneous flow so that slip correlation *S* is 1. An equation of pressure gradient is derived as:

$$\Delta p_{f,mixture} = 0.5 \int_0^L \frac{f_m \rho_m u_m^2}{D_h} dx \tag{57}$$

where,

$$f_m = C_f / \mathrm{Re}_m \tag{58}$$

and

$$\mathrm{Re}_m = \rho_m u_m D_h / \mu_m \tag{59}$$

From the theoretical predictions, the homogeneous two-phase mixing flow has the maximum pressure drop; while the ideally separated annular flow has the lowest pressure drop. By comparing the theoretical predictions and experimental results in Figure 4.18, the pressure drop resulted from the single and periodic flow boiling regime are between two ideal flow patterns (i.e., annular and churn flows) predicted from modeling. Though these models may not be highly accurate, it still strongly suggested that frictional

pressure drop can be greatly reduced by reducing entrained rate of small droplets. In experimental study, smooth walls are unable to suppress the mixing between liquid and vapor at high superficial velocity of vapor flow (or high Re) and then lead to higher interfacial stress. However, SiNWed surfaces successfully reduce flow friction through better separation of liquid and vapor flow.

4.3.9 FLUID STRUCTURE AT THE LIQUID-VAPOR INTERFACE IN THE SINGLE AND PERIODIC ANNULAR FLOW

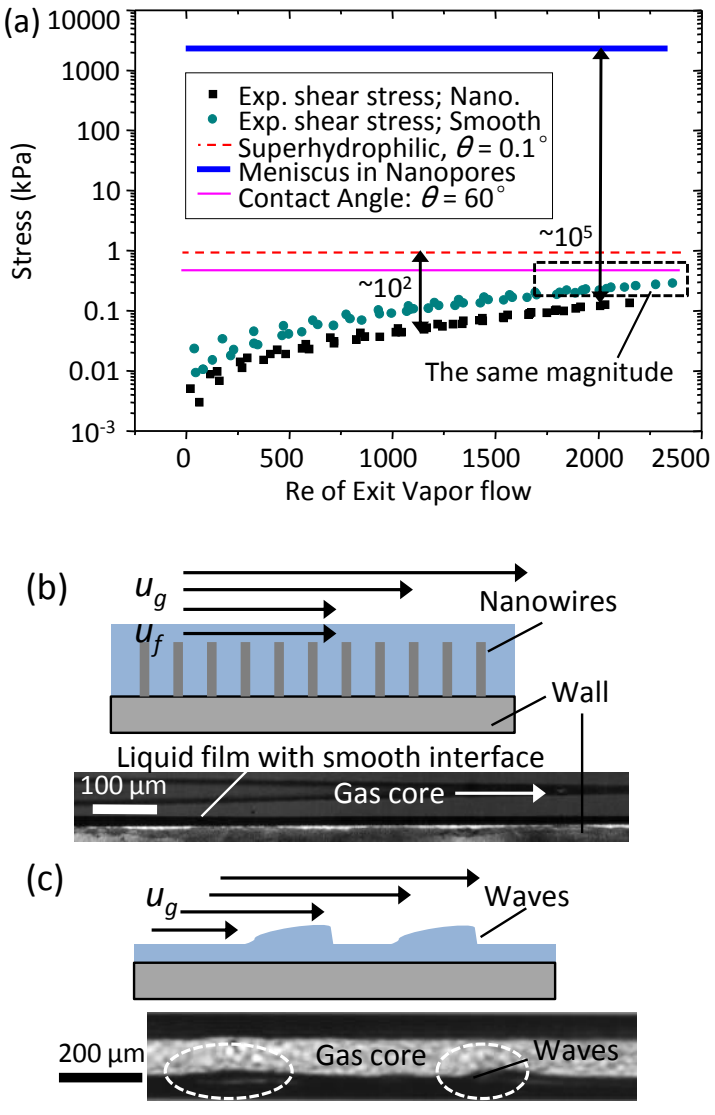

Figure 4.20. Effects of interfacial shear stress and capillary pressure on the profile of liquid-vapor interface during flow boiling in microchannels. (a) Average shear stresses reduced from experiments were plotted as a function of Reynolds number of exit vapor flow and compared to capillary pressure generated in the cross-sectional direction in smooth-wall microchannels and in the inner-wall direction on SiNWs. (b) Image and schematic of nearly flat liquid-vapor interface in the single and periodic annular flow in the SiNWed microchannels. (c) Image and schematic of wavy liquid-vapor interface in smooth-wall microchannels.

To better understand the formations of different flow patterns, interfacial stresses along axial pressure gradient, which are necessary to overcome the surface tension along axial direction of microchannel and nanoscale meniscus in nanoporous coatings, are compared in Figure 4.18. The interfacial stress is estimated from frictional pressure drop:

$$\sigma_i = \frac{\Delta p_f D_h}{4L} \tag{60}$$

To overcome the surface tension, deform the meniscus and separate droplets from liquid layer, the interfacial stress should be equal to or larger than pressure drop across the interface,

$$\Delta p_c = \frac{4\gamma \cos\theta}{d_n} \tag{61}$$

, where γ is surface tension, θ is the contact angle and d_n is the characteristic length. In this study, the d_n could be hydraulic diameter of microchannels and average diameter of cavities for calculation of pressured drop across meniscus within microchannels and nanoscale cavities, respectively. The comparison indicates that the experimental interfacial shear stress in SiNWed microchannel is about two orders or even five orders of magnitude smaller than required stress to overcome surface tension on superhydrophilic interface or on nanoscale meniscus, respectively. It implies the flow pattern is strongly dominated by surface tensions but not interfacial shear stresses. On the

other hand, Figure 4.20 indicates that σ_i along smooth silicon surfaces (contact angle is ~60 °) and its Δp along meniscus are in the same magnitude. It means none of them are dominating during formations of flow patterns. Therefore, flow pattern transitions between annular flow (capillary tension dominates) and churning flow (interfacial shear stress dominates) could occur. In Figure 4.20b and Figure 4.20c, visualization study shows experimental evidences to support above results. The smooth interface between vapor and liquid is shown in Figure 4.20b; the vapor gas core is in the middle of microchannel. A smooth liquid layer between vapor core and solid walls is generated by a fast rewetting process as a result of superhydrophilic wicking nanostructures. In the other case, the interfacial shear stress along two-phase interface induces waves along smooth walls as shown in Figure 4.20c. Then liquid droplets depart from solid walls and could be entrained into fast vapor flow as a part of churn flow in Figure 4.15a.

4.3.10 CHF MECHANISM IN THE SINGLE AND PERIODIC ANNULAR FLOW

The transition of two-phase flow patterns from bubbly flow to slug flow has been considered to be the primary cause of severe two-phase flow instabilities and pre-mature CHF (Zhang, Tong et al. 2009). In smooth-wall microchannels, flow boiling usually reached its pre-mature CHF, which is less than 155 W/cm^2 (Figure 4.21). The two-phase flow instabilities were controlled by inlet restrictors. According to previous study (Kosar, Kuo et al. 2006), the inlet restricted microchannels could provide even higher CHF in microchannels with similar dimensions. However, their high flow resistance leads to extra pressure drop into the whole systems and requires more pumping power (Figure 4.14).

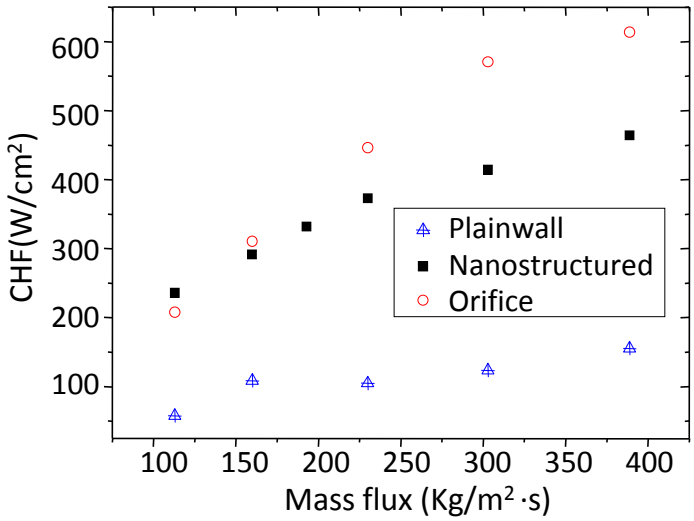

Figure 4.21. Comparison of CHF between plain-wall microchannels with & without IRs and SiNWed microchannels. CHFs are plotted as functions of mass fluxes.

The CHF mechanism in SiNWed microchannels is different from plain-wall microchannels. Capillary forces in SiNWed microchannels not only separate liquid from vapor flow but create a rewetting flow, which leads to higher CHF (Figure 4.21a) with

even less pressure drops (Figure 4.14). CHF has been improved up to 491 W/cm^2 at a moderate G = 389 kg/m^2 s in microchannels coated with SiNWed interfaces, up to 217% enhancement compared with plainwall microchannels. As shown in Figure 4.22a, the liquid flow is evenly distributed along walls as a result superhydrophility of nanostructures thus it will locally rewet the unsaturated area, where has capillary forces.

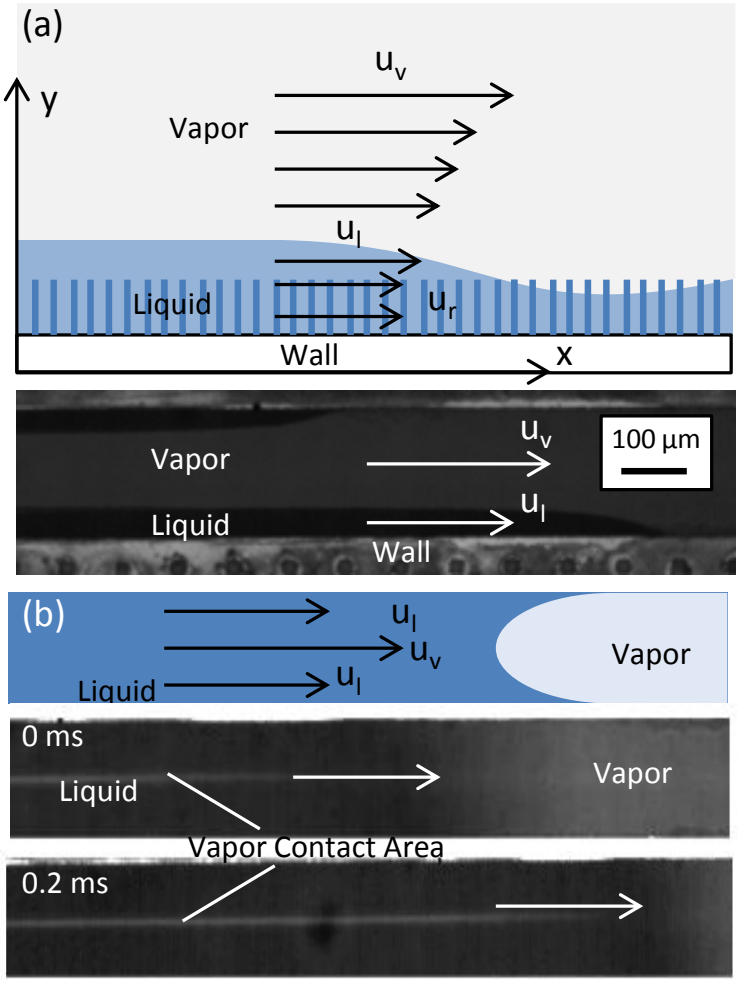

Figure 4.22. Improved liquid supply by the capillary flows induced on SiNWed walls in microchannels. (a) Local rewetting along SiNWed walls. (b) Global rewetting through the microchannel. Thin liquid film was still observed prior to CHF condition.

The surface tension force F_s drives rewetting flow with velocity u_r inside nanostructures. Above saturated nanostructures, an external liquid flow with velocity u_l could be then driven by shear stress. The third flow is the vapor flow with velocity u_v. It is also worth

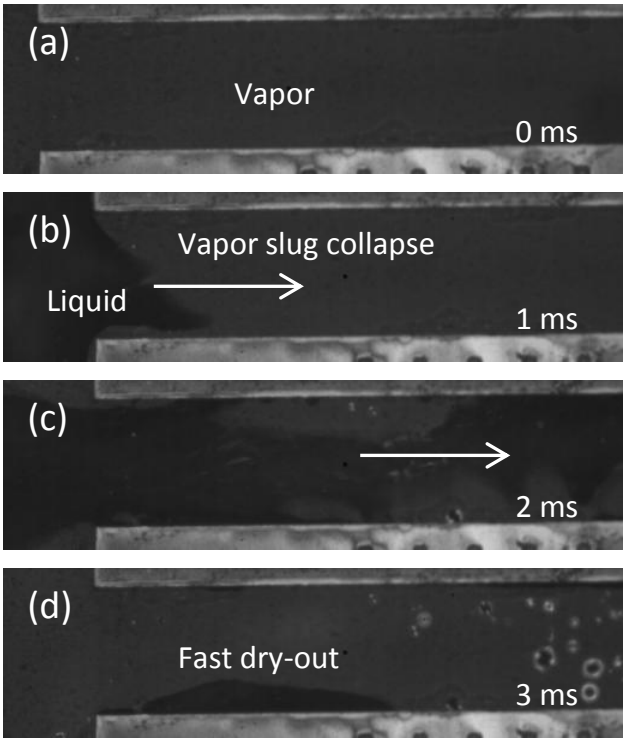

Figure 4.23. Fluid structure near CHF conditions in the SiNWed microchannels. Images are shot by a high-speed camera at 1000 frames per second. Working condition: q''_{eff} = 150 W/cm^2, $\dot{m}$ = 90 kg/m^2·s. (a) Liquid film was not visualized and microchannel could be filled with vapor. (b) The vapor slug partially collapsed. (c) Microchannel cannot be fully rewetted. (d) Continuous liquid film was broken. Expanding dried walls led to an escalation of wall temperatures.

mentioning another global wetting mechanism shown in Figure 4.22b. Vapor core collapse within a short time and the liquid flow fast rewets whole channel. It indicates the hydrodynamic instabilities of elongated vapor slug thru the whole microchannel may help

the rewetting and enhance CHF. As shown in Figure 4.12, this collapse process usually follows the capillary flow. It implies that the capillary flow may trigger the collapse the vapor core by creating hydraulic waves along walls of microchannels.

When these rewetting actions stop, the CHF would be reached in microchannels. The two-phase flow above CHF conditions is visualized in Figure 4.23. It shows the vapor slug would not totally collapse as shown in Fig. 9b. Figure 10a shows that the whole channel is quickly dry-out during high heat flux 150 W/cm^2 for a low mass flux 90 $kg/m^2 \cdot s$. During CHF conditions, it only partially collapses so that rewetting liquid cannot reach the whole channel as shown in Figure 4.23b and Figure 4.23c. It would be fast evaporated and dried out at the entrance of microchannels. The continuous capillary flow cannot be observed in this situation. As shown in Figure 4.23d, only small area was wetted by liquid flow. Then the vapor slug is stably established inside microchannel, Liquid may randomly and partially flow into superheated microchannels, but a stable mode of liquid supply cannot be rebuilt. Therefore, the microchannels reach CHF condition.

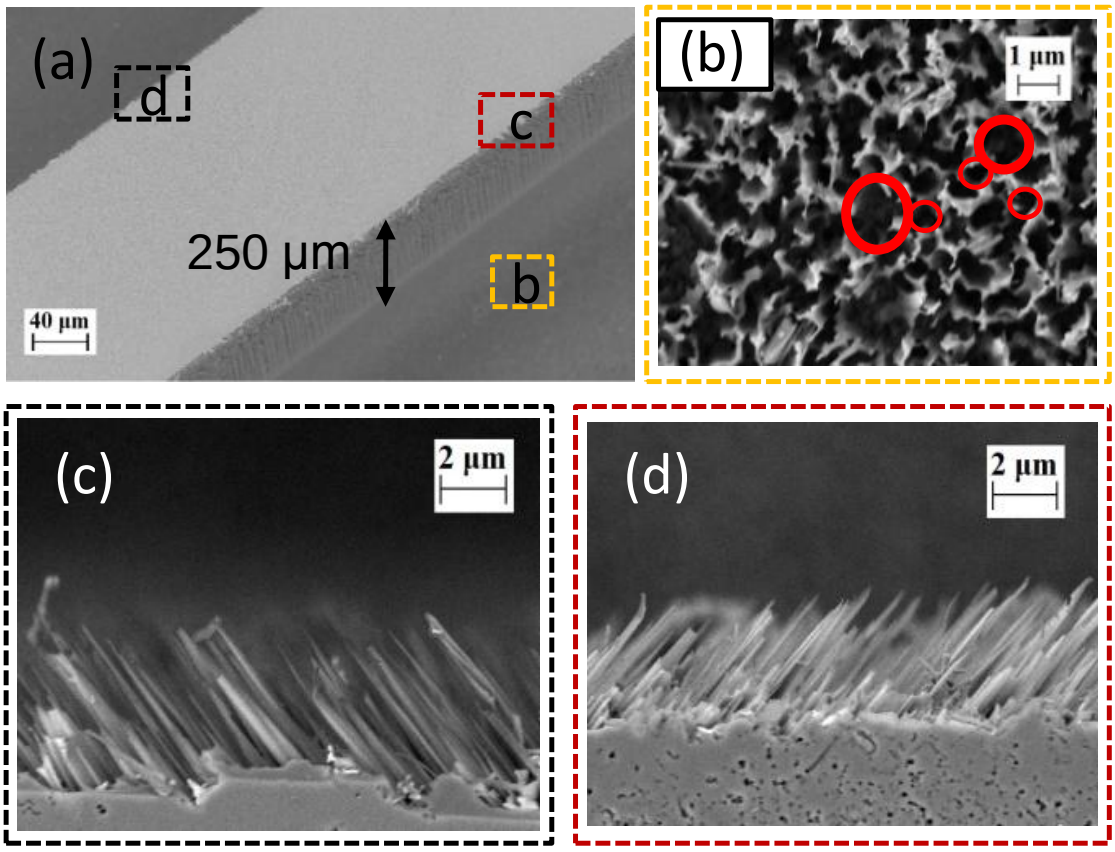

Figure 4.24. Boiling surfaces synthesized from hydrophilic SiNWs on inner walls of a microchannel. (a) The tilted-view scanning electron microscope (SEM) image shows the coverage of SiNWs in a rectangle microchannel (width, depth, length: 200 µm x 250 µm x 10 mm). (b) Top-view SEM image of SiNWs on the bottom surface. Typical microscale pores are highlighted. (c) and (d) SEM images of SiNWs on top edge of the vertical walls. Because of the crystal orientation, the SiNWs on two side walls have an approximately 45˚ tilt angle and those on the bottom surface are nearly vertical as shown in (b), (c) and (d). SiNWs are approximately 5 µm high.

The classic two-phase flow regimes are transitional. Four principle flow regimes including bubbly flow, slug flow, churn flow and annular flow are almost universally accepted and carry some unique traits at the micro scale.(Serizawa, Feng et al. 2002;Harirchian and Garimella 2011) The two-phase flow structures in microchannels are primarily governed by bubble confinements, liquid and vapor interactions, and forces

such as surface tension force and drag force. In this experimental study, we demonstrated that these three important factors can be controlled by tailored superhydrophilic silicon nanowires (SiNWs), which are approximately 20 nm in diameter and 5 μm long as shown in Figure 4.24. The SiNWs boiling surfaces were designed with the aim of producing small-sized bubbles and transferring the direction of dominant surface tension force(Raven and Marmottant 2006;Kandlikar 2010;Rabaud 2011) from the cross-sectional plane to the inner-wall plane. As a result, a mechanism to regulate bubble nucleation, separation, and two-phase flow regimes was formulated. The classic two-phase flow regimes can be reduced to a single two-phase flow regime termed "periodic annular flow". The single and periodic annular flow, which radically prevents two-phase flow regime transitions, was experimentally demonstrated to be self-stabilized. Compared to boiling with transitional flow regimes,(Harirchian and Garimella 2011) CHFs under the single periodic annular flow were enhanced approximately 300 % with mass fluxes ranging from 113 to 389 $kg/m^2 \cdot s$. Such dramatic enhancements should be primarily resulted from the unified flow boiling regimes. The highly stable flow boiling phenomena with high CHFs are desirable for high heat flux energy and thermal management systems.(Bergles and Kandlikar 2005) Equally important, rigorous generation of high-density micro- and sub-microscale vapor bubbles (i.e., nanobubbles) with extremely high surface area to volume ratio ($\sim 10^6$ m^{-1}) will enable emerging nanotechnologies in environmental science(Wu, Chen et al. 2008;Agarwal, Ng et al. 2011) and biotechnology. (Hernot and Klibanov 2008;Lukianova-Hleb, Hu et al. 2010)

In this study, flow boiling was studied in a microchannel array consisting of five parallel channels (length, width, and depth: 10 mm, 200 μm, and 250 μm). Except for the

top surface of microchannels, which was covered by Pyrex glass for visualization, SiNWs were directly grown on all inner walls (a). The SiNWs (Peng, Yan et al. 2002) were oxidized to achieve superhydrophilicity (approximately 0˚ contact angle) using the Wenzel effect.(Kuo and Gau 2010) Guided by the Hsu's model(Hsu 1962) and previous work,(Li, Wang et al. 2008) the optimal range of nucleation cavity size on the superhydrophilic boiling surfaces (by assuming contact angles between 0.1˚ and 1˚) was estimated from approximately 100 to 2000 nm.(Hsu 1962) The boiling surfaces with optimal submicron pores (formed by NW bundles) surrounded by nanogaps (created by individual NWs) were then synthesized from SiNWs by controlling the height and density of SiNWs (Figure 4.24c and Figure 4.24d) using the nanocarpet effect (Figure 4.24b).(Fan, Dyer et al. 2004) The average diameter of pores was measured at 466 nm from SEM images.

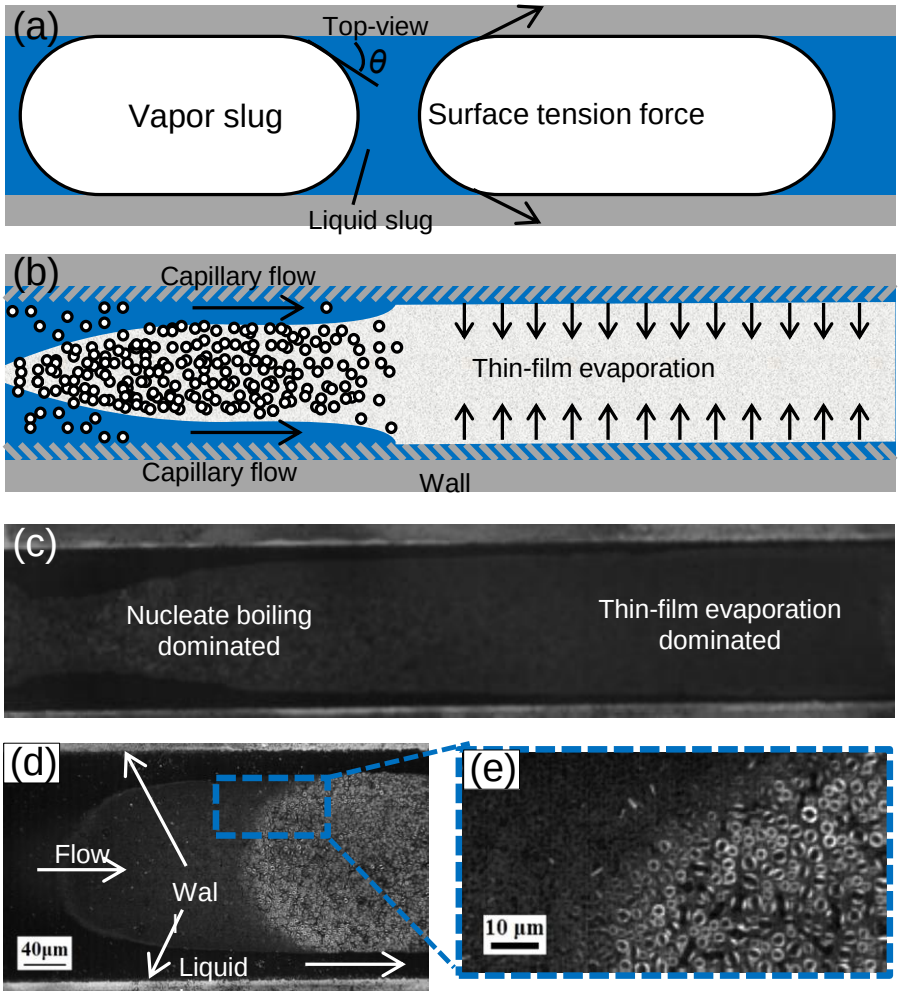

Figure 4.25. Comparisons of fluid structures in a microchannel with smooth inner-walls and SiNWed inner-walls. (a) The schematic of the fluid structure in slug flow in a microchannel with smooth walls. (b) The schematic of the fluid structures in a single and periodic annular flow in a microchannel with SiNWed walls. This figure was reduced from the optical image in (c). (c) The optical image of the fluid structures in a single and periodic annular flow. (d) A close-look of nucleate boiling. (e) The sub-microscale bubbles in an amplified optical image. The image was taken at an effective heat flux of 100 W/cm^2 and a mass flux of 213 kg/m^2 s. Arrows indicate flow directions. Blue, white and grey colors denote liquid, vapor and solid, respectively.

Near the inlet area, where was dominated by nucleate boiling, the diameters of vapor bubbles were significantly reduced to be less than 5 μm (termed as nanobubbles or NBs in short). The rapid large bubble growth in microchannels(Kuo and Peles 2008) was

effectively suppressed by generation vapor NBs. As illustrated in Figure 4.25c, d and e, vapor NBs near the inlet area were well-dispersed with extremely high density (e.g., more than 1.4×10^7 bubbles per cm^2 at a heat flux of 100 W/cm^2) and high surface area to volume ratio ($\sim 6\times10^6$ m^{-1}) as shown in Figure 4.25d and e.The smallest observable bubble was approximately 700 nm diameter (Figure 4.25d and e).

As aforementioned, the two-phase fluid structures in microchannels are primarily governed by bubble confinements, liquid and vapor interactions, and forces such as surface tension force and drag force. By reducing bubble size and preventing bubble from coalescence, the bubble confinements in the upstream of microchannels were effectively managed and hence, the interactions between bubbles and fluids were altered. First, the bubble size can be reduced by decreasing cavity size and minimizing the anchoring surface tension force. When bubbles are smaller than approximately 5 μm (Figure 4.25e), the buoyancy force are insignificant.(Zimmerman, Tesař et al. 2011) As a result, the bubble separation process (i.e., bubble departure) would be primarily governed by the anchoring surface tension force (Jiang, Osada et al. 2013),

$$F_s = 2\pi R_c \sigma \sin\theta \tag{62}$$

And the lifting inertial force, F_m, and the drag force (Van Helden, Van Der Geld et al. 1995;Thorncroft and Klausner 2001;Jiang, Osada et al. 2013),

$$F_d = \rho_l V^2 C_D \pi R^2 / 2 \tag{63}$$

where R is the bubble radius, R_c is the cavity opening radius, V is the bulk fluid velocity, θ is the static contact angle, σ is the surface tension, ρ_l is the liquid density, and C_D is the drag coefficient(Al-Hayes and Winterton 1981;Thorncroft and Klausner 2001). Imposed by F_m and F_d, which was estimated approximately one order of magnitude higher than F_s,

the bubbles could be swiped off from their nucleation cavities at small sizes. Second, as previous study(Wang and Cheng 2009) suggested, micro bubbles could be broken up into smaller bubbles by contacting with subcooled liquid. In this study, flow boiling experiments were conducted with a subcooling degree of approximately 40 K. It is possible that small bubbles could be prevented from coalescing into large bubbles during a subcooled flow boiling near the inlet area. In a saturated condition in the downstream, these small bubbles eventually coalesced to form a vapor core in each microchannel (Figure 4.25b and c).

In this study, the flow patterns were no longer dominated by the surface tension force at the cross-sectional direction. The capillary pressure,

$$p_c = 2\sigma \cos\theta / R_c \tag{64}$$

,which induced by the superhydrophilic SiNWs in the inner-wall plane is approximately 10^5 Pa, which is at least two orders of magnitude larger than that generated in the cross-sectional plane of a microchannel

$$p_c = 4\sigma \cos\theta / D_h \tag{65}$$

(i.e., approximately 600 Pa), where D_h is the hydraulic diameter of the microchannel. Thus, the direction of dominant forces was transformed from the cross-sectional plane (Figure 4.25a) to the inner-wall plane (Figure 4.25b) in two-phase flow systems by hydrophilic SiNWs.(Li, Wang et al. 2008;Chen, Lu et al. 2009;Liu, Li et al. 2011) As a result, the liquid slugs would be sucked into SiNWs and disappeared as evinced in Figure 4.25 and Figure 4.26, which eventually leads to a full separation of liquid and vapor flows and the formation of annular flows (Figure 4.25b, Figure 4.25c and Figure 4.26a). The capillary force also introduced strong local capillary liquid flows along the inner

solid walls, and the high frequency rewetting processes ranged from 23.3 to 53.7 Hz (Figure 4.26b). Additionally, the high Weber number of vapor flow in microchannel, *We*, was estimated at a magnitude of 10, which indicated a strong shear stress effect.

The overall characteristic of two-phase flow is annular and single in microchannels with SiNWs, which is radically different from the traditional multiple flow boiling regimes including the annular flow in existing studies(Serizawa, Feng et al. 2002;Thome 2004;Raven and Marmottant 2006;Marmottant and Raven 2009;Choi, Yu et al. 2011) since the vapor core grows and shrinks in a periodic manner. In this study, the maximum Reynolds number, Re, of vapor flows was less than 2300. The periodic behaviors were observed during entire laminar range of flow boiling from onset of nucleate boiling (ONB) to the critical heat flux (CHF) condition.

The major characteristics of the single and periodic annular flow during flow boiling in microchannels enabled by superhydrophilic SiNWs were summarized in Figure 4.26 Initially, vapor core occupied the center of the channel in a periodic annular flow. The contact area between the vapor core and the glass cover was small as observed at top view (0 ms in Figure 4.26a). Nucleation boiling and thin film evaporation dominate the upstream and downstream of the microchannel, respectively, as shown in Figure 4.25b and c, because of the vapor quality increasing in the flow direction.

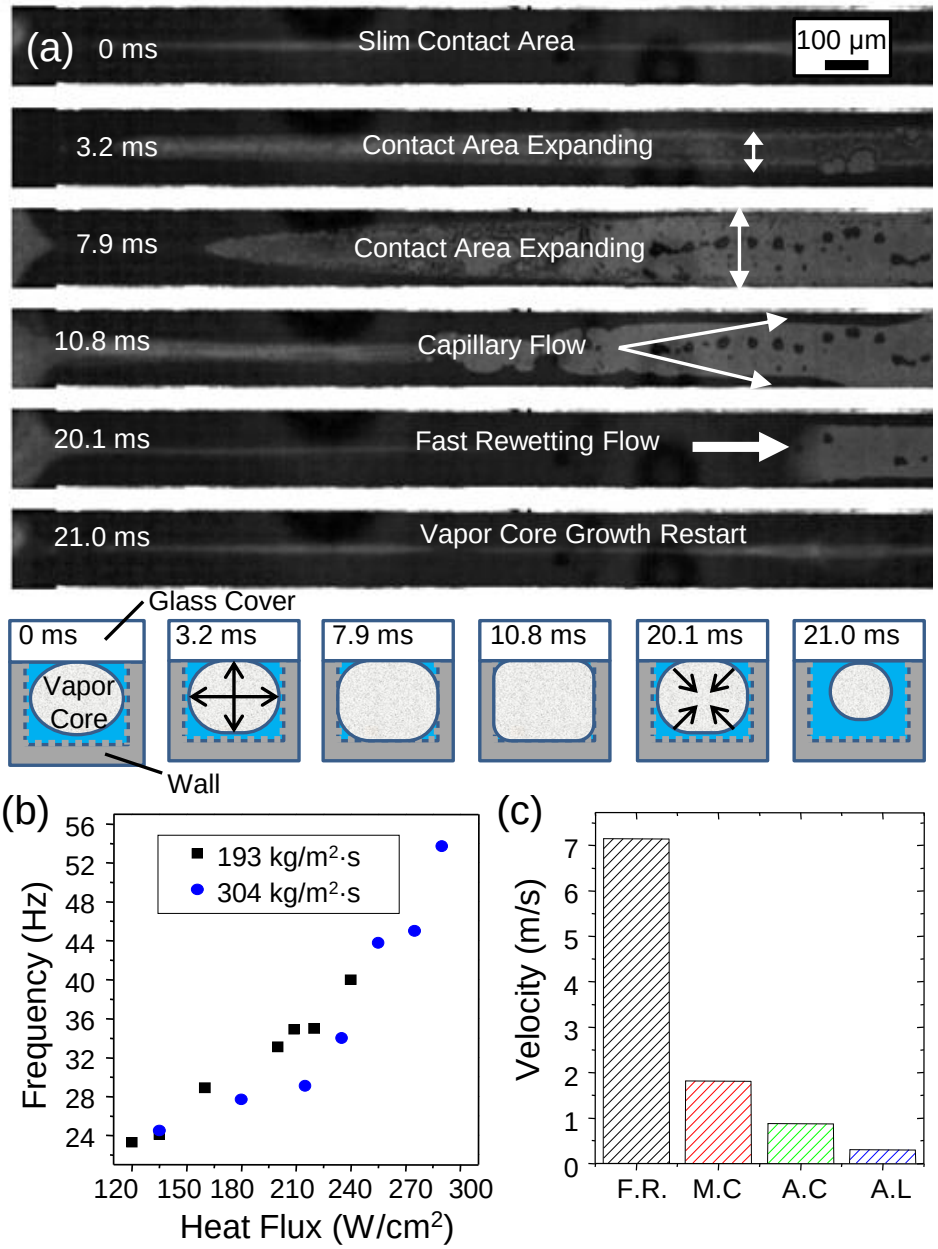

Figure 4.26. Characteristics of the single and periodic annular flow during flow boiling in microchannels with superhydrophilic SiNWs in a typical cycle. All images were taken from the top-view. (a) A whole period of single and periodic annular flow in a microchannel during convective boiling. Schematic cross-sectional figures at middle of microchannels were added to illustrate changes of a vapor shape and size. These images were captured under the working conditions: G = 193 kg/m^2 s, χ = 0.4. The white/gray areas denote vapor/bubbles and black/dark areas stand for liquid or droplets. (b) Rewetting frequency as a function of input heat fluxes and . (c) Typical velocities during rewetting process. F.R., M.C.,

A.C., and A.L. stand for the velocities of Fast Rewetting, Maximum Capillery, Average Capillery, and Average Liquid flow at inlet, respectively (enhanced online).

The vapor core rapidly grew because of the efficient phase-change heat transfer and eventually approached the SiNWs on the walls (from 0 ms to 7.9 ms in Figure 4.26a). As a result, the unsaturated superhydrophilic SiNWs (i.e., partially dryout) (Figure 4.24c) in the downstream instantly activated subcooled capillary flows at an average velocity of 0.73 m/s (Fig. 3c) along walls (at t=10.8 ms in Fig. 3a). Additionally, as shown in Figure 4.26c, both of the average and maximum velocities are substantially larger than the average bulk liquid velocity at the inlet (i.e., 0.304 m/s), which well evidenced the existence of the SiNWs induced capillary flows on inner walls. More importantly, because of the direct condensation at the vapor/subcooled liquid, the vapor core would then shrink and lead to fast rewetting flows (from 20.1 ms to 21 ms) as shown in Figure 4.26a, which should be primarily driven by the imposed pressure drop on microchannels. The rewetting flows flushed the vapor out of microchannels at a speed of 6.5 m/s as measured (Figure 4.26c). The rewetting frequency strongly depends on input heat fluxes and mass fluxes (Figure 4.26b), which implies the intensified evaporation/boiling would induce a faster growing vapor core and then a faster rewetting. The flow pattern then repeated at a distinct frequency. Reverse vapor flows near the inlet manifold of microchannels were observed. However, the liquid supply was not interrupted or even retarded because of the strong capillary flows on inner walls.

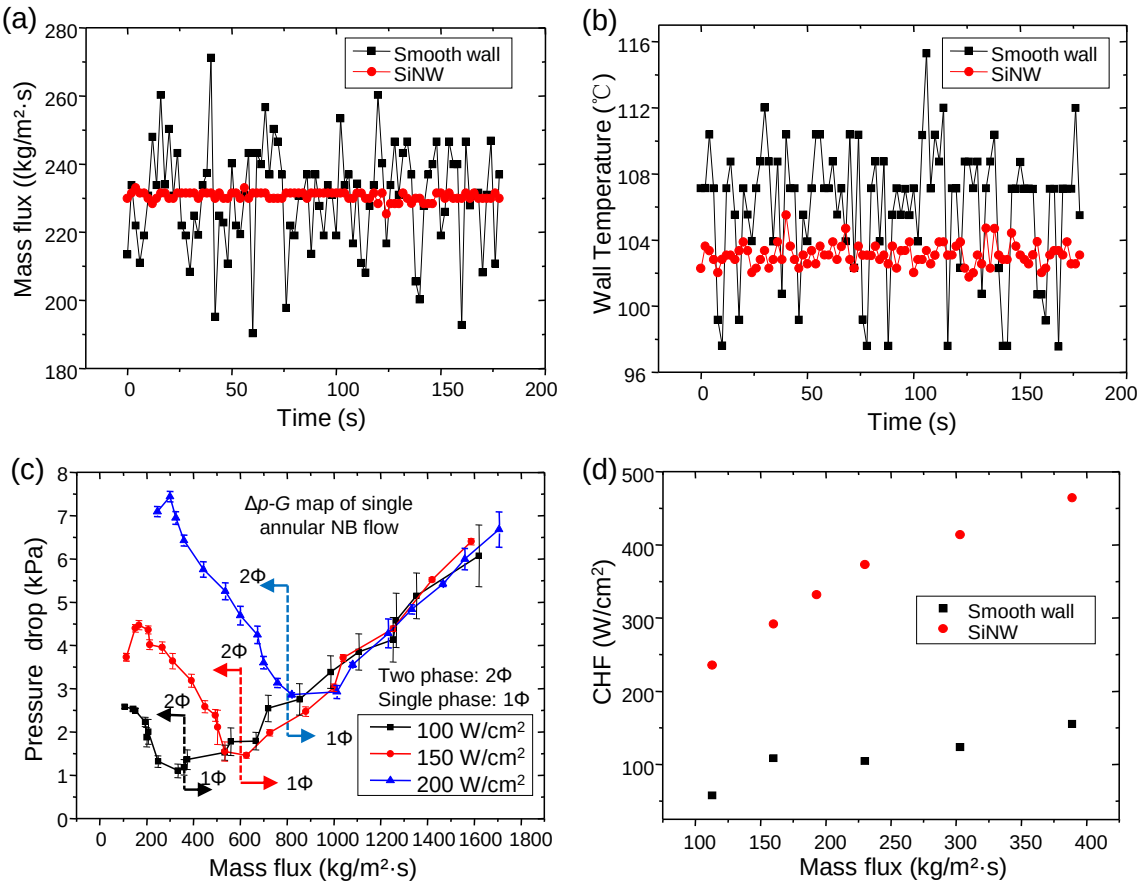

Figure 4.27. Comparisons of flow boiling instabilities and CHF in microchannels with smooth walls and SiNWed walls. (a) and (b) Transient mass fluxes and wall temperatures in a period of 180 seconds at a representative working condition: q"= 140 W/cm^2, G = 230 kg/m^2 s and q"= 53 W/cm^2, G = 113 kg/m^2 s, respectively. (c) Pressure drops (Δp) versus mass flux (G) curves at constant heat fluxes. Statistical analysis indicates effectively suppressed flow instabilities during the periodic annular flow. (d) Dramatically enhanced CHF in a single and periodic annular flow boiling regime.

In the traditional microchannel configurations, the unpredictable flow regime transitions can cause severe flow boiling instabilities and as a result, suppress evaporation and advection(Bergles and Kandlikar 2005;Raven and Marmottant 2006;Wang, Cheng et al. 2008;Zhang, Tong et al. 2009). As illustrated in Figure 4.27a and b, flow boiling in the single and periodic annular flow was self-stabilized in terms of mass flow rate (fluctuations less than 1%) and wall temperature (fluctuation less than 2%) by radically

removing the flow regime transitions. The Δp-G maps (pressure drop versus mass flux) were still "N"-shaped (Figure 4.27c), however, the static and dynamic instabilities occurred in traditional flow boiling(Bergles and Kandlikar 2005;Zhang, Tong et al. 2009) were radically suppressed by effectively managing the bubble confinement, separating liquid and vapor flows, and transforming the directions of surface tension force. The standard deviation (SDs represented as the error bars in Figure 4.27c) was also used to quantify flow boiling instabilities by examining the fluctuation of the system pressure drop. The results in Figure 4.27c show that the fluctuations of pressure drop in the single and periodic annular flow regime were substantially reduced compared to those in smooth microchannels.(Zhang, Tong et al. 2009;Liu, Li et al. 2011) As a result, CHF was enhanced approximately 300% comparing with plain-wall microchannels with mass fluxes ranging from 113 to 389 $kg/m^2 \cdot s$ (Figure 4.27d).

In all, a single and periodic annular flow regime during flow boiling in microchannels, which is self-stabilized and effective in enhancing CHF by radically removing the flow boiling regime transitions, was experimentally demonstrated in the laminar flow. The mechanisms behind the formation of this single and periodic annular flow regime were discussed. This study indicates the feasibility to control two-phase flow regimes and hence, two-phase transport at micro/nanoscale. The intrinsic merits of a single and periodic annular flow regime should be highly desired in areas pertinent to two-phase transport at micro/nano-scale.

4.5 SUMMARY

In conclusion, the flow boiling in microchannels with SiNWed inner walls was dramatically enhanced compared to smooth-wall microchannels with and without IRs or

orifices. The flow boiling in the single and periodic annular flow was also systematically characterized. The major heat transfer modes in the new flow boiling regime including nucleate boiling, thin film evaporation and advections were identified; and the associated enhancement mechanisms were discussed. The enhanced nucleate boiling is primarily resulted from the high active nucleation site density and the high bubble departure frequency that were enabled by the engineered SiNW boiling surfaces. The rapid capillary flows or rewetting induced by the superhydrophilic SiNWs plays critical roles in promoting thin film evaporation and advections over the whole microchannels during the entire flow boiling process. Visualization study was performed to improve the understanding of heat transfer and two-phase flows in the single and periodic annular flow. Theoretical study was conducted to qualitatively understand bubble dynamics, which was consistent with experimental observations.

In this experimental study, superhydrophilic nanostructures are coated onto inner surface of microchannel so that a single annular flow is formed during flow boiling inside microchannels. The thermal-hydraulic characteristics of this annular flow are studied. It gives following statements. These nano-engineered interfaces separate vapor and liquid due to surface tension forces in nano-scale or submicron scale cavities. The superhydraulicity of these nanostructures enhanced the adhesion forces so that the entrained droplets are much less than smooth channel.

Experimental study demonstrated this optimized flow structure could reduce frictional pressure drop during two-phase flow boiling even the roughness of solid surface is significantly increased. Experimental data in this study shows that pressure drop is reduced up to ~50%, comparing to smooth-wall samples. This characteristic

would save pumping power and improve energy economics of many chemical processing systems, energy systems and thermal management systems.

Two models of ideal annular flow and two-phase mixture flow are utilized to explain the mechanism of friction reduction in this letter. To reduce frictional pressure drop of annular flow, our results indicate that the two-phase separation is more critical factor than roughness. A better two-phase separation would lead to a lower frictional pressure drop.

Induced by surface tension forces, capillary flows along microchannels would rewet dry-out area and enhance CHF. According to our observation, the capillary flow may induce the collapse the vapor slug through the microchannel. During CHF condition, stable vapor slug is created with reduced capillary flow. Both capillary effects and hydrodynamic instabilities shall be considered for investigating the CHF mechanism of single annular flow.

Moreover, this interface material could be synthesis on complex 3D structures and integrated into many silicon microsystems, which include but not limited to multiphase microchemical systems, micro energy generator and micro cooling system for high-performance electronics. The cavity opening size and porosity is variable by controlling the duration of catalyst deposition and etching.

CHAPTER 5

NANO-TIPS INDUCED BOUNDARY LAYERS IN MICROCHANNELS

Flow boiling has great potentials in cooling high power electronic and photonic components. However, the device performance is often thermally limited to the critical heat fluxes of current cooling technologies. Flow boiling in miniaturized channels is hampered by several severe constraints such as bubble confinements (Bar-Cohen, Sheehan et al. 2012), viscosity and surface tension force-dominated flows (Kandlikar 2010), which result in unpredictable flow pattern transitions (Serizawa, Feng et al. 2002;Rahim, Revellin et al. 2011) and tend to induce severe two-phase flow instabilities and suppress evaporation and convection. This, in turn, is detrimental to flow boiling heat transfer. As discussed in previous chapters, critical heat fluxes are also dominated by flow instability issues. As a result, two-phase flow boiling in microchannels have not been accepted as a practical approach for real-world electronics cooling (Bar-Cohen and Geisler 2011).

In microchannels, surface tension and laminar flow dominates microchannels rather than other factors. Thus, the existing of large vapor slugs, whose diameter are larger than the hydraulic diameter of microchannels, become a critical issue. Due to the existing of large vapor slugs, the flow patterns transition occurs during unstable flow boiling. The transient flow pattern in microchannels is either vapor slug flow or sub-cooled liquid flow. For certain pressure drop between point c and e in Figure 1.2, the mass flux is oscillating around steady point at low frequency (0.01 to 1 Hz)

(Wu and Cheng 2004;Zhang, Tong et al. 2009). While vapor slug is expanding inside microchannels, liquid may be impeded to rewet dry-out area. Then local temperature would rise rapidly. Then, premature CHF, which is much smaller than actual capability of a microscale flow boiling system, would be induced by Ledinegg instability. Not to mention this instability may interlink with compressible volume instability and rapid bubble growth instability and further reduce mass and heat transfer efficiency. To overcome this problem, a constant displacement pump header and throttle were used to force the inlet flow into microchannels (Bergles and Kandlikar 2005). And the most effective existing solution is adding an inlet orifice (Kosar, Kuo et al. 2006;Wang, Cheng et al. 2008) at the entrance of each single channel in a microchannel array. Previous studies reveal that the inlet orifice did reshape the pressure-drop-mass-flux curve, separate flows and hinder the reverse flow (Kosar, Kuo et al. 2006;Wang, Cheng et al. 2008). Thus, CHFs are significantly enhanced by inlet orifices. Nevertheless, inlet orifices would increase pressure drop two magnitudes more than without them. Much higher pump power and more sophisticated flow-driven mechanism are necessary for previous solutions to suppress these instabilities. They increase the total cost and reduce the reliability of a microscale flow boiling system, therefore, make it hardly practical in real-world applications. Thus, flow instabilities shall be suppressed within microchannels without using inlet orifices.

It is necessary to consider a effective mechanism to suppress flow instabilities. To find an alternative method for suppressing flow instabilities with fewer drawbacks, there are several critical tasks. First, large vapor slugs, which grow, combine in reverse flow and hinder the incoming rewetting liquid, shall be collapsed when dry-out is lasting and

the CHF is reaching. It is necessary to develop a method for controlling the growth and collapse of bubble inside microchannels. Although there is lack of analytical method to precisely predict the collapse criterion of a growing thermal bubble in sub-cooled flow, bubble collapse shall be caused by increased shear stress on bubble wall as a result of violent bubble motion and inner pressure increasing (Legendre, Boree et al. 1998;Bogoyavlenskiy 1999). Secondly, an efficient rewetting method is necessary to supply liquid for flow boiling and thin-film evaporation inside microchannels. Finally, there are diversified and transitional flow patterns in microchannels: bubbly flow, vapor slug flow, churning flow and annular flow. The annular flow shall dominate the flow boiling in microchannels (Bergles and Kandlikar 2005), however the existing of meniscus may leads to long-lasting vapor slug in reverse flow so that large-amplitude oscillations of pressure drop or mass fluxes exist during flow boiling in microchannels (Wu and Cheng 2003;Wu and Cheng 2004;Bergles and Kandlikar 2005). By breaking vapor slugs in a short time, annular flow could be rebuilt at high frequency and thin-film evaporation could be sustained inside microchannels.

Thermal boundary layer on walls of microchannel are considered to be re-designed for controlling bubble dynamics and suppress the flow instabilities. Because heat and mass transfer are ultimately governed by boundary layers (BLs) during flow boiling in microchannels. It was also experimentally demonstrated in recent studies that flow boiling can be enhanced by disturbing BLs through creating oscillations (Yang, Dai et al. 2012;Yang, Dai et al. 2013), introducing capillary flows along walls, and promoting thin film evaporation (Li, Wu et al. 2012;Morshed, Yang et al. 2012). Laminar boundary layer dominates two-phase flow boiling in microchannels, especially, thin-film

evaporation, where the effects of viscosity are significant in liquid thin films. It is supposed that the boundary layer shall play an important role for bubble dynamics in microchannels. However, researches to enhance flow boiling in microchannels by intentionally constructing and optimizing *BLs* was not reported.

In all, a new functional boundary layer on inner walls of microchannels is used to meet above requirements and suppress flow instabilities as shown in Figure 2.3. First, this boundary layer shall be super-hydrophilic. This boundary layer should also work as wicking structures to induce a rewetting flow thru the inner wall of microchannels and rebuild liquid thin-film. Then, the liquid film could support the following thin-film evaporation so that combined vapor slugs grow even faster in reserve flow. It could sustain thin-film evaporation without fast dry-out. Finally, the fast motion of bubble walls may lead to a collapse of the vapor slug. This boundary layer should also change the direction of inner surface tension forces and re-distribute vapor and liquid inside microchannels. Therefore, an annular flow would be generated while flow instabilities could be suppressed.

5.1 EXPERIMENTAL PROCEDURES

The testing setup and data reduction refer to Section 4.2 in CHAPTER 4.

5.1.1 MICRO/NANOFABRICATION OF NANO-TIP INDUCED BOUNDARY LAYER.

Recent advanced technology on micro/nanofabrication helps us realize this concept. Patternable nanotip arrays have been fabricated and demonstrated (Chang Kun, Sang Min et al. 2008). This nanostructures are made by using deep reactive ion etching (DRIE). It could be a low-cost method because DRIE is an inexpensive technique, which is well-

deployed in current MEMS/microelectronics industries. Moreover, no nanoparticles or nanoscale lithography is involved into the fabrication process.

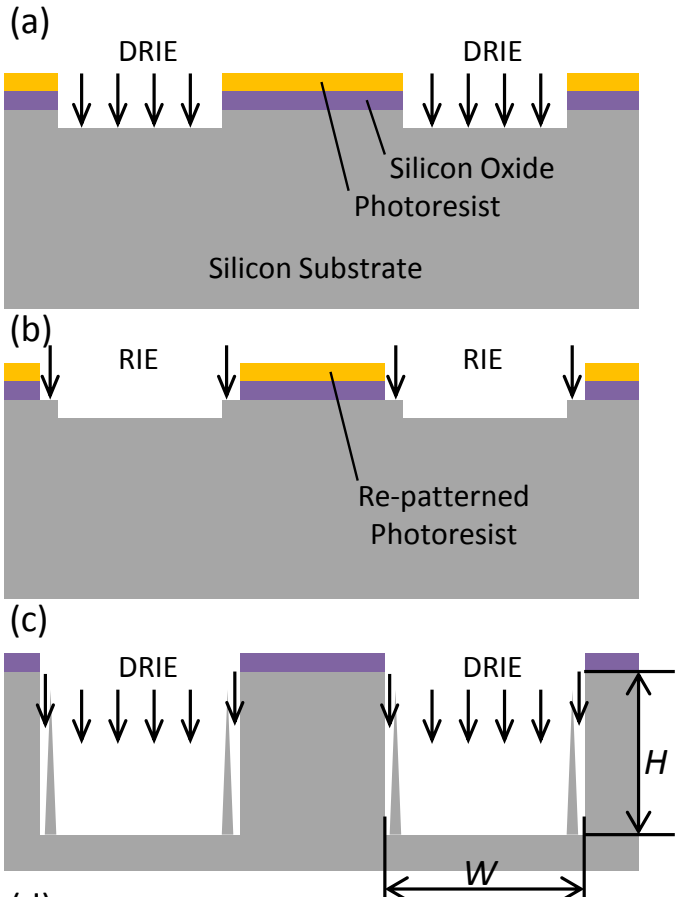

Figure 5.1. The Cross-sectional viewed fabrication process of patternable nanotips. (a) First step DRIE etch 50 μm depth trench. (b) The silicon oxide mask is re-patterned so that the mask is 5 μm wider than original trench. (c) Additional DRIE step etch 200 μm deeper and form the nanotip arrays along the side walls of microchannel. (d) the key dimensions of nanotip arrays.

The nanotip arrays are formed by Bosch process, which usually starts with a photo-masked and developed <100> silicon wafer. At the beginning, the C_4F_4 gas is provided to generate fluorocarbon as the polymeric passivation layer of the entire surface in microchannels. Consequently, SF_6 gas is used for isotropic etching. High power

induced coupled plasma (ICP) is applied to sputter away fluorocarbon layer on the horizontal bottom surfaces and etch silicon vertically. Therefore, as mentioned in many existing studies (Kuo-Shen, Ayon et al. 2002;Chang Kun, Sang Min et al. 2008), nanoscale scallops are formed on both sides of microchannels and the sidewalls are not exactly vertical. Furthermore, due to non-uniform electrical fields at the wafer-cool-grease interface deviating the ion flux laterally, tapered reentrant profiles were found on sidewalls (Pike, Karl et al. 2004;Lee, Jiang et al. 2007;Chang Kun, Sang Min et al. 2008). There are repeat prominences and depressions along the sidewalls. C. K. Kang, et al demonstrated a technique to generate nanotip arrays on planar surface or top surface of microstructures by reforming these reentrant sidewalls during second DRIE (Chang Kun, Sang Min et al. 2008). In this study, a multi-step DRIE method is developed to integrate these nanotip arrays on bottom surface inside microfluidic systems.

The existing method (Chang Kun, Sang Min et al. 2008) was modified so that nanotips could be formed inside microchannels. In this fabrication process, a pre-etched pattern would determine the distribution of nanotip arryas, which located on the edge of pre-etched trench (Figure 5.1a). Wrinkled curtain-shape sculptures are formed at the lower part of side walls. Then, secondary patterning would remove oxide mask on the gaps between nanotip arrays and walls (Figure 5.1b). The second DRIE would etching the gap. However, the tops of the curtain-shape sculptures shall not be removed, then form into nanotips (Figure 5.1c). The width of gap is defined as W_g = 5 μm in our study.

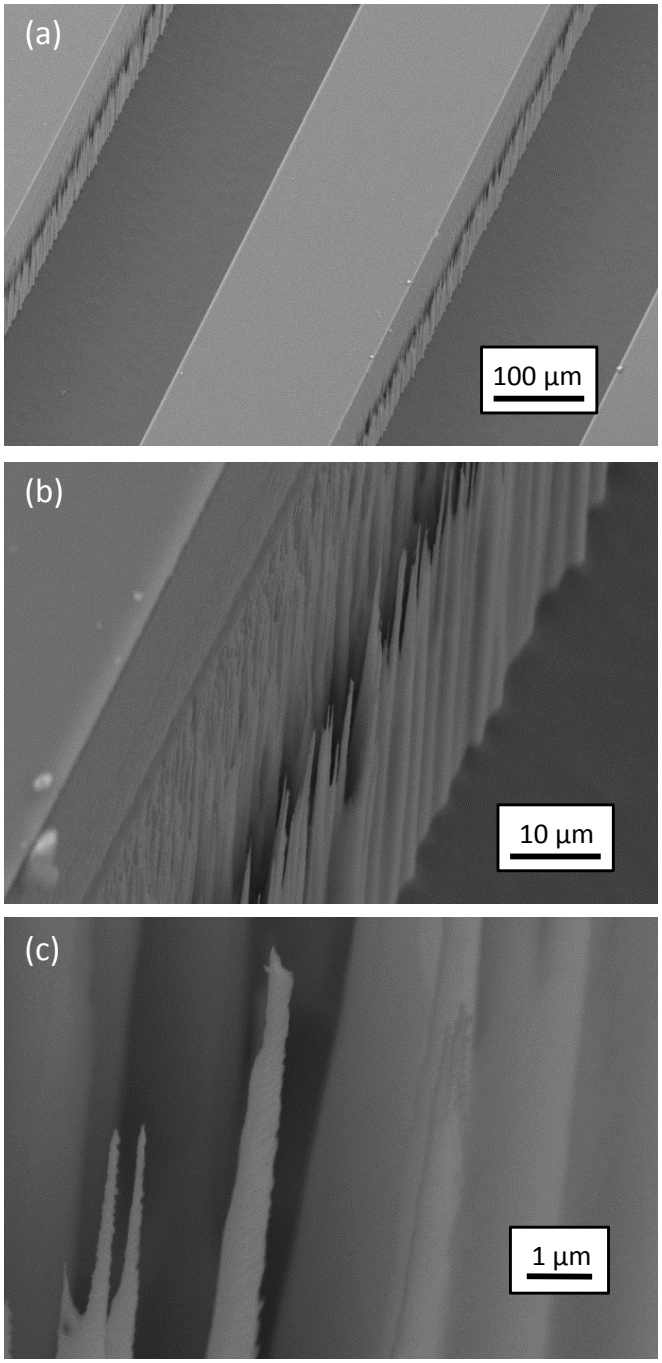

Figure 5.2. SEM figures of nanotips inside microchannels. (a) Microchannels. (b) Nanostructures close to side walls. (c) Nanotips.

And the height of nanotip arrays H_t is 200 μm. As shown in Figure 5.1, nanotip arrays are etched by DRIE and located close to the side walls of microchannels. Both parameters are controllable in fabrication process so that the distributions and heights of nanotips could be designed. Due to ease of the patternable-nanotip fabrication method, it is not necessary in fabrication process to use nanoscale lithography or nanoparticle, which are common in other technique (Dixit, Lin et al. 2008;Li, Wu et al. 2012;Morshed, Yang et al. 2012). The SEM figures are shown in Figure 5.2. And there are 5 microchannels (220 μm W, 250 μm H, 10 mm L) in a testing chip.

On the backside, microfabrication process similar to Section 4.2 forms a micro heater and micro thermistors. Therefore, uniform heat flux would be provided at an area of 0.2 cm^2 on the backside of microchannel arrays. In the same time, the average temperature on this heating area during flow boiling would be monitored by the micro thermistors.

5.2 RESULTS AND DISCUSSION

An experimental study was performed on flow boiling in Si microchannels consisting of five parallel channels (length, width, and depth: 10 mm, 200 μm, and 250 μm) with Si nanotips induced BL. For comparisons, a parallel microchannel array with identical channel dimensions was tested.

5.2.1 NANO-TIPS INDUCED WETTABILITY

During flow boiling, a high speed camera was used to observe wettability and liquid distribution on side walls during flow boiling inside microchannels (Figure 5.3a). While vapor slugs growing inside microchannels, the transient contact angle on side wall of microchannels is directly top-viewed and shown in Figure 5.3. According to Figure 5.3b, the contact angle of plain-wall silicon surface is about 60 degrees, which means the DRIE etched wall is partially wetted during flow boiling. On the contrary, high surface tension force is paralleled to the nanotips induced boundary between solid and vapor. It makes the nanotip arrays super-hydrophilicity. The curtain-shape microstructures (Chang Kun, Sang Min et al. 2008) and nanoscale scallop on nanotips as shown in Figure 5.2c may contribute to the super-hydrophilicity. This property of nanotip array shall be important for microfluidics and heat transfer in microchannel. The capillary force within these nanostructures may take the domination of viscosity in thermal boundary layer by introducing a liquid thin film between nanotip array and walls, which may also modify the bubble dynamics during thin-film evaporation inside an elongated vapor slug.

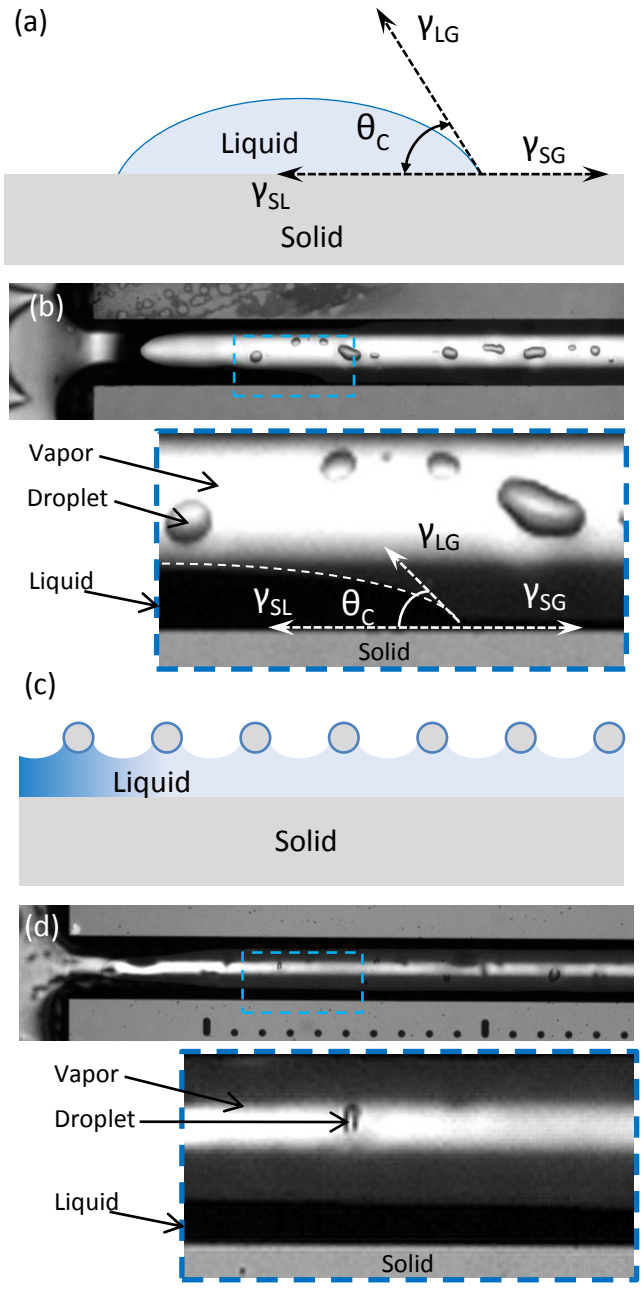

Figure 5.3. The wettability of side-wall solid boundary is determined by the contact angle. The top-viewed high speed photography reveal the wettabilty of (a) plain side-wall boundary and (b) nanotip induced boundary.

5.2.2 FLOW INSTABILITY

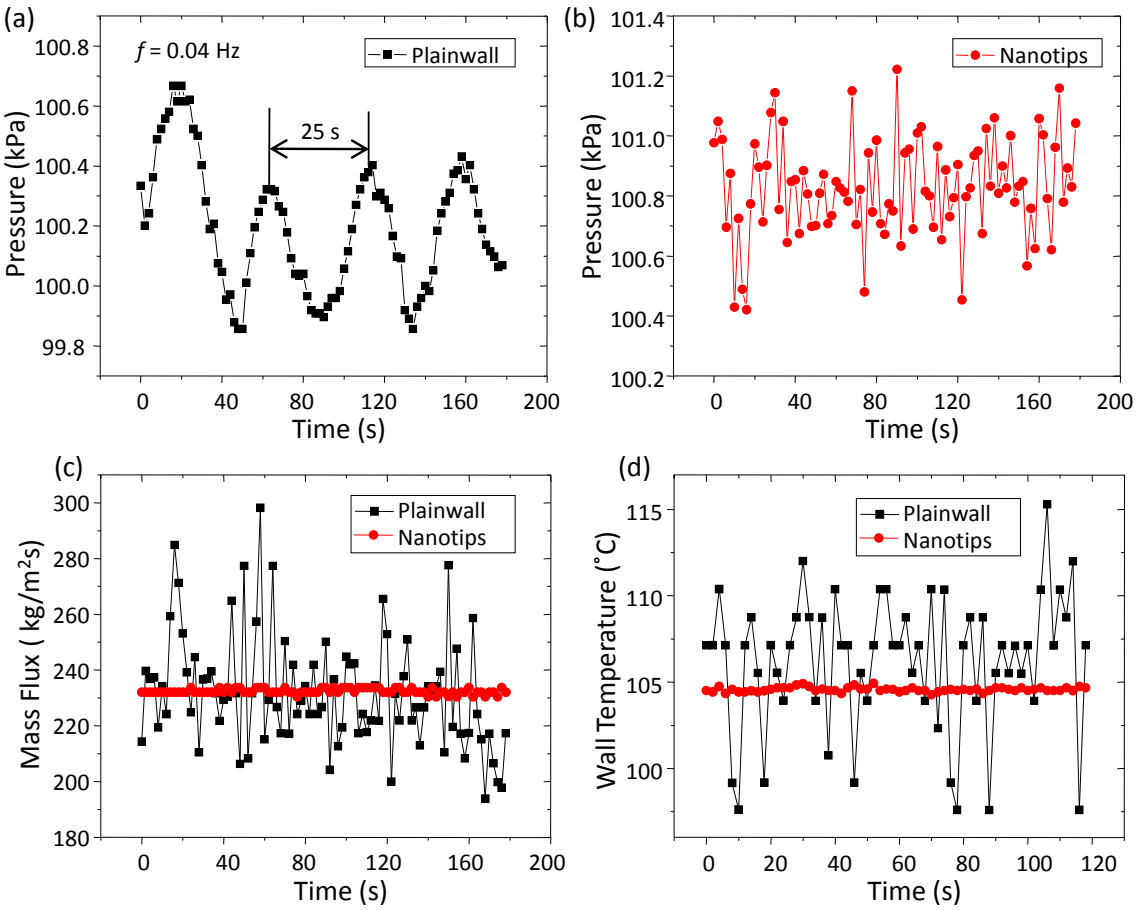

Figure 5.4. Stabilized flow boiling by nanotips induced *BL*. (a) Outlet pressure oscillation of flow boiling in plain-wall microchannels with mass flux 230 kg/m^{2}s and heat flux 125 W/cm^2. (b) Outlet pressure oscillation of flow boiling in microchannels with nanotips induced boundary layer with mass flux 230 kg/m^{2}s and heat flux 125 W/cm^2. (c) Oscillation of mass flux in microchannels with mass flux 230 kg/m^{2}s and heat flux 125 W/cm^2. (d) Oscillation of wall temperature in microchannels with mass flux 113 kg/m^{2}s and heat flux 53 W/cm^2.

The transient data of pressures, mass fluxes and temperature during flow boiling in microchannels were collected and shown in Figure 5.4. It indicates there is a low-frequency oscillation existing in plain-wall microchannels. This result matches previous study on plain-wall microchannel without enhanced structures (Wang, Cheng et al. 2007). The oscillation frequency is about 0.04 Hz for flow boiling in plain-wall microchannels.

In Figure 5.4b, due to the application of nanotips induced boundary layer, the oscillation amplitude is significantly reduced under the same sampling rate (0.5 Hz). It also implies that the oscillation frequencies of Figure 5.4b are much higher than Figure 5.4a. It may be induced by fast collapse of vapor slugs during fast bubble wall motions.

Then, Figure 5.4c and d shows that the flow instabilities were successfully suppressed. In plain-wall microchannels, the oscillations of mass flux are ~32% of average values and the oscillations of temperature are ~19% of average values. By applying nanotips induced boundary layer, both mass fluxes and average temperatures were stabilized to less than 0.5% of average values comparing to large amplitude oscillations of mass fluxes and temperatures in plain-wall microchannels.

5.2.3 PRESSURE DROP

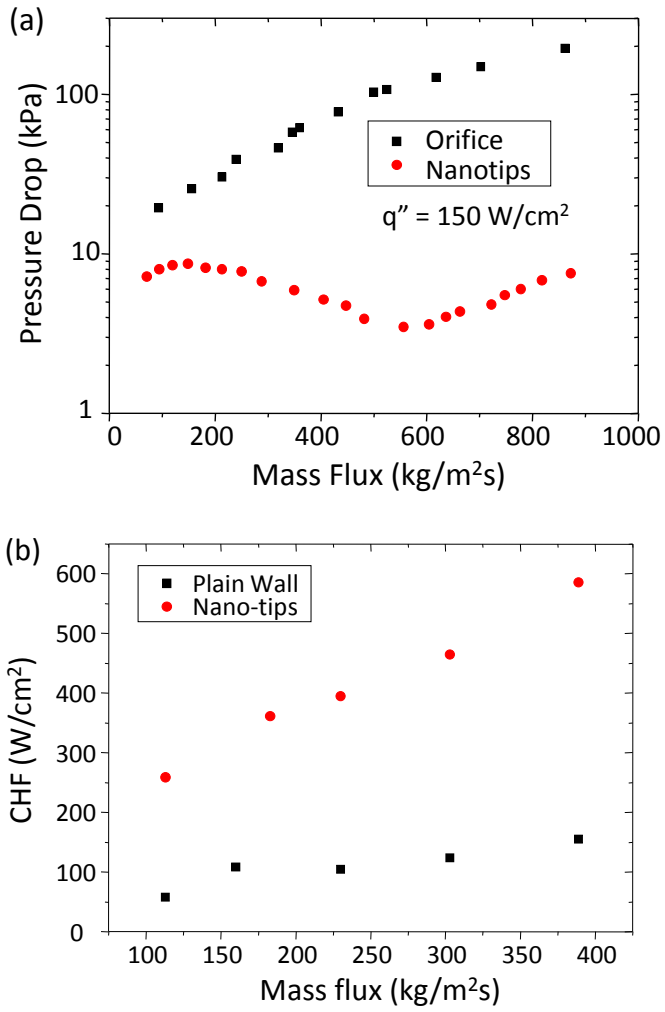

Figure 5.5. (a) A Δp-G map of flow boiling in microchannels with inlet orifice and nanotips is shown. (c) Enhancements of CHF as a function of mass flux. They have identical dimensions of microchannels but different enhancement method.

A comparison of pressure drops between microchannels with inlet orifices and nanotips is shown in Figure 5.5a. Although inlet orifice has the same capability for suppressing flow instabilities like nanotips (Figure 5.5b), it induces much higher pressure

drop than current results. Thus, current technique could suppress the flow instabilities without sacrificing pumping power.

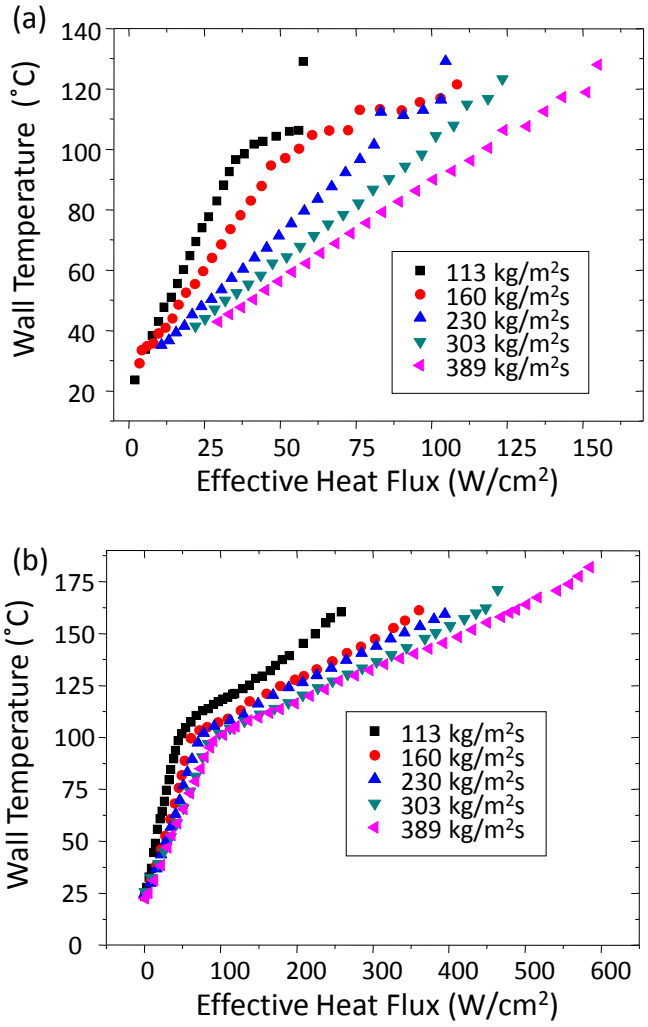

Figure 5.6. Flow boiling curves of plain-wall (a) microchannels and (b) microchannels with nanotips induced boundary layer..

5.2.4CRITICAL HEAT FLUX

Once flow instabilities are effectively suppressed, the CHF shall be largely improved as shown in Figure 5.5b. Flow boiling in microchannels are tested and shown in Figure 5.6. As shown in Figure 5.6a, the premature CHF leads to reduced heat transfer efficiency during the beginning stage of flow boiling and this result has been

demonstrated by many previous studies (Bergles and Kandlikar 2005;Kuo and Peles 2008). As a valid method, the nanotips induced boundary layer suppresses flow instabilities. In current study, CHF was enhanced up to ~585 W/cm^2 at a moderate mass flux of 389 kg/m ²s on deionized (DI) water (Figure 5.6b). Compared to flow boiling in plain-wall microchannels, CHF was enhanced between 332 % and 448 % with mass flux varying from 113 to 383 kg/m^{2}s.

5.2.5 HEAT TRANSFER EFFICIENCY

The nanotips inside microchannel not only suppress flow instabilities but also enhance heat transfer. Because flow boiling performance of plain-wall microchannels is not comparable to current concept, microchannel with inlet orifice is used to estimate the heat transfer enhancement of current concept. As shown in Figure 5.7, the wall temperatures of microchannels with nanotip arrays are significantly lower than the microchannels with orifices. The experiments are carried through two different mass fluxes. Data in Figure 5.7 shows up to 50% percent enhancement of heat transfer.

The enhancement of flow boiling heat transfer could be induced by two major mechanisms: enhanced nucleation boiling and enhanced thin-film evaporation. The first mechanism usually plays an important role at the initial stage of flow boiling because high potential nucleation sites reduced required superheats for bubble nucleations (Kosar, Kuo et al. 2005). There are many potential nucleation sites as cavities between nanotips and walls (Figure 5.2), however, plain-wall microchannels are lack of similar potential nucleation cavities (Kuo, Kosar et al. 2006). Once the vapor slug and annular flow was established in microchannels, the first mechanism may dominate heat transfer any more. In this situation, the second mechanism shall be the major reason of enhanced heat

transfer. The nanotip arrays could generate new thermal boundary layers and enhance thin-film evaporation as shown in Figure 5.3. Detailed mechanism will discussed with visualization studies in following sections.

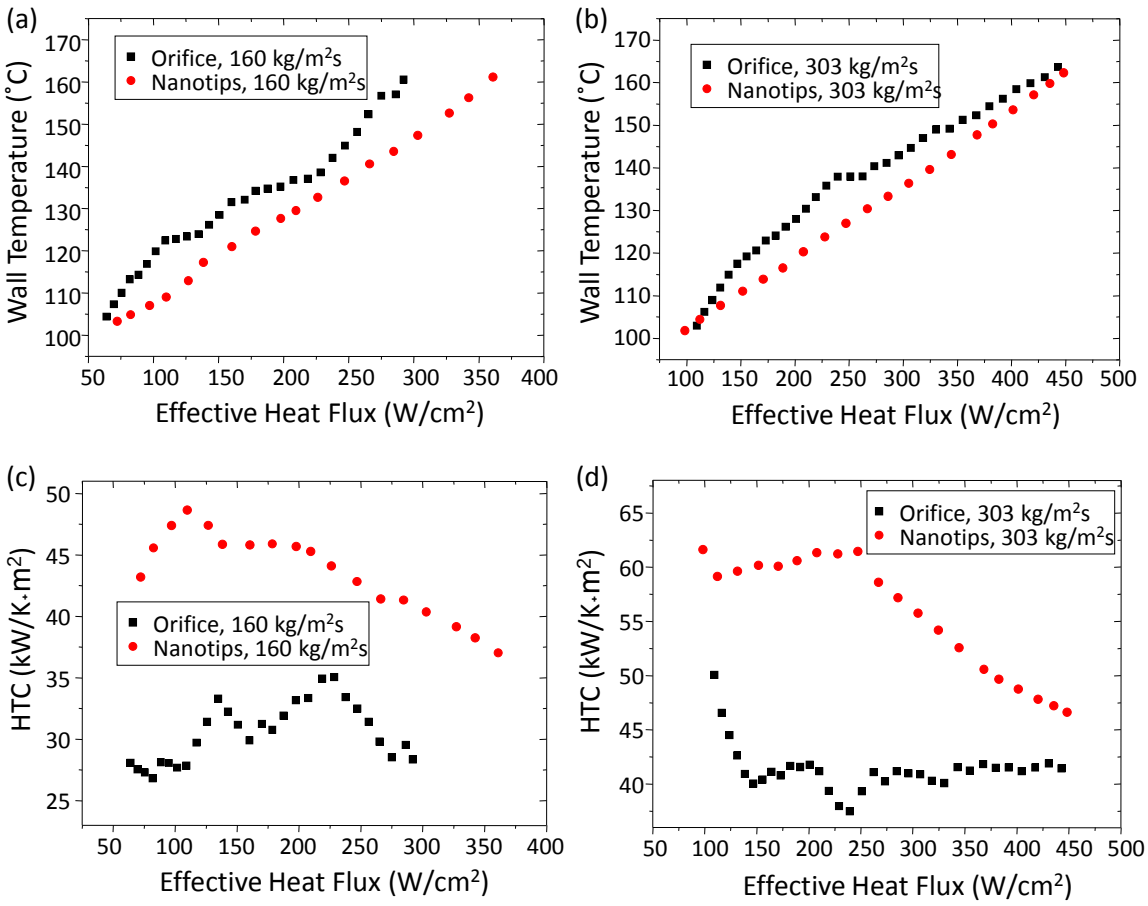

Figure 5.7. Comparing the heat transfer efficiency of flow boiling in nanotip enhanced microchannels with inlet restricted microchannels. (a) and (b) are average wall temperature during flow boiling. (c) and (d) are heat transfer coefficient.

5.3 MECHANISM

In this study, the mechanism of CHF and heat transfer is investigated. As discussed in previous studies, combined large vapor slugs in reserve flow shall lead to difficulty in rewetting microchannels (Bergles and Kandlikar 2005). Also, the transition between flow patterns is caused by fast vapor slug growth (Zhang, Tong et al. 2009). Once the inlet manifold and microchannels are filled with vapor bubles, the thin-film evaporation and boiling would be hindered then the system reach premature CHF.

As we discussed in this chapter, the fast motion of bubble wall and quickly increased internal pressure may collapse vapor slugs. Existing studies modeled the criterion of a gas bubble collapse in liquids (Bogoyavlenskiy 1999;Lugli and Zerbetto 2007;Tsiglifis and Pelekasis 2007) and suggest the increased internal pressure (Tsiglifis and Pelekasis 2007) and increased tension of bubble wall caused by fast boundary oscillation (Bogoyavlenskiy 1999) would collapse a suspended gas bubble. However, the condensation and evaporation at the thermal bubble boundary has more complicated conditions than a gas bubble. K. S. Das et al shows there could be a waiting time while one end of vapor slug is superheated and the other side is supercooled (Das and Wilson 2010). It is the similar case of flow boiling in plain-wall channel when vapor slug is growing in sub-cooled liquid. His study implies the endurance of the vapor slug in traiditional channel. However, previous study doesn't indicate how to shorten this waiting time and it doesn't consider the drag force of supercooled liquid flow. D. Legendre et al modeled and calculated the thermal and dynamic evolution of a spherical bubble in a subcooled liquid (Legendre, Boree et al. 1998). They give the collapse time of a thermal bubble by numerical modeling. However, the criterion of collapse has not been discussed.

Generally, there are few previous researches on collapse of microscale confined thermal vapor slug in subcooled flow. Furthermore, few techniques are reported to collapse elongated vapor slugs in microchannesl and enhanced flow boiling.

Recent studies (Li, Wu et al. 2012;Morshed, Yang et al. 2012) have been used superhydrophilic nanostructures to enhance mass and heat transfer of flow boiling in microchannels. However, existing studies only apply the nanostructures at the bottom of microchannels and few mass and heat transportation phenomena (capillary flow and thin-film evaporation) on nanostructured solid boundaries has been directly observed and reported. Also, the direction of surface tension forces inside microchannels in previous studies is totally different from current concept. As we discussed in above sections, the surface tension dominates several modes of flow instabilities as a result of bubble confinements in microchannels. Thus, CHF is still limited by flow instabilities in previous studies.

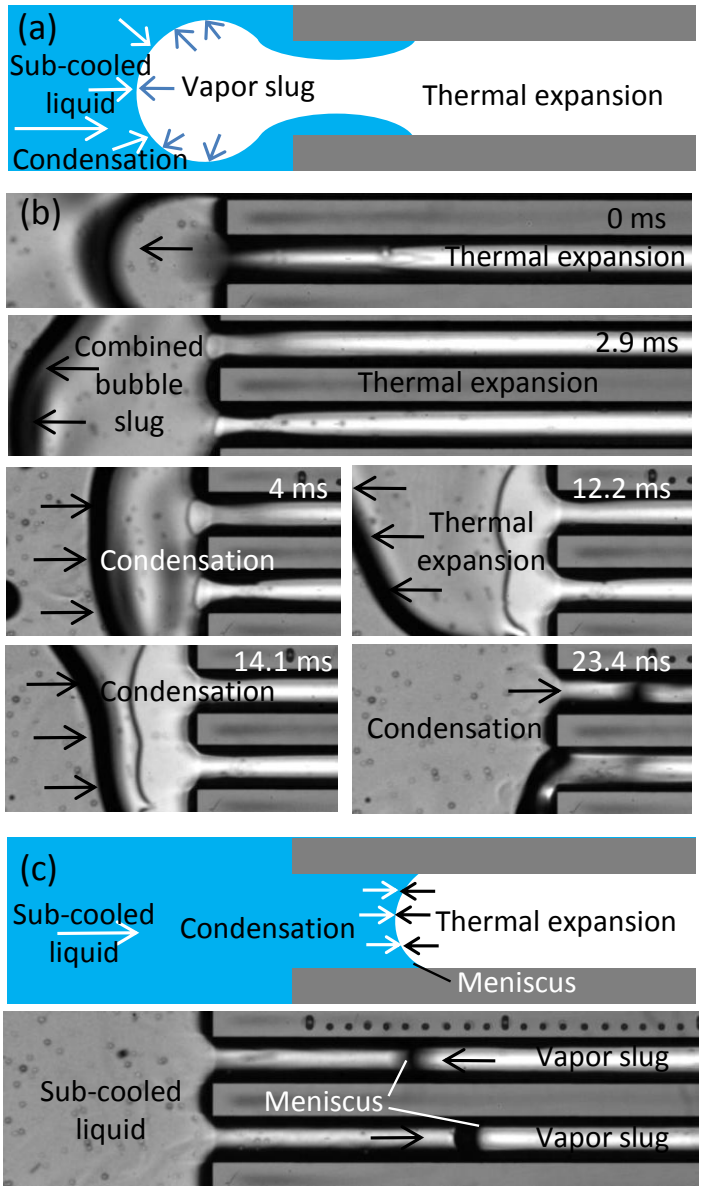

Figure 5.8. Analysis of flow pattern in plain-wall microchannels. (a) Schematic map of vapor slug growth in reverse flow. (b) The motion of bubble of combined vapor slug in reverse flow. (c) The existing of meniscu and elongated vapor slugs inside microchannels.

In this dissertation, the bubble behaviors in traditional microchannels are schematically shown in Figure 5.8. Without the induced boundary layer, the bubble growth rate is primarily determined by the thermal expansion and it should be limited by

the temperature and pressure inside vapor slug (Figure 5.8a). The superheated bubble may result in low condensation rate on the bubble wall hence bubble expanding and shrinking process (also known as flow boiling instabilities) were recorded at low frequencies as shown in Figure 5.8b. Inside the microchannel, the surface tension force generated in the cross-sectional direction (Figure 5.8c) of a microchannel formed meniscus and prevents incoming flow supplying liquid onto the inner wall around vapor slugs and causes pre-mature CHF conditions. (Kim, Rainey et al. 2002;Wu and Cheng 2003;Wu and Cheng 2004;Kandlikar, Kuan et al. 2006;Kosar, Kuo et al. 2006;Kuo and Peles 2008;Chen and Garimella 2011)

On the contrary, the established BL will fundamentally alter the bubble dynamics during flow boiling in microchannels. For instance, the elongated bubble will grow rapidly as a result of thin film evaporation on the induced BL (Figure 5.9a). Consequently, the fast growth of a bubble would lead to direct contact and significantly enhanced condensation heat transfer at the subcooled liquid and vapor interface and hence, a rapid collapse of a vapor slug (Figure 5.9b). The rapid and periodic growth and collapse of a vapor slug in micrcochannles will lead to high frequency liquid flush inside microchannels during flow boiling. Such a highly dynamic fluid motion induced by nanotips is highly desirable and was not achieved before. The high frequency oscillations can drastically enhance the global and local liquid supply and introduce advections. The existence of the induced BL, i.e., a moving liquid film (because of the surface tension force and shearing stress imposed by vapor flows), can reduce the transitional flow regimes into a new regime similar with annular flow by separating liquid and vapor flows.

In our study, we first ever demonstrated the existing of capillary flow along solid boundary by inducing nanotips. H. Wang, S.V. Garimella et al studied and modeled the characteristics of an evaporating thin film in a plain-wall microchannel (Wang, Garimella et al. 2007). In their study, an adsorbed or non-evaporating region is defined between the heated walls and a vapor slug. Thin-film evaporation only occurs at the intrinsic-meniscus region, which is significantly smaller than non-evaporating region inside a microchannel. However, as shown in Figure 5.9b and c, nanotips activate the non-evaporating region then extend the evaporating region so that thin-film evaporation occurs in most internal boundary between solid walls and a vapor slug.

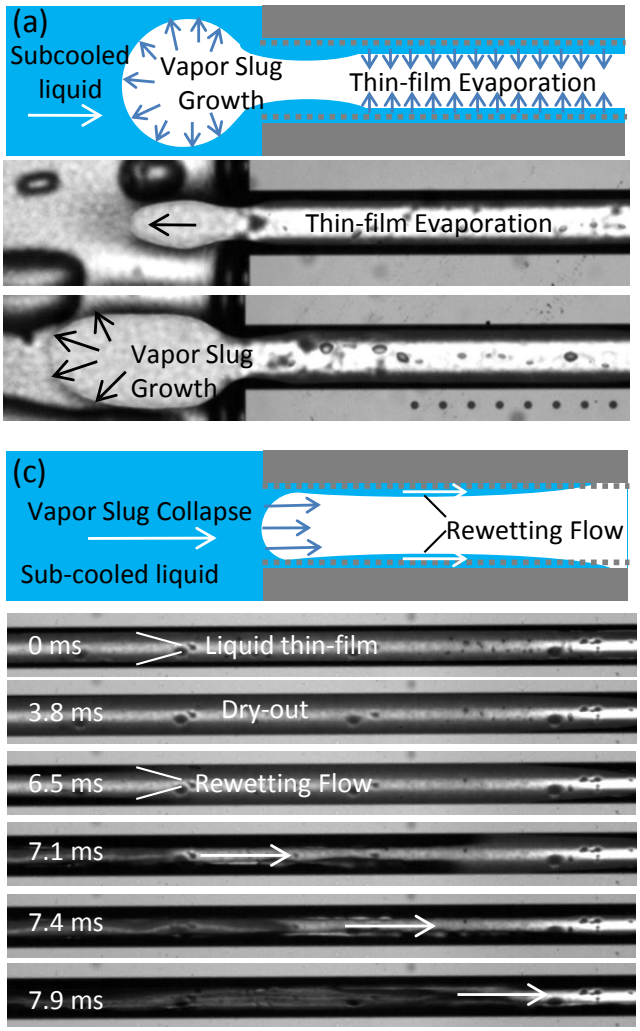

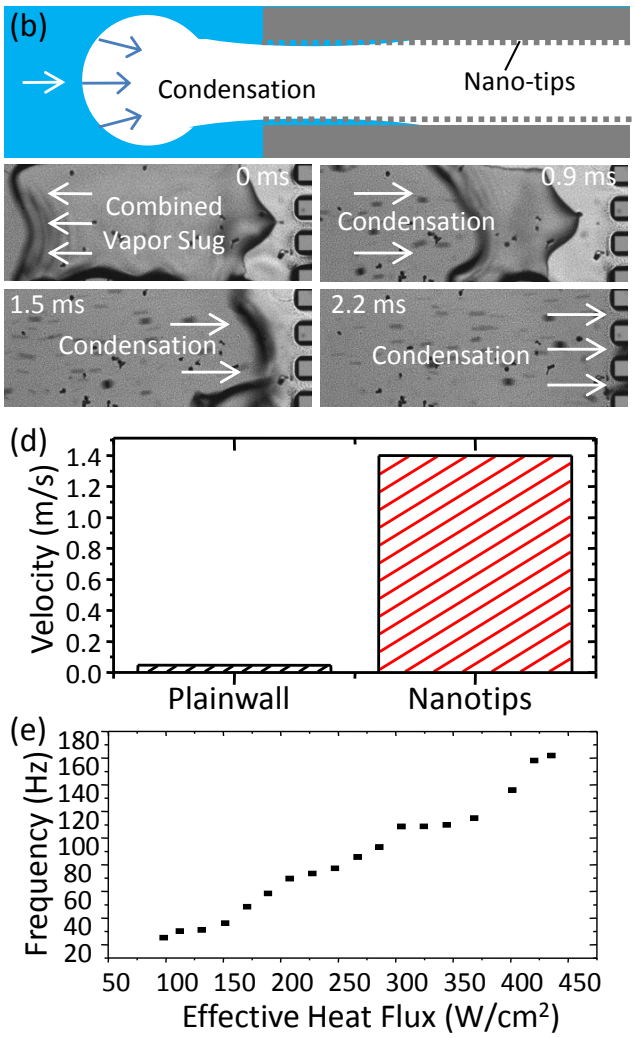

Figure 5.9. Analysis of flow pattern in microchannels with nanotips induced boundary layer. (a) Vapor slug growth in reverse flow. (b) Vapor slug collapse and fast condensation in inlet sub-cooled liquid flow. (c) Fast rewetting inside microchannels formed by the new boundary layer. (d) Comparing the average water-front velocity during bubble growth and collapse process in reverse flow. (e) The rewetting frequency in microchannels with nanotip induced boundary layer as a function of effective heat flux.

The impacts of nanotips induced BL were partially validated in microchannels. The averaged velocity of the liquid-vapor interface during bubble expansion was used to measure the bubble expansion rate by assuming a constant cross-sectional flow area. As illustrated in Figure 5.9d, the velocity in the microchannels with induced BL was approximately an order of magnitude higher that in microchannels with smooth walls.

The rapid rewetting induced by nanotips was also observed as illustrated in Figure 5.9e. The rewetting frequency was measured ranging from 35 Hz to 180 Hz and observed to increase with increasing working heat flux.

Due to nanotips induced boundary layer, the thin-film evaporation could last longer time than without it. The continuous phase change would greatly accelerate the steamwise advection flow inside vapor slugs and increase the internal pressure. Thus, mass and heat transfer in thin-film evaporation are significantly enhanced by nanotips inside microchannels.

5.4 SUMMARY

For the first time, by directly reconstructing the BL, it has been shown that the flow boiling in microchannels can be controlled and designed as desired to some extent. Compared with the partial and incremental enhancement of flow boiling in existing studies through the use of novel configurations, flow boiling in microchannels with nanotips induced BLs could be drastically enhanced by optimizing the heat transfer process and two-phase flows. As a result, CHF can be dramatically enhanced up to nearly 500% by creating new liquid supply mechanisms without using the IRs. The unpredictable two-phase flow patterns can be reduced to a new and single flow pattern enabling excellent controllability of the otherwise stochastic two-phase flow patterns/regimes. Such a dramatic enhancement in the flow boiling can lead to a breakthrough in the design of energy-efficient and cost-effective two-phase cooling systems to achieve direct cooling of next generation high power electronics, 3D microelectronics, and high power photonics. Equally important, this study enable new research directions in two-phase transport, and provide fresh fundamental insights

pertinent to boiling at the nano- and micro-domains. In addition, it will greatly advance current understanding of boiling at diminishing length scales

However, in current stage of study, the mechanism is still not well-understood without knowing the velocity profiles inside these novel thermal boundary layers. There is few technique to investigate two-phase flow in nanoscale. Molecule dynamics may help us reveal more details of these new phenomena. Moreover, heat transfer and CHF could be further enhanced by reforming and controlling boundary layer during flow boiling in microchannels.

REFERENCES

Abdelall, F. F., G. Hahn, S. M. Ghiaasiaan, S. I. Abdel-Khalik, S. S. Jeter, M. Yoda and D. L. Sadowski 2005. Pressure drop caused by abrupt flow area changes in small channels. *Experimental Thermal and Fluid Science* 29(4): 425-434.

Agarwal, A., W. J. Ng and Y. Liu 2011. Principle and applications of microbubble and nanobubble technology for water treatment. *Chemosphere* 84(9): 1175-1180.

Agostini, B., M. Fabbri, J. E. Park, L. Wojtan, J. R. Thome and B. Michel 2007. State of the art of high heat flux cooling technologies. *Heat Transfer Engineering* 28(4): 258-281.

Ahn, H. S., S. H. Kang, C. Lee, J. Kim and M. H. Kim 2012. The effect of liquid spreading due to micro-structures of flow boiling critical heat flux. *International Journal of Multiphase Flow* 43(0): 1-12.

Al-Hayes, R. A. M. and R. H. S. Winterton 1981. Bubble diameter on detachment in flowing liquids. *International Journal of Heat and Mass Transfer* 24(2): 223-230.

Andersson, H., W. van der Wijngaart, P. Nilsson, P. Enoksson and G. Stemme 2001. A valve-less diffuser micropump for microfluidic analytical systems. *Sensors and Actuators B-Chemical* 72(3): 259-265.

Aussillous, P. and D. Quere 2000. Quick deposition of a fluid on the wall of a tube. *Physics of Fluids* 12(10): 2367-2371.

Balasubramanian, P. and S. G. Kandlikar 2005. Experimental Study of Flow Patterns, Pressure Drop, and Flow Instabilities in Parallel Rectangular Minichannels. *Heat Transfer Engineering* 26(3): 20-27.

Bar-Cohen, A., M. Arik and M. Ohadi 2006. Direct liquid cooling of high flux micro and nano electronic components. *Proceedings of the Ieee* 94(8): 1549-1570.

Bar-Cohen, A. and K. J. L. Geisler (2011). Cooling the Electronic Brain. Mechanical Engineering**:** 38-41.

Bar-Cohen, A. and E. Rahim 2009. Modeling and Prediction of Two-Phase Microgap Channel Heat Transfer Characteristics. *Heat Transfer Engineering* 30(8): 601-625.

Bar-Cohen, A., J. Sheehan and E. Rahim 2012. Two-Phase Thermal Transport in Microgap Channels—Theory, Experimental Results, and Predictive Relations. *Microgravity Science and Technology* 24(1): 1-15.

Bergles, A. E. and S. G. Kandlikar 2005. On the nature of critical heat flux in microchannels. *Journal of Heat Transfer-Transactions of the Asme* 127(1): 101-107.

Bogoyavlenskiy, V. A. 1999. Differential criterion of a bubble collapse in viscous liquids. *Physical Review E* 60(1): 504-508.Bonaccurso, E., H. J. Butt and V. S. J. Craig 2003. Surface roughness and hydrodynamic boundary slip of a newtonian fluid in a completely wetting system. *Physical Review Letters* 90(14).

Borkent, B. M., S. M. Dammer, H. Schönherr, G. J. Vancso and D. Lohse 2007. Superstability of surface nanobubbles. *Physical Review Letters* 98(20): 204502.Boure, J. A., A. E. Bergles and L. S. Tong 1973. Review of two-phase flow instability. *Nuclear Engineering and Design* 25(2): 165-192.

Cao, H. Z., H. B. Xu, N. Liang and C. Q. Tian 2011. Experiment investigation of R134a flow boiling process in microchannel with cavitation structure. *Heat Transfer Engineering* 32(7-8): 542-553.

Cavallini, A., D. Del Col, M. Matkovic and L. Rossetto 2009. Frictional pressure drop during vapour–liquid flow in minichannels: Modelling and experimental evaluation. *International Journal of Heat and Fluid Flow* 30(1): 131-139.

Chandrasekaran, S. and S. Sundararajan 2004. Effect of microfabrication processes on surface roughness parameters of silicon surfaces. *Surface and Coatings Technology* 188–189(0): 581-587.

Chang, K. H. and C. Pan 2007. Two-phase flow instability for boiling in a microchannel heat sink. *International Journal of Heat and Mass Transfer* 50(11-12): 2078-2088.

Chang Kun, K., L. Sang Min, J. Im Deok, J. Phill Gu, H. Sung Jin and K. Jong Soo 2008. The fabrication of patternable silicon nanotips using deep reactive ion etching. *Journal of Micromechanics and Microengineering* 18(7): 075007.

Chen, P.-H., W.-C. Chen and S. H. Chang 1997. Bubble growth and ink ejection process of a thermal ink jet printhead. *International Journal of Mechanical Sciences* 39(6): 683-695.

Chen, R., M. C. Lu, V. Srinivasan, Z. Wang, H. H. Cho and A. Majumdar 2009. Nanowires for enhanced boiling heat transfer. *Nano Letters* 9(2): 548-553.

Chen, T. and S. V. Garimella 2011. Local heat transfer distribution and effect of instabilities during flow boiling in a silicon microchannel heat sink. *International Journal of Heat and Mass Transfer* 54(15-16): 3179-3190.

Cheng, C. M. and C. H. Liu 2006. A capillary system with thermal-bubble-actuated 1 x N microfluidic switches via time-sequence power control for continuous liquid handling. *Journal of Microelectromechanical Systems* 15(2): 296-307.

Cheng, P., G. Wang and X. Quan 2009. Recent Work on Boiling and Condensation in Microchannels. *Journal of Heat Transfer* 131(4): 043211-043215.

Cheng, P., G. D. Wang and X. J. Quan 2009. Recent Work on Boiling and Condensation in Microchannels. *Journal of Heat Transfer-Transactions of the Asme* 131(4).

Cheng, P., H. Y. Wu and F. J. Hong 2007. Phase-change heat transfer in microsystems. *Journal of Heat Transfer-Transactions of the Asme* 129(2): 101-108.

Choi, C., D. I. Yu and M. Kim 2011. Surface wettability effect on flow pattern and pressure drop in adiabatic two-phase flows in rectangular microchannels with T-junction mixer. *Experimental Thermal and Fluid Science* 35(6): 1086-1096.

Choi, C. W., D. I. Yu and M. H. Kim 2010. Adiabatic two-phase flow in rectangular microchannels with different aspect ratios: Part II - bubble behaviors and pressure drop in single bubble. *International Journal of Heat and Mass Transfer* 53(23-24): 5242-5249.

Chun Ting, L. and P. Chin 2009. A highly stable microchannel heat sink for convective boiling. *Journal of Micromechanics and Microengineering* 19(5): 055013.

Dai, X., F. Yang, R. Fang, T. Yemame, J. A. Khan and C. Li 2013. Enhanced Single and Two-phase Transport Phenomena Using Flow Separation in a Microgap with Copper Woven Mesh Coatings. *Applied Thermal Engineering*(0).

Das, K. S. and S. K. Wilson 2010. Dynamics of a two-dimensional vapor bubble confined between superheated or subcooled parallel plates. *Physical Review E* 81(4): 046314.

Deng, P., Y.-K. Lee and P. Cheng 2003. The growth and collapse of a micro-bubble under pulse heating. *International Journal of Heat and Mass Transfer* 46(21): 4041-4050.

Dixit, P., N. Lin, J. Miao, W. K. Wong and T. K. Choon 2008. Silicon nanopillars based 3D stacked microchannel heat sinks concept for enhanced heat dissipation applications in MEMS packaging. *Sensors and Actuators A: Physical* 141(2): 685-694.

Egatz-Gomez, A., R. Majithia, C. Levert and K. E. Meissner 2012. Super-wetting, wafer-sized silicon nanowire surfaces with hierarchical roughness and low defects. *RSC Advances* 2(30): 11472-11480.

Fan, J. G., D. Dyer, G. Zhang and Y. P. Zhao 2004. Nanocarpet Effect: Pattern Formation during the Wetting of Vertically Aligned Nanorod Arrays. *Nano Letters* 4(11): 2133-2138.

Fanghao Yang, Xianming Dai, Chih-Jung Kuo, Yoav Peles, Jamil Khan and C. Li 2012. Enhanced flow boiling in Microchannels by High Frequency Microbubble-excited and -modulated Oscillations. *International Journal of Heat and Mass Transfer* In review.

Fogg, D. W. and K. E. Goodson 2009. Bubble-Induced Water Hammer and Cavitation in Microchannel Flow Boiling. *Journal of Heat Transfer-Transactions of the Asme* 131(12).

Fogg, D. W. and K. E. Goodson 2009. Bubble-Induced Water Hammer and Cavitation in Microchannel Flow Boiling. *Journal of Heat Transfer* 131(12): 121006-121012.

Fore, L. B., S. G. Beus and R. C. Bauer 2000. Interfacial friction in gas-liquid annular flow: analogies to full and transition roughness. *International Journal of Multiphase Flow* 26(11): 1755-1769.

Fu, B. R., M. S. Tsou and C. Pan 2012. Boiling heat transfer and critical heat flux of ethanol–water mixtures flowing through a diverging microchannel with artificial cavities. *International Journal of Heat and Mass Transfer* 55(5-6): 1807-1814.

Fuerstman, M. J., P. Garstecki and G. M. Whitesides 2007. Coding/decoding and reversibility of droplet trains in microfluidic networks. *Science* 315(5813): 828-832.

Geiger, G. E. 1964. *Sudden contraction losses in single and two-phase flow*. Ph. D., University of Pittsburgh.

Gunther, A. Y. and W. A. Shaw 1945. A General Correlation of Friction Factors for Various Types of Surfaces in Cross Flow. *Trans. ASME* 67: 643-660.

Guo, D., J. J. Wei and Y. H. Zhang 2011. Enhanced flow boiling heat transfer with jet impingement on micro-pin-finned surfaces. *Applied Thermal Engineering* 31(11–12): 2042-2051.

Guohua, L. and et al. 2009. Seed bubbles trigger boiling heat transfer in silicon microchannels. *Microfluidics and Nanofluidics*.

Guohua, L., X. Jinliang, Y. Yongping and Z. Wei 2010. Active control of flow and heat transfer in silicon microchannels. *Journal of Micromechanics and Microengineering* 20(4): 045006.

H. Kubo, H. T., and Hiroshi Honda 1999. Effects of size and number density of micro-reentrant cavities on boiling heat transfer from a silicon chip immersed in degassed and gas-dissolved FC-72. *Journal of Enhanced Heat Transfer* 6(2-4): 151-160.

Hailei, W. and R. B. Peterson 2010. Enhanced boiling heat transfer in parallel microchannels with diffusion brazed wire mesh. *Components and Packaging Technologies, IEEE Transactions on* 33(4): 784-793.

Harirchian, T. and S. V. Garimella 2011. Boiling heat transfer and flow regimes in microchannels---a comprehensive understanding. *Journal of Electronic Packaging* 133(1): 011001-011010.

Hartman, R. L. and K. F. Jensen 2009. Microchemical systems for continuous-flow synthesis. *Lab on a Chip* 9(17): 2495-2507.

Hernot, S. and A. L. Klibanov 2008. Microbubbles in ultrasound-triggered drug and gene delivery. *Advanced Drug Delivery Reviews* 60(10): 1153-1166.

Hetsroni, G., A. Mosyak, Z. Segal and E. Pogrebnyak 2003. Two-phase flow patterns in parallel micro-channels. *International Journal of Multiphase Flow* 29(3): 341-360.

Hitt, D. L., C. M. Zakrzwski and M. A. Thomas 2001. MEMS-based satellite micropropulsion via catalyzed hydrogen peroxide decomposition. *Smart Mater. Struct.* 10: 1163-1175.

Hsieh, S.-S. and C.-Y. Lin 2012. Correlation of critical heat flux and two-phase friction factor for subcooled convective boiling in structured surface microchannels. *International Journal of Heat and Mass Transfer* 55(1-3): 32-42.

Hsu, Y. Y. 1962. On the size range of active nucleation cavities on a heating surface. *Journal of Heat Transfer* 84: 207-216.

Jensen, K. F. 2001. Microreaction engineering - is small better? *Chemical Engineering Science* 56(2): 293-303.

Jiang, L. A., M. Wong and Y. Zohar 2001. Forced convection boiling in a microchannel heat sink. *Journal of Microelectromechanical Systems* 10(1): 80-87.

Jiang, Y. Y., H. Osada, M. Inagaki and N. Horinouchi 2013. Dynamic modeling on bubble growth, detachment and heat transfer for hybrid-scheme computations of nucleate boiling. *International Journal of Heat and Mass Transfer* 56(1–2): 640-652.

Jin, F., X. Gong, J. Ye and T. Ngai 2008. Direct measurement of the nanobubble-induced weak depletion attraction between a spherical particle and a flat surface in an aqueous solution. *Soft Matter* 4(5): 968-971.

Kabov, O. A., D. V. Zaitsev, V. V. Cheverda and A. Bar-Cohen 2011. Evaporation and flow dynamics of thin, shear-driven liquid films in microgap channels. *Experimental Thermal and Fluid Science* 35(5): 825-831.

Kandlikar, S. G. 2002. Fundamental issues related to flow boiling in minichannels and microchannels. *Experimental Thermal and Fluid Science* 26(2-4): 389-407.

Kandlikar, S. G. 2010. Scale effects on flow boiling heat transfer in microchannels: A fundamental perspective. *International Journal of Thermal Sciences* 49(7): 1073-1085.

Kandlikar, S. G. 2012. History, Advances, and Challenges in Liquid Flow and Flow Boiling Heat Transfer in Microchannels: A Critical Review. *Journal of Heat Transfer-Transactions of the Asme* 134(3).

Kandlikar, S. G. and A. V. Bapat 2007. Evaluation of jet impingement, spray and microchannel chip cooling options for high heat flux removal. *Heat Transfer Engineering* 28(11): 911-923.

Kandlikar, S. G., W. K. Kuan, D. A. Willistein and J. Borrelli 2006. Stabilization of flow boiling in microchannels using pressure drop elements and fabricated nucleation sites. *Journal of Heat Transfer-Transactions of the Asme* 128(4): 389-396.

Kandlikar, S. G., W. K. Kuan, D. A. Willistein and J. Borrelli 2006. Stabilization of flow boiling in microchannels using pressure drop elements and fabricated nucleation sites. *Journal of Heat Transfer* 128(4): 389-396.

Kashid, M. N., A. Renken and L. Kiwi-Minsker 2011. Gas-liquid and liquid-liquid mass transfer in microstructured reactors. *Chemical Engineering Science* 66(17): 3876-3897.

Kennedy, J. E., G. M. Roach, M. F. Dowling, S. I. Abdel-Khalik, S. M. Ghiaasiaan, S. M. Jeter and Z. H. Quershi 2000. The onset of flow instability in uniformly heated horizontal microchannels. *Journal of Heat Transfer-Transactions of the Asme* 122(1): 118-125.

Kenning, D. B. R., D. S. Wen, K. S. Das and S. K. Wilson 2006. Confined growth of a vapour bubble in a capillary tube at initially uniform superheat: Experiments and modelling. *International Journal of Heat and Mass Transfer* 49(23-24): 4653-4671.

Khanikar, V., I. Mudawar and T. Fisher 2009. Effects of carbon nanotube coating on flow boiling in a micro-channel. *International Journal of Heat and Mass Transfer* 52(15-16): 3805-3817.

Kim, J. H., K. N. Rainey, S. M. You and J. Y. Pak 2002. Mechanism of Nucleate Boiling Heat Transfer Enhancement From Microporous Surfaces in Saturated FC-72. *Journal of Heat Transfer* 124(3): 500-506.

Kline, S. J. and F. A. McClintock 1953. Describing uncertainties in single-sample experiments. *Mechanical Engineering* 75(1): 3- 8.

Kobayashi, J., Y. Mori, K. Okamoto, R. Akiyama, M. Ueno, T. Kitamori and S. Kobayashi 2004. A microfluidic device for conducting gas-liquid-solid hydrogenation reactions. *Science* 304(5675): 1305-1308.

Kosar, A., C. J. Kuo and Y. Peles 2005. Boiling heat transfer in rectangular microchannels with reentrant cavities. *International Journal of Heat and Mass Transfer* 48(23-24): 4867-4886.

Kosar, A., C. J. Kuo and Y. Peles 2006. Suppression of boiling flow oscillations in parallel microchannels by inlet restrictors. *Journal of Heat Transfer-Transactions of the Asme* 128(3): 251-260.

Kousalya, A. S., C. N. Hunter, S. A. Putnam, T. Miller and T. S. Fisher 2012. Photonically enhanced flow boiling in a channel coated with carbon nanotubes. *Applied Physics Letters* 100(7).

Krishnamurthy, S. and Y. Peles 2010. Flow boiling heat transfer on micro pin fins entrenched in a microchannel. *Journal of Heat Transfer* 132(4): 041007-041010.

Kuo-Shen, C., A. A. Ayon, Z. Xin and S. M. Spearing 2002. Effect of process parameters on the surface morphology and mechanical performance of silicon structures after deep reactive ion etching (DRIE). *Microelectromechanical Systems, Journal of* 11(3): 264-275.

Kuo-Shen, C., A. A. Ayon, X. Zhang and S. M. Spearing 2002. Effect of process parameters on the surface morphology and mechanical performance of silicon structures after deep reactive ion etching (DRIE). *Microelectromechanical Systems, Journal of* 11(3): 264-275.

Kuo, C. J., A. Kosar, Y. Peles, S. Virost, C. Mishra and M. K. Jensen 2006. Bubble dynamics during boiling in enhanced surface microchannels. *Journal of Microelectromechanical Systems* 15(6): 1514-1527.

Kuo, C. J. and Y. Peles 2008. Flow boiling instabilities in microchannels and means for mitigation by reentrant cavities. *Journal of Heat Transfer-Transactions of the Asme* 130(7).

Kuo, C. Y. and C. Gau 2010. Control of superhydrophilicity and superhydrophobicity of a superwetting silicon nanowire surface. *Journal of The Electrochemical Society* 157(9): K201-K205.

Lee, C. H., K. Jiang and G. J. Davies 2007. Sidewall roughness characterization and comparison between silicon and SU-8 microcomponents. *Materials Characterization* 58(7): 603-609.

Lee, H. J., D. Y. Liu and S.-c. Yao 2010. Flow instability of evaporative micro-channels. *International Journal of Heat and Mass Transfer* 53(9–10): 1740-1749.

Legendre, D., J. Boree and J. Magnaudet 1998. Thermal and dynamic evolution of a spherical bubble moving steadily in a superheated or subcooled liquid. *Physics of Fluids* 10(6): 1256-1272.

Li, C., Z. Wang, P.-I. Wang, Y. Peles, N. Koratkar and G. P. Peterson 2008. Nanostructured copper interfaces for enhanced boiling. *Small* 4(8): 1084-1088.

Li, C., Z. Wang, P. I. Wang, Y. Peles, N. Koratkar and G. P. Peterson 2008. Nanostructured copper interfaces for enhanced boiling. *Small* 4(8): 1084-1088.

Li, D., G. S. Wu, W. Wang, Y. D. Wang, D. Liu, D. C. Zhang, Y. F. Chen, G. P. Peterson and R. Yang 2012. Enhancing Flow Boiling Heat Transfer in Microchannels for Thermal Management with Monolithically-Integrated Silicon Nanowires. *Nano Letters*.

Li, H. Y., F. G. Tseng and C. Pan 2004. Bubble dynamics in microchannels. Part II: two parallel microchannels. *International Journal of Heat and Mass Transfer* 47(25): 5591-5601.

Li, J., G. P. Peterson and P. Cheng 2008. Dynamic characteristics of transient boiling on a square platinum microheater under millisecond pulsed heating. *International Journal of Heat and Mass Transfer* 51(1–2): 273-282.

Li, S., R. Furberg, M. S. Toprak, B. Palm and M. Muhammed 2008. Nature-Inspired Boiling Enhancement by Novel Nanostructured Macroporous Surfaces. *Advanced Functional Materials* 18(15): 2215-2220.

Lin, P. H., B. R. Fu and C. Pan 2011. Critical heat flux on flow boiling of methanol-water mixtures in a diverging microchannel with artificial cavities. *International Journal of Heat and Mass Transfer* 54(15-16): 3156-3166.

Liu, D., P. S. Lee and S. V. Garimella 2005. Prediction of the onset of nucleate boiling in microchannel flow. *International Journal of Heat and Mass Transfer* 48(25-26): 5134-5149.

Liu, G., J. Xu and Y. Yang 2010. Seed bubbles trigger boiling heat transfer in silicon microchannels. *Microfluidics and Nanofluidics* 8(3): 341-359.

Liu, G. H., J. L. Xu, Y. P. Yang and A. W. Zhang 2010. Active control of flow and heat transfer in silicon microchannels. *Journal of Micromechanics and Microengineering* 20(4).

Liu, T. Y., P. L. Li, C. W. Liu and C. Gau 2011. Boiling flow characteristics in microchannels with very hydrophobic surface to super-hydrophilic surface. *International Journal of Heat and Mass Transfer* 54(1-3): 126-134.

Liu, Z. H., T. F. Tong and Y. H. Qiu 2004. Critical heat flux of steady boiling for subcooled water jet impingement on the flat stagnation zone. *Journal of Heat Transfer-Transactions of the Asme* 126(2): 179-183.

Losey, M. W., R. J. Jackman, S. L. Firebaugh, M. A. Schmidt and K. F. Jensen 2002. Design and fabrication of microfluidic devices for multiphase mixing and reaction. *Journal of Microelectromechanical Systems* 11(6): 709-717.

Lugli, F. and F. Zerbetto 2007. An introduction to bubble dynamics. *Physical Chemistry Chemical Physics* 9(20): 2447-2456.

Lukianova-Hleb, E., Y. Hu, L. Latterini, L. Tarpani, S. Lee, R. A. Drezek, J. H. Hafner and D. O. Lapotko 2010. Plasmonic nanobubbles as transient vapor nanobubbles generated around plasmonic nanoparticles. *Acs Nano* 4(4): 2109-2123.

Luo, X. B. and S. Liu 2007. A microjet array cooling system for thermal management of high-brightness LEDs. *Ieee Transactions on Advanced Packaging* 30(3): 475-484.

Marmottant, P. and J.-P. Raven 2009. Microfluidics with foams. *Soft Matter* 5(18): 3385-3388.

Mikic, B. B., W. M. Rohsenow and P. Griffith 1970. On bubble growth rates. *International Journal of Heat and Mass Transfer* 13(4): 657-666.

Morshed, A. K. M. M., F. Yang, M. Yakut Ali, J. A. Khan and C. Li 2012. Enhanced flow boiling in a microchannel with integration of nanowires. *Applied Thermal Engineering* 32(0): 68-75.

Mudawar, I. 2001. Assessment of high-heat-flux thermal management schemes. *Ieee Transactions on Components and Packaging Technologies* 24(2): 122-141.

Mukherjee, A. and S. G. Kandlikar 2006. Numerical study of an evaporating meniscus on a moving heated surface. *Journal of Heat Transfer-Transactions of the Asme* 128(12): 1285-1292.

Mukherjee, A. and S. G. Kandlikar 2009. The effect of inlet constriction on bubble growth during flow boiling in microchannels. *International Journal of Heat and Mass Transfer* 52(21–22): 5204-5212.

Nukiyama, S. 1966. The maximum and minimum values of the heat Q transmitted from metal to boiling water under atmospheric pressure. *International Journal of Heat and Mass Transfer* 9(12): 1419-1433.

Ory, E., H. Yuan, A. Prosperetti, S. Popinet and S. Zaleski 2000. Growth and collapse of a vapor bubble in a narrow tube. *Physics of Fluids* 12(6): 1268-1277.

Peles, Y. 2012. *Contemporary Perspectives on Flow Instabilities in Microchannels*, Begell House Inc.

Peng, K. Q., Y. J. Yan, S. P. Gao and J. Zhu 2002. Synthesis of Large-Area Silicon Nanowire Arrays via Self-Assembling Nanoelectrochemistry. *Advanced Materials* 14(16): 1164-1167.

Pike, W. T., W. J. Karl, S. Kumar, S. Vijendran and T. Semple 2004. Analysis of sidewall quality in through-wafer deep reactive-ion etching. *Microelectronic Engineering* 73–74(0): 340-345.

Po Chang, L. and P. Chin 2008. Boiling heat transfer and two-phase flow of water in a single shallow microchannel with a uniform or diverging cross section. *Journal of Micromechanics and Microengineering* 18(2): 025005.

Prakash, M. and N. Gershenfeld 2007. Microfluidic bubble logic. *Science* 315(5813): 832-835.

Qu, W. L. and I. Mudawar 2003. Measurement and prediction of pressure drop in two-phase micro-channel heat sinks. *International Journal of Heat and Mass Transfer* 46(15): 2737-2753.

Qu, W. L. and I. Mudawar 2004. Measurement and correlation of critical heat flux in two-phase micro-channel heat sinks. *International Journal of Heat and Mass Transfer* 47(10-11): 2045-2059.

R. B. Maxwell, A. L. G., M. Toner, M. L. Gray, and M. A. 2003. A microbubble-powered bioparticle actuator. *J. Microelectromech.Syst.* 12(5): 630-640.

Rabaud, D. 2011. Manipulation of confined bubbles in a thin microchannel: Drag and acoustic Bjerknes forces. *Phys. Fluids* 23(4): 042003.

Rahim, E., R. Revellin, J. Thome and A. Bar-Cohen 2011. Characterization and prediction of two-phase flow regimes in miniature tubes. *International Journal of Multiphase Flow* 37(1): 12-23.

Rapolu, P. and S. Son 2011. Characterization of wettability effects on pressure drop of two-phase flow in microchannel. *Experiments in Fluids* 51(4): 1101-1108.

Rashid, A., P. Bjorn, M. C. Claudi and H. M. Mohammad 2010. *Flow patterns and flow pattern maps for microchannels*. Thermal Issues in Emerging Technologies Theory and Applications (ThETA), 2010 3rd International Conference on.

Raven, J.-P. and P. Marmottant 2006. Periodic Microfluidic Bubbling Oscillator: Insight into the Stability of Two-Phase Microflows. *Physical Review Letters* 97(15): 154501.

Robin H. Liu, J. Y., Maciej Z. Pindera, Mahesh Athavale and Piotr Grodzinski 2002. Bubble-induced acoustic micromixing. *Lab on a Chip* 2: 151-157.

Rovinsky, J., N. Brauner and D. Moalem Maron 1997. Analytical solution for laminar two-phase flow in a fully eccentric core-annular configuration. *International Journal of Multiphase Flow* 23(3): 523-543.

Royne, A., C. J. Dey and D. R. Mills 2005. Cooling of photovoltaic cells under concentrated illumination: a critical review. *Solar Energy Materials and Solar Cells* 86(4): 451-483.

Sbragaglia, M., R. Benzi, L. Biferale, S. Succi and F. Toschi 2006. Surface roughness-hydrophobicity coupling in microchannel and nanochannel flows. *Physical Review Letters* 97(20).

Schasfoort, R. B. M., S. Schlautmann, L. Hendrikse and A. van den Berg 1999. Field-effect flow control for microfabricated fluidic networks. *Science* 286(5441): 942-945.

Schneider, B., A. Kosar, C. J. Kuo, C. Mishra, G. S. Cole, R. P. Scaringe and Y. Peles 2006. Cavitation enhanced heat transfer in microchannels. *Journal of Heat Transfer-Transactions of the Asme* 128(12): 1293-1301.

Serizawa, A., Z. Feng and Z. Kawara 2002. Two-phase flow in microchannels. *Experimental Thermal and Fluid Science* 26(6-7): 703-714.

Serizawa, A., Z. P. Feng and Z. Kawara 2002. Two-phase flow in microchannels. *Experimental Thermal and Fluid Science* 26(6-7): 703-714.

Shah, R. K. and A. L. London 1978. *Laminar Flow Forced Convection in Ducts*. New York, Academic Press.

Shui, L., S. Pennathur, J. C. T. Eijkel and A. van den Berg 2008. Multiphase flow in lab on chip devices: A real tool for the future. *Lab on a Chip* 8(7): 1010-1014.

Singh, N., V. Sathyamurthy, W. Peterson, J. Arendt and D. Banerjee 2010. Flow boiling enhancement on a horizontal heater using carbon nanotube coatings. *International Journal of Heat and Fluid Flow* 31(2): 201-207.

Tadashi Okamoto, T. S., and Nobuko Yamamoto 2000. Microarray fabrication with covalent attachment of DNA using Bubble Jet technology. *Nature Biotechnology* 18: 438-441.

Thome, J. R. 2004. Boiling in microchannels: a review of experiment and theory. *International Journal of Heat and Fluid Flow* 25(2): 128-139.

Thome, J. R. 2006. State-of-the-art overview of boiling and two-phase flows in microchannels. *Heat Transfer Engineering* 27(9): 4-19.

Thorncroft, G. E. and J. F. Klausner 2001. BUBBLE FORCES AND DETACHMENT MODELS. *Multiphase Science and Technology* 13(3&4): 42.

Trieu Phan, H., N. Caney, P. Marty, S. Colasson and J. Gavillet 2011. Flow boiling of water in a minichannel: The effects of surface wettability on two-phase pressure drop. *Applied Thermal Engineering* 31(11–12): 1894-1905.

Tsai, J. and J. Lin 2002. Active microfluidic mixer and gas bubble filter driven by thermal bubble micropump. *Sens. Actuators A, Phys* 97-98: 665-671.

Tsai, J. and L. Lin 2002. A thermal-bubble-actuated micronozzle-diffuser pump. *Journal of Microelectromechanical Systems* 11: 665-671.

Tsiglifis, K. and N. A. Pelekasis 2007. Nonlinear oscillations and collapse of elongated bubbles subject to weak viscous effects: Effect of internal overpressure. *Physics of Fluids* 19(7): 072106.

Ujereh, S., T. Fisher and I. Mudawar 2007. Effects of carbon nanotube arrays on nucleate pool boiling. *International Journal of Heat and Mass Transfer* 50(19-20): 4023-4038.

Vafaei, S. and D. Wen 2010. Critical heat flux (CHF) of subcooled flow boiling of alumina nanofluids in a horizontal microchannel. *Journal of Heat Transfer* 132(10): 102404-102407.

Van Helden, W. G. J., C. W. M. Van Der Geld and P. G. M. Boot 1995. Forces on bubbles growing and detaching in flow along a vertical wall. *International Journal of Heat and Mass Transfer* 38(11): 2075-2088.

Vassallo, P. F. and R. Kumar 1999. Liquid and gas velocity measurements using LDV in air-water duct flow. *Experimental Thermal and Fluid Science* 19(2): 85-92.

Vengallatore, S., Y. Peles, L. R. Arana and S. M. Spearing 2004. Self-assembly of micro- and nanoparticles on internal micromachined silicon surfaces. *Sensors and Actuators A: Physical* 113(1): 124-131.

Wang, G. and P. Cheng 2009. Subcooled flow boiling and microbubble emission boiling phenomena in a partially heated microchannel. *International Journal of Heat and Mass Transfer* 52(1-2): 79-91.

Wang, G., P. Cheng and A. E. Bergles 2008. Effects of inlet/outlet configurations on flow boiling instability in parallel microchannels. *International Journal of Heat and Mass Transfer* 51(9-10): 2267-2281.

Wang, G., P. Cheng and H. Wu 2007. Unstable and stable flow boiling in parallel microchannels and in a single microchannel. *International Journal of Heat and Mass Transfer* 50(21–22): 4297-4310.

Wang, H., S. V. Garimella and J. Y. Murthy 2007. Characteristics of an evaporating thin film in a microchannel. *International Journal of Heat and Mass Transfer* 50(19–20): 3933-3942.

Wojtan, L., R. Revellin and J. R. Thome 2006. Investigation of saturated critical heat flux in a single, uniformly heated microchannel. *Experimental Thermal and Fluid Science* 30(8): 765-774.

Wu, H. Y. and P. Cheng 2003. Visualization and measurements of periodic boiling in silicon microchannels. *International Journal of Heat and Mass Transfer* 46(14): 2603-2614.

Wu, H. Y. and P. Cheng 2004. Boiling instability in parallel silicon microchannels at different heat flux. *International Journal of Heat and Mass Transfer* 47(17-18): 3631-3641.

Wu, H. Y., P. Cheng and H. Wang 2006. Pressure drop and flow boiling instabilities in silicon microchannel heat sinks. *Journal of Micromechanics and Microengineering* 16(10): 2138-2146.

Wu, Z. H., H. B. Chen, Y. M. Dong, H. L. Mao, J. L. Sun, S. F. Chen, V. S. J. Craig and J. Hu 2008. Cleaning using nanobubbles: Defouling by electrochemical generation of bubbles. *Journal of Colloid and Interface Science* 328(1): 10-14.

Xu, J., G. Liu, W. Zhang, Q. Li and B. Wang 2009. Seed bubbles stabilize flow and heat transfer in parallel microchannels. *International Journal of Multiphase Flow* 35(8): 773-790.

Xu, J., J. Zhou and Y. Gan 2005. Static and dynamic flow instability of a parallel microchannel heat sink at high heat fluxes. *Energy Conversion and Management* 46(2): 313-334.

Yang, F., X. Dai, C.-J. Kuo, Y. Peles, J. Khan and C. Li 2013. Enhanced flow boiling in microchannels by self-sustained high frequency two-phase oscillations. *International Journal of Heat and Mass Transfer* 58(1–2): 402-412.

Yang, F., X. Dai and C. Li 2012. High Frequency Microbubble-switched Oscillations Modulated by Microfluidic Transistors. *Applied Physics Letters* Submission.

Yang, F., X. Dai, Y. Peles, P. Cheng and C. Li 2013. Can Transitional Flow Boiling Regimes Be Reduced into a Single and Periodic Annular Flow in Microchannels? *Applied Physics Letters*.

Zhang, M.-L., K.-Q. Peng, X. Fan, J.-S. Jie, R.-Q. Zhang, S.-T. Lee and N.-B. Wong 2008. Preparation of Large-Area Uniform Silicon Nanowires Arrays through Metal-Assisted Chemical Etching. *The Journal of Physical Chemistry C* 112(12): 4444-4450.

Zhang, T., T. Tong, J.-Y. Chang, Y. Peles, R. Prasher, M. K. Jensen, J. T. Wen and P. Phelan 2009. Ledinegg instability in microchannels. *International Journal of Heat and Mass Transfer* 52(25-26): 5661-5674.

Zimmerman, W. B., V. Tesař and H. C. H. Bandulasena 2011. Towards energy efficient nanobubble generation with fluidic oscillation. *Current Opinion in Colloid & Interface Science* 16(4): 350-356.